BILINGUAL PUBLISHING GROUP

Non-Metallic Material Science

Volume 5 • Issue 1 • April 2023 ISSN 2661-3301(Online)

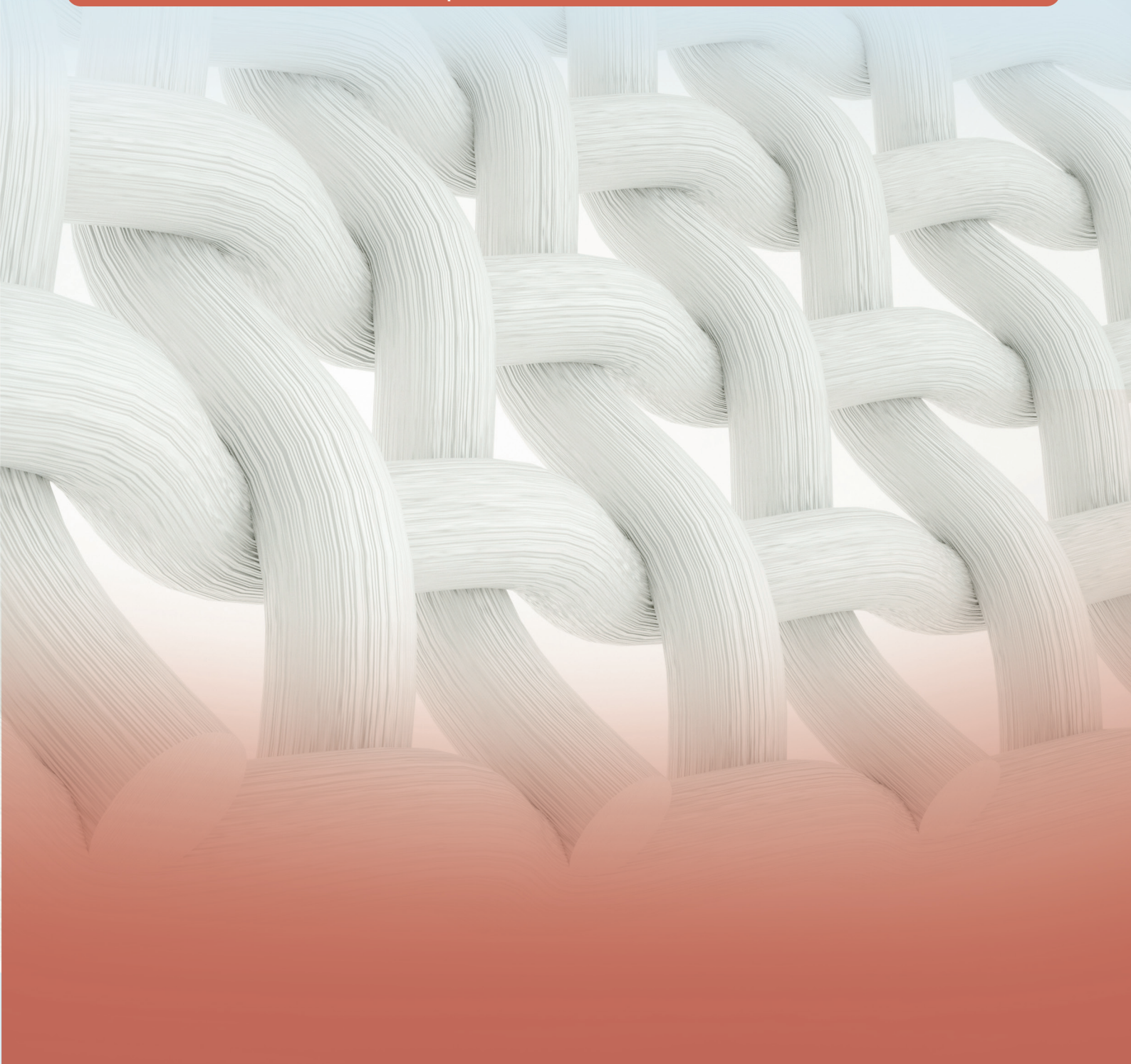

Volume 5 Issue 1 · April 2023 · ISSN 2661-3301 (Online)

Non-Metallic Material Science

Editor-in-Chief

Professor Sabu Thomas

BILINGUAL PUBLISHING GROUP

BILINGUAL PUBLISHING GROUP

Volume 5 | Issue 1 | April 2023 | Page1-63

Non-Metallic Material Science

Contents

Editorial

Articles

Review

BILINGUAL PUBLISHING GROUP

Non-Metallic Material Science

https://journals.bilpubgroup.com/index.php/nmms

EDITORIAL

Editorial on Emerging Trends in Polymeric Materials Research and Applications

Muhammad Imran Rashid

Chemical, Polymer and Composite Materials Engineering Department, University of Engineering and Technology, Lahore (New Campus), 39021, Pakistan

Polymeric materials especially nanocomposites (Graphene, MXene based) are widely used in food, electronics, biomedical, batteries, energy storage, fuel cells, wastewater treatment, and automotive [1]. Nanocomposites are stronger, lighter, and stiffer and can improve properties such as mechanical strength, electrical conductivity, thermal stability, flame retardancy, surface appearance, optical clarity and chemical resistance. Current research is focusing on nanocomposites applications [1-3], CO_2 capturing polymers [4], making polymers degradable [5-7] especially developing bio-composites [8] and green composites [9,10] which are degradable, use of deep eutectic solvents for biomass pretreatment to manufacture bio-composites or green composites and polymeric composites as drilling fluids [11] and their use in developing ceramics and to construct sequence-controlled and complex topological structures through control of polymerization methodologies.

Current research is progressing towards tailoring the properties of nanocomposites thus enabling their use for multiple applications. Entropic effects interplay with interparticle interactions can yield effective tailoring of nanocomposites [12]. The relation between thermodynamic interactions and macroscale morphologies is important. Schiff base with nitro groups [13], dibutyltin (IV) complex, telmisartan organotin (IV) [14] and polyphosphates [15] are currently employed for carbon dioxide storage. Rice husk treated with choline chloride and aqueous glycerol was incorporated into LDPE to develop bio composites with high hardness and elastic modulus and lower creep rate [16,17]. Deep eutectic solvents result

*CORRESPONDING AUTHOR:
Muhammad Imran Rashid, Chemical, Polymer and Composite Materials Engineering Department, University of Engineering and Technology, Lahore (New Campus), 39021, Pakistan; Email: muhammadimran_rashid@yahoo.com

ARTICLE INFO
Received: 28 December 2022 | Revised: 29 December 2022 | Accepted: 30 December 2022 | Published Online: 11 January 2023
DOI: https://doi.org/10.30564/nmms.v5i1.5328

CITATION
Rashid, M.I., 2023. Editorial on Emerging Trends in Polymeric Materials Research and Applications. Non-Metallic Material Science. 5(1): 1-3. DOI: https://doi.org/10.30564/nmms.v5i1.5328

in polymer bio-composites with enhanced mechanical and fire safety characteristics [18] and their use is increasing in developing carbon composites [19], silica composites [20] and valorization of lignocellulosic biomass [21].

Polymer composites have many applications in the oil and gas sector where it is used as an additive in the preparation of smart fluids. The smart fluids in the oil and gas sector are used as drilling aids in the drilling process of wellbore and enhanced oil recovery process. Polymer composites prepared by a combination of water-soluble polymer and carbon nanotubes will improve the rheology, filtration, and shale inhibition properties of drilling fluids. Polymer nanocomposite synthesized by solution polymerization technique in which functionalize carbon nanotubes were dispersed in the solution and three different monomers (2-Acrylamido-2-methylpropane sulfonic acid, acrylamide, and maleic acid) reacted with each other to produce polymer nanocomposite is utilized as an additive for drilling fluid formulation. The synthesized polymer nanocomposite improved the thermal stability, rheological properties, filtration properties, and shale inhibition properties [11,22].

Conflict of Interest

There is no conflict of interest.

References

[1] Ates, B., Koytepe, S., Ulu, A., et al., 2020. Chemistry, structures, and advanced applications of nanocomposites from biorenewable resources. Chemical Reviews. 120(17), 9304-9362. doi: 10.1021/acs.chemrev.9b00553.

[2] Hassan, T., Salam, A., Khan, A., et al., 2021. Functional nanocomposites and their potential applications: A review. Journal of Polymer Research. 28(2), 36. doi: 10.1007/s10965-021-02408-1.

[3] Muhammed S.M., Sasikanth, S.M., Annamalai, R., et al., 2021. A brief review on polymer nanocomposites and its applications. Materials Today: Proceedings. 45, 2536-2539. doi: https://doi.org/10.1016/j.matpr.2020.11.254.

[4] Rashid, M.I., 2022. GHG emissions and role of polymeric materials in mitigation. Non-Metallic Material Science. 4(1), 1-2.

[5] Luckachan, G.E., Pillai, C.K.S., 2011. Biodegradable Polymers—A review on recent trends and emerging perspectives. Journal of Polymers and the Environment. 19(3), 637-676. doi: 10.1007/s10924-011-0317-1.

[6] Shah, T.V., Vasava, D.V., 2019. A glimpse of biodegradable polymers and their biomedical applications. e-Polymers. 19(1), 385-410. doi: 10.1515/epoly-2019-0041.

[7] Leo, C.M., Kennemur, J.G., 2022. A new CAM-MP-ing ground for polymers. Nature Synthesis. 1(12), 917-918. doi: 10.1038/s44160-022-00198-y.

[8] Gao, C., Yao, M., Li, S., et al., 2019. Highly biodegradable and bioactive Fe-Pd-bredigite biocomposites prepared by selective laser melting. Journal of Advanced Research. 20, 91-104. doi: 10.1016/j.jare.2019.06.001.

[9] Kuram, E., 2022. Advances in development of green composites based on natural fibers: A review. Emergent Materials. 5(3), 811-831. doi: 10.1007/s42247-021-00279-2.

[10] Das, R., Bhattacharjee, C., 2022. Chapter 4—Green composites, the next-generation sustainable composite materials: Specific features and applications. Altalhi T, Inamuddin, (editors). Green Sustainable Process for Chemical and Environmental Engineering and Science. Elsevier: Amsterdam. pp. 55-70.

[11] Ahmad, H.M., Kamal, M.S., Al-Harthi, M.A., 2018. High molecular weight copolymers as rheology modifier and fluid loss additive for water-based drilling fluids. Journal of Molecular Liquids. 252, 133-143. doi: 10.1016/j.molliq.2017.12.135.

[12] Dai, X., Hou, C., Xu, Z., et al., 2019. Entropic effects in polymer nanocomposites. Entropy (Basel, Switzerland). 21(2). doi: 10.3390/e21020186.

[13] Omer, R.M., Al-Tikrity, E.T.B., El-Hiti, G.A.,

et al., 2020. Porous aromatic melamine schiff bases as highly efficient media for carbon dioxide storage. Processes. 8(1), 17. Available from: https://www.mdpi.com/2227-9717/8/1/17.

[14] Hadi, A.G., Jawad, K., Yousif, E., et al., 2019. Synthesis of telmisartan organotin(IV) complexes and their use as carbon dioxide capture media. Molecules. 24(8), 1631. Available from: https://www.mdpi.com/1420-3049/24/8/1631.

[15] Satar, H.A., Ahmed, A.A., Yousif, E., et al., 2019. Synthesis of novel Heteroatom-Doped Porous-Organic polymers as environmentally efficient media for carbon dioxide storage. Applied Sciences. 9(20), 4314. Available from: https://www.mdpi.com/2076-3417/9/20/4314.

[16] Sulaiman, M., Iqbal, T., Yasin, S., et al., 2020. Study of nano-mechanical performance of pretreated natural fiber in ldpe composite for packaging applications. Materials (Basel, Switzerland). 13(21). doi: 10.3390/ma13214977.

[17] Sulaiman, M., Iqbal, T., Yasin, S., et al., 2021. Fabrication and nanomechanical characterization of thermoplastic biocomposites based on chemically treated lignocellulosic biomass for surface engineering applications. Frontiers in Materials. 8. doi: 10.3389/fmats.2021.733109.

[18] Zabihi, O., Ahmadi, M., Yadav, R., et al., 2021. Novel phosphorous-based deep eutectic solvents for the production of recyclable macadamia nutshell–polymer biocomposites with improved mechanical and fire safety performances. ACS Sustainable Chemistry & Engineering. 9(12), 4463-4476. doi: 10.1021/acssuschemeng.0c08447.

[19] Carrasco-Huertas, G., Jiménez-Riobóo, R.J., Gutiérrez, M.C., et al., 2020. Carbon and carbon composites obtained using deep eutectic solvents and aqueous dilutions thereof. Chemical Communications. 56(25), 3592-3604. doi: 10.1039/D0CC00681E.

[20] Yang, H., Yang, L., Guo, H., et al., 2021. The effect of silica modified by deep eutectic solvents on the properties of nature rubber/silica composites. Journal of Elastomers & Plastics. 54(1), 111-122. doi: 10.1177/00952443211020051.

[21] Scelsi, E., Angelini, A., Pastore, C., 2021. Deep eutectic solvents for the valorisation of lignocellulosic biomasses towards fine chemicals. Biomass. 1(1), 29-59. https://www.mdpi.com/2673-8783/1/1/3.

[22] Ahmad, H.M., Iqbal, T., Kamal, M.S., et al., 2020. Influence of hydrophobically modified polymer and titania nanoparticles on shale hydration and swelling properties. Energy & Fuels. 34(12), 16456-16468. doi: 10.1021/acs.energyfuels.0c02445.

BILINGUAL PUBLISHING GROUP

Non-Metallic Material Science

https://journals.bilpubgroup.com/index.php/nmms

ARTICLE

High Energy X-Ray Dosimetry Using $(ZnO)_{0.2}(TeO_2)_{0.8}$ Thin Film-based Real-time X-Ray Sensor

M.M. Idris[1,2,3*], I.O. Olarinoye[1], M.T. Kolo[1], S.O. Ibrahim[1], and J.K. Audu[4]

[1] *Department of Physics, Federal University of Technology, P.M.B 65, Minna, Nigeria*

[2] *Department of Physics, Nasarawa State University, P.M.B 1022, Keffi, Nigeria*

[3] *Department of Physics, University Putra, 43400, Malaysia*

[4] *Department of Medical Physics and Radiotherapy, National Hospital, P.M.B 425, Abuja, Nigeria*

ABSTRACT

This study reports the dosimetric response of a $(ZnO)_{0.2}(TeO_2)_{0.8}$ thin film sensor irradiated with high-energy X-ray radiation at various doses. The spray pyrolysis method was used for the film deposition on soda-lime glass substrate using zinc acetate dehydrate and tellurium dioxide powder as the starting precursors. The structural and morphological properties of the film were determined. The I-V characteristics measurements were performed during irradiation with a 6 MV X-ray beam from a Linac. The results revealed that the XRD pattern of the AS-deposited thin film is non-crystalline (amorphous) in nature. The FESEM image shows the non-uniform shape of nanoparticles agglomerated separately, and the EDX spectrum shows the presence of Te, Zn, and O in the film. The I-V characteristics measurements indicate that the current density increases linearly with X-ray doses (0-250 cGy) for all applied voltages (1-6 V). The sensitivity of the thin film sensor has been found to be in the range of 0.37-0.94 $mA/cm^2/Gy$. The current-voltage measurement test for fading normalised in percentage to day 0 was found in the order of day 0 > day 15 > day 30 > day 1 > day 2. These results are expected to be beneficial for fabricating cheap and practical X-ray sensors.

Keywords: Thin film; X- ray radiation; I-V characteristics; Dosimetry

*CORRESPONDING AUTHOR:

M.M. Idris, Department of Physics, Federal University of Technology, P.M.B 65, Minna, Nigeria; Department of Physics, Nasarawa State University, P.M.B 1022, Keffi, Nigeria; Department of Physics, University Putra, 43400, Malaysia; Email: idrismustapham@nsuk.edu.ng

ARTICLE INFO

Received: 27 December 2022 | Revised : 30 December 2022 | Accepted: 2 February 2023 | Published Online: 16 February 2023

DOI: https://doi.org/10.30564/nmms.v5i1.5369

CITATION

Idris, M.M., Olarinoye, I.O., Kolo, M.T., et al., 2023. High Energy X-Ray Dosimetry Using $(ZnO)_{0.2}(TeO_2)_{0.8}$ Thin Film-based Real-time X-Ray Sensor. Non-Metallic Material Science. 5(1): 4-13. DOI: https://doi.org/10.30564/nmms.v5i1.5369

1. Introduction

The continuous expansion of ionising radiation applications in many areas has necessitated the use of dosimeters with special physical features, such as small size [1]. The quest to design miniaturised dosimeters with small active volumes has consequently led to increasing research into materials in thin film form for their dosimetric properties [2-4]. Numerous techniques of deposition, both physical and chemical, have been adopted for transparent conducting oxide thin film preparation. The desired properties of the prepared film are predetermined by the deposition technique used. These can greatly affect the functionality of the film device [5].

The widespread usage of transparent conducting oxide (TCO) thin films in optoelectronic devices such as touch screens, liquid crystal displays, solar cells, and light-emitting diodes in recent years has drawn substantial scientific interest [6,7]. Owing to its strong electrical conductivity and excellent transparency to visible light, indium tin oxide (ITO) is the most widely used TCO [8]. The high price, limited supply, and toxicity of indium, the main component of ITO, have raised significant concerns about finding viable substitutes [9]. In addition, ITO loses some of its electrical and optical qualities when exposed to a hydrogen plasma environment [10].

Due to its excellent optical and electrical characteristics as well as the low cost, non-toxicity, and abundance of Zn, ZnO is a particularly alluring material in this respect and a great substitute material for ITO [11]. At ambient temperature, ZnO is an n-type semiconductor material with a relatively broad band gap energy of 3.37 eV and a significant exciton-binding energy (60 meV) [12]. High thermal stability, strong stability in hydrogen plasma, and high electrochemical stability are some of its additional advantageous characteristics when compared to ITO [11,13].

Tellurium oxide is a p-type semiconductor material with a band gap of about 2.88 eV and interesting non-linear optical properties [14]. It is characterised by a high dielectric constant in both crystal and film making it a potential candidate for future use in ultra-high integrated electronic devices [15]. TeO_2 based materials have attracted considerable research interest in recent years due to their high refractive index, good non-linear optical properties and electrical semi-conductivity appealing for various applications [16].

Transparent conducting oxide has been reported to be deposited on substrates using a variety of deposition techniques, including pulse laser deposition (PLD) [17], chemical vapour deposition (CVD) [18], radio frequency (RF) sputtering [19], and the sol-gel method [20]. RF sputtering method and convoluted deposition techniques, like MBE, showed good thin film defect density, crystal structure consistency, and high deposition speeds with little defect concentration [19]. The deposition technique, however, costs more than conventional deposition techniques while producing high deposition rates. The spray pyrolysis method can produce high-quality thin films on substrates at moderate temperatures with a low cost of operation [21-31].

With regard to the lattice characteristics and thermal mismatching between the substrate and the film owing to the development of stress in the deposited films, the choice of substrate material is crucial for the formation of ZnO doped TeO_2 thin films [24]. Aside from that, the type of substrate can also affect how ZnO film nucleates and grows. Soda-lime glass [25], sapphire (Al_2O_3) [26], Si (1 0 0) [9], and GaAs [27] are examples of substrates often employed for the deposition of a most metal oxide including ZnO and TeO_2 thin films. Among the substrate materials, soda-lime glass substrate has been proven suitable [29-36]. In this study, we prepared a $(ZnO)_{0.2}(TeO_2)_{0.8}$ thin film sensor by spray pyrolysis with the aim of testing the dosimetric response during irradiation with high-energy x-rays.

Thin film sensor undergoes structural changes when exposed to ionising radiation such as optical, structural and electrical properties [29]. Ionizing radiation can cause changes in the properties of the thin film which depend on the radiation dose, parameters associated with the films, and the radiation type [7,30-32]. Previous studies have investigated materials in thin film form as radiation sensors for conceivable dosimeter designs [29-37]. For gamma sens-

ing and dosimetry application, In_2O_3 thin film was recently deposited using the spray pyrolysis method and optimised [33]. It was discovered that the deposition conditions affected the film's gamma-ray sensitivity. The investigation came to the conclusion that the thin films are suitable for use as photon dosimeters. However, the toxic nature of indium oxide [34] could prevent the widespread manufacture of dosimeters based on the substance. Another study [35] discovered that polymer-encased CS_4PbI_6 thin films were extremely sensitive to X-rays, reaching 256.20 cu cm^{-2} for 30 keV X-rays at a bias voltage of 10 V. The materials were determined to be reliable, strong, and reusable for radiation measurement. The effects of gamma photon irradiation on the crystallinity, microstructure, optical transmission, and photoluminescence characteristics of PbIn thin films deposited by the spin coating process were also reported by Aldawood et al. [35]. The examined film's characteristics were discovered to change with photon exposure and may be calibrated for radiation monitoring and detection. Other thin film materials, including ZTO [37], ZrO_2 [36], MoO_3 [38], ZnO [39], ITO [40], TeO_2 [41], and others, have shown properties that make them highly sensitive to radiation and, as a result, appropriate for the fabrication of real-time dosimeters.

When subjected to photons, ZnO and TeO_2 have each individually demonstrated changes in their optical, structural, and electrical characteristics [16,39,41]. These findings show that both materials are highly photon sensitive due to their electrical and optical characteristics. However, it could be possible to maximise radiation sensitivity by combining both materials in thin film form. As a result, for the first time, this study will look at how the electrical characteristics of $(ZnO)_{0.2}(TeO_2)_{0.8}$ composite thin films are altered for X-ray photon detection and dosimetry. The fabrication of thin-film-based miniaturized dosimeters that is extremely sensitive, stable, repeatable, reusable, and capable of real-time readout in radiation-related applications such as medicine was the motivating factor behind this study. This study aims to investigate and evaluate the effects of various X-ray doses on the current-voltage (I-V) properties of the $(ZnO)_{0.2}(TeO_2)_{0.8}$ thin film sensor, as well as the sensitivity and lowest detectable dosage at various bias voltages.

2. Experimental procedure

2.1 Chemical synthesis

The zinc acetate dehydrate was slowly added (drop-wise) into a beaker placed on an analytical balance until 0.863 g was measured, then 2.0 mL of acetyl acetone and 58.0 mL of methanol were added, respectively. The mixture was stirred vigorously using a magnetic stirrer for about 15 minutes at room temperature until the solute completely dissolved. Also, 0.638 g of tellurium dioxide solute with a molecular weight of 159.6 g/mol was measured and then dissolved in 40 mL of HCl (43 mol% concentration) and 20 mL of methanol, respectively. The solution was vigorously mixed while being heated at 60 °C for about 15 minutes using a magnetic stirrer hotplate, until the solute dissolved completely. The addition of methanol to the tellurium dioxide solution was to prevent precipitation.

2.2 Thin film deposition

Spray pyrolysis was used to create the $(ZnO)_{0.2}(TeO_2)_{0.8}$ thin film sensors. Compressed air was employed as a carrier gas to spray the atomized precursor solution of ZnO-doped TeO_2 onto a heated soda-lime glass substrate using a desktop-style automated ultrasonic spray pyrolysis coating apparatus (U-spray USP 1500). 10 mL of the precursor solution was placed in the dispensing tank of the depositor, and the substrate temperature was maintained at 300 °C throughout the deposition procedure. The flow rates of the solution, air, and the distance from the nozzle to the substrate are 0.15 $mL \cdot min^{-1}$, 0.2 $kg \cdot cm^{-2}$, and 3.0 cm, respectively. An innate solution tube and a glass tube, through which carrier gases travel, make up the spray nozzle. The solution is automatically sucked in and then sprayed when pressure is applied to the carrier gas, which creates a vacuum at the nozzle's tip. A thin film of thickness 375 nm was created

using 1.2 mL of the synthesised $(ZnO)_{0.2}$ $(TeO_2)_{0.8}$ solution that had been atomized. On the thin film that had been created, a thick film of interdigitated graphite electrodes with an equal inter-electrode spacing of 0.3 mm was printed, together with two copper foils positioned at the margins of the graphite electrodes 10 mm apart from one another. **Figure 1** depicts the schematics diagram of the $(ZnO)_{0.2}(TeO_2)_{0.8}$ thin film sensor that has been constructed.

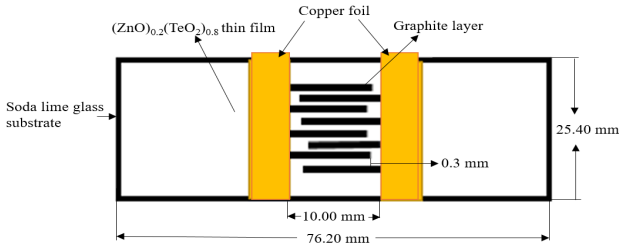

Figure 1. Schematic diagram of the prepared $(ZnO)_{0.2}(TeO_2)_{0.8}$ thin film sensor.

2.3 Characterisation

The film crystallinity and crystalline phase of $(ZnO)_{0.2}(TeO_2)_{0.8}$ thin film was analyzed by X-ray diffraction measurement which was carried out at room temperature by using PHILIPS (PW 3040/60 MPD X'PERT HIGH PRO PANALYTICAL) diffractometer system (scan step of 0.05° (2θ), counting time of 10.16 s per data point) operated at 40 kV and 30 mA. It is equipped with a Cu tube for generating Cu-Kα radiation (k = 1.5406 Å); as an incident beam in the 2-theta mode over the range of 10°-80°. The morphological analysis was performed by FEI (Nova Nanosem 230) field emission scanning electron microscope (FESEM). Energy-dispersive spectrum (EDX) analysis of the film was performed during FESEM measurements.

2.4 Irradiation and I-V characteristic determination

The $(ZnO)_{0.2}(TeO_2)_{0.8}$ thin film sensor was exposed to various doses (dose rate) of 50 cGy (200 cGy), 100 cGy (250 cGy/min), 150 cGy (300 cGy/min), 200 cGy (350 cGy/min), and 250 cGy (400 cGy) X-ray at an exposure time of 0.25, 0.4, 0.5, 0.57, 0.63 min, respectively, using a 6 MV photon beam linear accelerator (Elekta Synergy Platform). The thin film was positioned such that it was parallel to the X-ray beam. Secondary charged particle equilibrium was implemented using an additional PMMA build-up layer in front of the thin film sensor, as prescribed by ISO 4037-3 [42]. The irradiation field size of the beam is 5 × 5 cm^2. After the setup, the researcher exits the Linacs bunker, and in accordance with a radiation safety policy, waits 60 seconds after the exposure before entering the bunker again. CCTV footage of the bunker and a monitor in the control room that shows the electrometer readings are used to capture the induced current. With regard to the applied voltages of 0, 1, 2, 3, 4, 5, and 6 V, each measurement was done independently.

2.5 Test for dosimetric fading

The I-V characteristics of the thin film sensor were tested for fading. These measurements were performed for post-irradiation of the thin films to high-energy X-rays. The I-V characteristics measurement was carried out at an interval of 0, 1, 2, 15, and 30 days after irradiation respectively. At the end of the I-V characteristics measurements, the values of measured current were normalised to values of day 0 using Equation (1):

$$Normalisation = \frac{I_x}{I_{0x}} \times 100\% \quad (1)$$

where I_x is the measured current at a given day for x voltage and I_{0x} is the measured current at day 0 for x voltage. The normalised values are presented in percentages.

3. Results and discussion

The FESEM images of $(ZnO)_{0.2}(TeO_2)_{0.8}$ thin film are shown in **Figure 2a**. The FESESM was used to image and identify the morphology of the film taken at 50,000× magnification. As we know, ZnO and TeO_2 have a hexagonal and tetragonal structure, respectively, and the FESEM image showed a non-uniform distribution of clustered structures. As

shown in **Figure 2a**, the TeO_2-doped ZnO thin layers are stacked together. As a result, the nanoparticles within the film are seen agglomerated separately in the FESEM image of the film. The nanoparticles are non-uniform in shape, and the grains are non-crystalline and non-uniform. Similar non-uniform surface morphology was reported by Dobri et al. [43] for TeO_2 thin films, Shirpay and Bagheri [44] for $MoTeO_2$ binary thin films, Urfa et al. [45] for ZnO nanoparticles, and Park et al. [46] for TeO_2-core/TiO_2-shell nanowires. Although the samples in the current and previous studies have non-identical morphology and the data differed due to differences in sample preparation, method of deposition, the thickness of the film, chemical sample and post-deposition treatment condition [25,47,48].

The chemical composition of the film was carried out with an energy-dispersive X-ray spectrometer (EDX) during FESEM anaysis. **Figure 2b** shows the EDX spectrum of the $(ZnO)_{0.2}(TeO_2)_{0.8}$ thin film nanostructure, revealing the existence of Te, Zn, and O peaks. After the quasi-quantitative determination of the EDX spectrum, the weight percentages of Te, Zn, and O were 8.09, 5.66, and 28.54, respectively, and the atomic percentages of Te (K), Zn (K), and O were 2.04, 2.78, and 57.32, respectively. It is demonstrated that the purity of the fabrication is high without the other residues such as Si, Ca, and Na derived from the soda-lime glass substrate and Pt buffer layer coating for the FESEM analysis. Traces of Fe in a negligible amount were seen, which might have found their way into the film during Pt coating for FESEM examination. The soda-lime glass substrate residues are relatively high in the EDX spectrum, not as constituents of the film but because of the thin nature of the film (a thickness of 375 nm), which enables the electron to interact with the glass substrate. It is also supposed that the ratio of Zn/O and Te/O_2 is less than 1, compared with the perfect chemical stoichiometry of ZnO and TeO_2. These results reveal that there is some oxygen vacancy in the ZnO/TeO_2 thin film. Similar observations have been reported by Silambarasan et al. [49] and Shanmugam et al. [50].

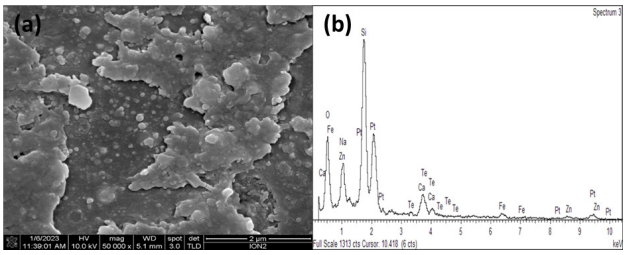

Figure 2. (a) FESEM image of $(ZnO)_{0.2}(TeO_2)_{0.8}$ thin film (b) EDX spectrum of $(ZnO)_{0.2}(TeO_2)_{0.8}$ thin film.

The structural properties of the $(ZnO)_{0.2}(TeO_2)_{0.8}$ thin film were studied by XRD measurement shown in **Figure 3**. The as-deposited thin film is non-crystalline (amorphous) in nature. The pattern shows a highly concentrated weak diffraction peak present at about 23.25° belonging to the diffraction pattern of the α-phase TeO_2 (α-TeO_2, JCPDS card 78-1713) with preferred orientation along (110) direction. A similar XRD diffraction spectrum was reported by Jeong et al. [51] for the dual active layer of IGZO thin film transistor, Khan et al. [52] for as-deposited multilayer ZnO/TiO_2 thin films and Carotenuto et al. [53] for tellurium film. A weak intensive peak at 68.32° is seen which may be due to the wurtzite structure of ZnO (JCPDS card 043-0002) with preferred orientation along (201) direction as reported by Shatnawi et al. [54]. Both α-TeO_2 and wurtzite ZnO phases were already present in the as-deposited $(ZnO)_{0.2}(TeO_2)_{0.8}$ thin film.

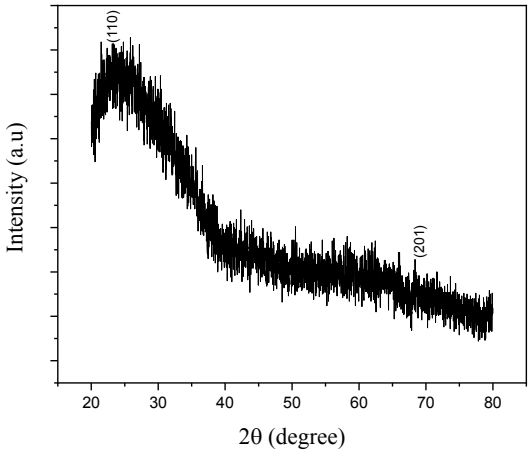

Figure 3. XRD pattern of $(ZnO)_{0.2}(TeO_2)_{0.8}$ thin film.

Figure 4 shows typical current versus applied voltage plots for the $(ZnO)_{0.2}(TeO_2)_{0.8}$ thin film sensor exposed to various X-ray doses. The dependence

of the current density at different voltages applied to the thin film structure is shown in **Figure 5**. Clearly, the current density has been found to increase linearly with the X-ray dose over a range of 0–250 cGy (**Figure 4**). The sensitivities of the $(ZnO)_{0.2}(TeO_2)_{0.8}$ thin film device were calculated using current density versus dose plot and was found to be in the 0.37-0.94 mA/cm^2/Gy range.

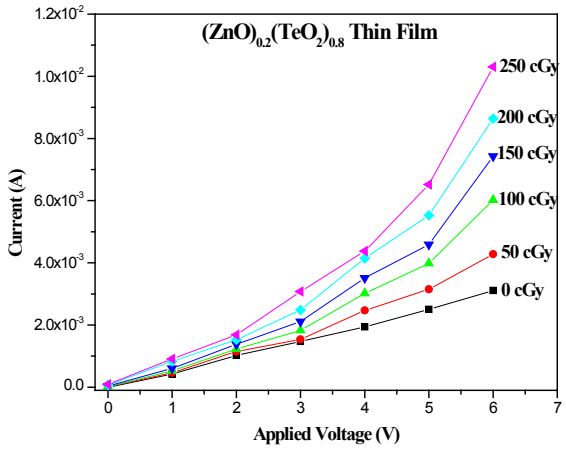

Figure 4. Current versus Voltage (I-V) plot at different X-ray Dose for $(ZnO)_{0.2}(TeO_2)_{0.8}$ thin film device.

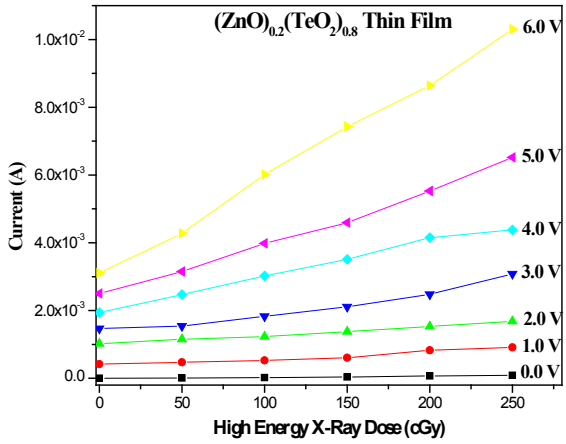

Figure 5. Current versus High Energy X-ray Dose (I-D) plot at different applied Voltages for $(ZnO)_{0.2}(TeO_2)_{0.8}$ thin film device.

The current versus voltage (I-V) characteristics of the prepared thin films show an enhancement in the values of current under a forward-biassed condition. During the transmission of X-rays through thin films, defects are induced, resulting in the disordered structure of the film. This is attributed to the energy transfer from the X-ray radiation dose to the electrons that makes the electron move from the valence band to the conduction band, creating electron-hole pairs that increase the conductivity of the film [16].

The test for fading of the I-V characteristics of the post-X-ray irradiation for days 0, 1, 2, 15, and 30 normalised to day 0 was analyzed. The mean relative readings obtained are in the order of day 0 > day 15 > day 30 > day 1 > day 2. Firstly, there was a decline in the induced current on days 1 (81.59%) and 2 (89.5%). An abrupt increase was observed on day 15 (99.20%) and a slight decrease on day 30 (93.30%). These abnormalities could be attributed to the introduction of ZnO into the lattice of TeO_2 in a small amount (20% ZnO). The semiconducting behaviour of the film indicates that the irradiation with high-energy X-ray radiation affects the microstructure of the film [38-42].

The healing effect may also be responsible for the rise in current density [55]. There are usually some intrinsic flaws created during the film deposition. As a result of the interaction between X-ray radiation and the film, the film's structure will become disorganised throughout transmission through the film. The number of defects (induced plus residual intrinsic defects) is less than the number of intrinsic defects due to the recombination of defects, which lowers the thin film's resistivity and results in an increase in current [56]. At small doses, these thin films have a fine homogeneous grain structure without any large pores. The healing effect may also be used to understand how the critical dosage depends on the film thickness [48]. Therefore, compared to thinner films, larger films require substantially greater radiation doses for healing [29].

Transparent conducting oxide thin layer conductivity control is still a difficult task [38,39]. The optical and electrical characteristics of semiconductor thin film devices can be strongly impacted by even very low concentrations of impurities (down to 10^{-14} cm^3 or 0.01 ppm) and native point defects [57-59]. In order to effectively manage the conductivity in a thin film device, it is essential to comprehend the function of native point defects (such as vacancies, interstitials, and antisites), the integration of impurities, and

the doping of two or more oxides. It has long been confirmed that oxygen vacancies or interstitials are what produce the unintended n-type conductivity in ZnO [60]. Pure ZnO thin films are not resistant to corrosive conditions; for instance, the adsorption of O_2 reduces the film's electrical conductivity and alters the surface shape [61]. In order to make the ZnO system resistant to such changes, doping ZnO with TeO_2 has been examined in this work, leading to the development of an intriguing family of materials based on doped ZnO.

4. Conclusions

This work involves the synthesis, doping, film deposition, structural, morphological study, and the current-voltage characteristics during high energy X-ray exposure of a $(ZnO)_{0.2}(TeO_2)_{0.8}$ thin film sensor prepared by the spray pyrolysis method. The XRD pattern revealed the non-crystalline (amorphous) nature of the film. The FESEM image shows non-uniform shapes of nanoparticles that are agglomerated separately. The current density has been found to increase linearly with the X-ray dose over a range of 0-250 cGy. The sensitivity of the film device was estimated and found to be in the range of 0.37-0.94 $mA/cm^2/Gy$. There is a slight decline in the film conductivity over a period of 30 days after exposure to high-energy X-rays. The semiconducting behaviour of the film indicates that the irradiation with high-energy X-ray doses affects the microstructure of the film. These results are expected to be beneficial for fabricating cheap and practical X-ray detection applications.

Conflict of Interest

There is no conflict of interest.

Acknowledgement

The authors wish to thank the Nigeria government through the Tertiary Education Trust Fund (TET Fund) for funding this research study.

References

[1] Yahaya, I., Mundi, A.A., Mustapha, I.M., et al., 2019. Evaluation of concentration of copper, lead, and zinc in different brands of cigarette sold in Keffi main market of Nasarawa State, Nigeria. Asian Journal of Advance Research and Reports. 4, 1-7. doi: 10.9734/ajarr/2019/v4i430119.

[2] Nie, Y., Xie, Y., Zheng, Y., et al., 2021. Preparation of ZnO/Bi_2O_3 composites as heterogeneous thin film materials with high photoelectric performance on FTO base. Journal of Coatings. 11(9). doi: 10.3390/coatings11091140.

[3] Younus, I.A., Ezzat, A.M., Uonis, M.M., 2021. Preparation of ZnTe thin films using chemical bath deposition technique. Journal of Nanocomposites. 6(4), 165-172. doi: 10.1080/20550324.2020.1865712.

[4] Idris, M.M., Ubaidullah, A., Sulayman, M.B., et al., 2021. Assessment of gamma background exposure levels in some selected residential houses in FCT Abuja , Nigeria. Journal of Radiation and Nuclear Application. 254(3), 251-254.

[5] Edrine, T., Muhammad, D., Ahmad, N.S.Y., et al., 2019. A review: Photonic devices used for dosimetry in medical radiation. Journal of Sensors. 19(1), 2226.

[6] Muchuweni, E., Sathiaraj, T.S., Nyakotyo, H., 2017. Synthesis and characterization of zinc oxide thin films for optoelectronic applications. Journal of Heliyon. 3(4), e00285. doi: 10.1016/j.heliyon.2017.e00285.

[7] Idris, M.M., Olarinoye, I.O., Kolo, M.T., et al., 2022. Transparent conducting oxides thin film dosimetry: Present and the future. Journal of Radiation and Nuclear Application. 7(1), 49-58.

[8] Chen, Y. (editor), 2018. Review of ZnO transparent conducting oxides for solar applications. IOP Conference Series on Material Science and Engineering; 2018 May 25-27; Nanchang, China; UK: IOP Publishing. doi: 10.1088/1757-899X/423/1/012170.

[9] de Godoy, M.P.F., de Herval, L.K.S., Cotta, A.A.C., et al., 2020. ZnO thin films design: The

role of precursor molarity in the spray pyrolysis process. Journal of Material Science: Material in Electronics. 31(20), 17269-17280. doi: 10.1007/s10854-020-04281-y.

[10] Robertson, J., Falabretti, B., 2011. Electronic structure of transparent conducting oxides, 6th ed. Springer US: Boston.

[11] Ilin, E., 2014. Study of the synthesis machanisms and optical properties of ZnO nanomaterials obtained by supercritical fluids route [HAL thesis]. France: Université de Bordeaux.

[12] Eskalen, H., Kavun, Y., Kerli, S., et al., 2020. An investigation of radiation shielding properties of boron doped ZnO thin films. Journal of Optical Materials. 105, 109871. doi: 10.1016/j.optmat.2020.109871.

[13] Khan, Z.R., Khan, M.S., Zulfequar, M., et al., 2011. Optical and structural properties of ZnO thin films fabricated by Sol-Gel method. Journal of Material Sciences and Applications. 2(5), 340-345. doi: 10.4236/msa.2011.25044.

[14] Kariper, A., 2019. Crystalline TeO_2 thin film with chemical bath deposition. Indian Journal of Pure and Applied Physics. 57(3), 175-179.

[15] Bontempo, L., Dos Santos Filho, S.G., Kassab, L.R.P., 2020. Process oxygen flow influence on the structural properties of thin films obtained by co-sputtering of (TeO_2)x-ZnO and Au onto Si substrates. Journal of Nanomaterials. 10(9), 1-16. doi: 10.3390/nano10091863.

[16] Sudha, A., Maity, T.K., Sharma, S.L., et al., 2018. An extensive study on the structural evolution and gamma radiation stability of TeO_2 thin films. Journal of Material Science in Semicondor Processing. 74, 347-351. doi: 10.1016/j.mssp.2017.10.018.

[17] Nistor, M., Rougier, A., 2011. Low temperature Si doped ZnO thin films for transparent conducting oxides. Journal of Solar Energy Materials and Solar Cells. 95, 2357-2362. doi: 10.1016/j.solmat.2011.04.006.

[18] Manzi, J.A., 2016. Zinc precursor synthesis and the aerosol assisted chemical vapour deposition of zinc oxide thin films [PhD thesis]. London: Department of Chemistry University College London Christopher Ingold Laboratories.

[19] Kariper, I.A., 2019. Crystalline TeO_2 thin film with chemical bath deposition. Indian Journal of Pure and Applied Physics. 57(2), 411-419. doi: 10.1007/s00339-021-04344-9.

[20] Bhat, J.S., Maddani, K.I., Karguppikar, A.M., et al., 2007. Electron beam radiation effects on electrical and optical properties of pure and aluminum doped tin oxide films. Journal of Nucear Instruments and Methods in Physics Research B. 258, 369-374. doi: 10.1016/j.nimb.2007.02.074.

[21] Paquin, F., Rivnay, J., Salleo, A., et al., 2015. Multi-phase semicrystalline microstructures drive exciton dissociation in neat plastic semiconductors. Journal of Material Chemistry C. 3, 10715-10722. doi: 10.1039/b000000x.

[22] Arockiam, C.J., Ananthanarayanan, R., Srinivasan, P., et al., 2021. Room temperature selective sensing of benzene vapor molecules using mixed oxide thin film of zinc oxide and cadmium oxide. Journal of Material Science in Semiconduting Processing. 132, 105930. doi: 10.1016/j.mssp.2021.105930.

[23] Saadie, J.H., 2015. Influence of thickness on electrical and optical properties of tellurium thin films deposited by chemical spray pyrolysis. International Journal of Applied Mathematics, Electronics and Computers. 3(2), 96-101.

[24] Xu, S.H., Huang, J.Y., Fei, G.T., et al., 2021. Sol-Gel preparation of high transmittance of infrared antireflective coating for TeO_2 crystals. Journal of Infrared Physics and Technology. 118, 103881. doi: 10.1016/j.infrared.2021.103881.

[25] Patil, N.B., Nimbalkar, A.R., Patil, M.G., 2018. ZnO thin film prepared by a sol-gel spin coating technique for NO_2 detection. Journal of Material Sciences and Engineering B. 227(2), 53-60. doi: 10.1016/j.mseb.2017.10.011.

[26] Özgür, Ü., Ya, I., Alivov, C., et al., 2005. A comprehensive review of ZnO materials and devices. Journal of Applied Physics. 98(4), 1-103. doi: 10.1063/1.1992666.

[27] Look, D.C., 2001. Recent advances in ZnO ma-

terials and devices. Journal of Material Science and Engineering B: Solid-State Materials and Advanced Technology. 80(1-3), 383-387. doi: 10.1016/S0921-5107(00)00604-8.

[28] Kayani, Z.N., Shah, I., Zulfiqar, B., et al., 2017. Structural, optical and magnetic properties of nanocrystalline Co-doped ZnO thin films grown by Sol-Gel. Journal of Applied Physical Sciences. 73(1), 13-21. doi: 10.1515/zna-2017-0302.

[29] Aparna, C., Shetty, P.K., Mahesha, M.G., 2022. Structural optimization of indium oxide thin film for gamma dosimetry applications. Journal of Material Science in Semiconducting Processing. 150, 106931.

[30] Shamma, K., Aldwayyan, A., Albrithen, H., et al., 2021. Exploiting the properties of TiO_2 thin films as a sensing layer on (MEMS)-based sensors for radiation dosimetry applications. Journal of AIP Advanced. 025209, 1-9. doi: 10.1063/5.0032353.

[31] Ogundare, F.O., Olarinoye, I.O., 2015. He + induced changes in the surface structure and optical properties of RF-sputtered amorphous alumina thin films. Journal of Non Crystalline Solids. 432(Part B), 292-299. doi: 10.1016/j.jnoncrysol.2015.10.026.

[32] Olarinoye, I.O., Ogundare, F.O., 2017. Optical and microstructural properties of neutron irradiated RF-sputtered amorphous alumina thin films. Journal of Optics. 134, 66-77.

[33] Jeong, W.S., Kim, J., Seok, J., et al., 2016. Indium oxide (In_2O_3) nanoparticles induce progressive lung injury distinct from lung injuries by copper oxide (CuO) and nickel oxide (NiO) nanoparticles. Journal of Archieves of Toxicology. 90(4), 817-828.

[34] Li, Q., Zhou, C., Nie, S., et al., 2021. Durable Flexible Polymer-Encapsulated Cs_4PbI_6 Thin Film for High Sensitivity X-ray detection. Journal of Nano Letters. 21(24), 10279-10283.

[35] Aldawood, S.M., AlTalib, S., AlGarawi, O.M., et al., 2022. Gamma ray effects on the properties of PbI_2 thin films. Journal of Radiation Physics and Chemistry. 193, 110003.

[36] Chauhan, V.R., Gupta, D., Upadhyay, S., et al., 2022. Influence of high dose gamma radiation on optical, physico-chemical and surface morphology properties of nanocrystalline ZrO_2 thin films. Journal of Optical Materials. 126, 112125.

[37] Wang, S., Uprety, S., Mirkhani, V., et al., 2022. The effect of gamma-ray irradiation on the electrical characteristics of sol-gel derived zinc tin oxide thin film transistors. Journal of Solid-State Electronics. 191, 108270.

[38] Sen, M.A., Manir, S.K., Dutta, M.S., et al., 2020. Influence of total absorbed dose of Co-60 γ-radiation on the properties of h-MoO_3 thin films. Journal of Thin Solid Films. 693, 137700.

[39] Thabit, M.A., Kabir, H.A., Ismail, N.A., et al., 2022. Development of Ag-doped ZnO thin films and thermoluminescence (TLD) characteristics for radiation technology. Journal of Nanomaterials. 12(17), 3068.

[40] Ali, A.M.A., Ahmed, N.M., Mohammad, S.M., et al., 2019. Effect of gamma irradiation dose on the structure and pH sensitivity of ITO thin films in extended gate field effect transistor. Journal of Results in Physics. 12, 615-622.

[41] Maity, T.K., Sharma, S.L., Chourasiya, G., 2012. The real-time gamma radiation dosimetry with TeO_2 thin films. Journal of Radiation Measurements. 47, 145-148. doi: 10.1016/j.radmeas.2011.11.008.

[42] Dubeau, J., Sun, J., Leroux, N., et al., 2023. The HP (3, α) dose response of direct reading survey meters. Journal of Radiation Measurements. 160, 106891. doi: 10.1016/j.radmeas.2022.106891.

[43] Bataliotti, M.D., Costa, F.B., Minussi, F.B., et al., 2022. Characterization of tellurium dioxide thin films obtained through the Pechini method. Journal of Sol-Gel Science and Technology. 1, 378-385. doi: 10.1007/s10971-022-05844-7.

[44] Shirpay, A., Mohagheghi, M.M.B., 2020. Investigation of structural, optical and thermoelectric properties of 2H—$MoTe_2$ and MoO_3—TeO_2 thin films. Journal of Physica B: Condense Matter. 587, 412141. doi: 10.1016/j.physb.2020.412141.

[45] Urfa, Y., Çorumlu, V., Altındal, A., 2021. Gam-

ma ray irradiation dose dependent methanol sensing with ZnO nanoparticles. Journal of Material Chemistry and Physics. 264, 124473. doi: 10.1016/j.matchemphys.2021.124473.

[46] Park, S., An, S., Lee, C., 2013. Structure and photoluminescence properties of TeO_2-core/TiO_2-shell nanowires. Journal of Physica E: Low-dimensional Systems and Nanostructures. 54, 5-8. doi: 10.1016/j.physe.2013.05.023.

[47] Ambedkar, A.K., Singh, M., Kumar, V., et al., 2020. Structural, optical and thermoelectric properties of Al-doped ZnO thin films prepared by spray pyrolysis. Journal of Surfaces and Interfaces. 19, 100504. doi: 10.1016/j.surfin.2020.100504.

[48] Maity, T.K., Sharma, S.L., 2011. Effects of gamma irradiation on electrical, optical and structural properties of tellurium dioxide thin films. Indian Journal of Pure and Applied Physics. 49(9), 606-612.

[49] Silambarasan, M., Saravanan, S., Soga, T., 2015. Raman and photoluminescence studies of A and Fe-doped ZnO nanoparticles. International Journal of ChemTech Research. 7(3), 1644-1650.

[50] Shanmugam, N., Suthakaran, S., Kannadasan, N., et al., 2015. Synthesis and characterization of Te doped ZnO nanosheets for photocatalytic application. Journal of Heterocyclics.1(1), 1-6. doi: 10.33805/2639-6734.105.

[51] Jeong, S., Kim, M., Lee, S., et al., 2014. Dual active layer a-IGZO TFT via homogeneous conductive layer formation by photochemical H-doping. Journal of Nanoscale Research Letters. 9(1), 1-9. doi: 10.1186/1556-276X-9-619.

[52] Khan, M.I., Bhatti, K.A., Qindeel, R., et al., 2016. Investigations of the structural, morphological and electrical properties of multilayer ZnO/TiO_2 thin films, deposited by Sol-Gel technique. Journal of Results in Physics. 6, 156-160. doi: 10.1016/j.rinp.2016.01.015.

[53] Carotenuto, G., Palomba, M., De Nicola, S., et al., 2015. Structural and photoconductivity properties of tellurium / PMMA films. Journal of Nanoscale Research Letters. 10, 313. doi: 10.1186/s11671-015-1007-z.

[54] Shatnawi, M., Alsmadi, A.M., Bsoul, I., et al., 2016. Influence of Mn doping on the magnetic and optical properties of ZnO nanocrystalline particles results in physics influence of Mn doping on the magnetic and optical properties of ZnO nanocrystalline particles. Journal of Results in Physics. 6, 1064-1071. doi: 10.1016/j.rinp.2016.11.041.

[55] Maity, T.K., Sudha, A., Sharma, S.L., et al., 2016. High sensitivity gamma radiation dosimetry using $(In_2O_3)_{0.1}(TeO_2)_{0.9}$ thin films. Journal of Radiation Protection Environment. 1, 135-138. doi: 10.4103/0972-0464.176156.

[56] Sudha, A., Sharma, S.L., Gupta, A.N., 2019. Achieving sensitive and stable indium oxide thin films for gamma radiation monitoring. Journal of Sensors Actuators A: Physica. 285, 378-385. doi: 10.1016/j.sna.2018.10.015.

[57] Chen, C.J., Chandel, A., Thakur, D., et al., 2021. Ag modified bathocuproine: ZnO nanoparticles electron buffer layer based bifacial inverted-type perovskite solar cells. Journal of Organic Electronics. 92, 106110. doi: 10.1016/j.orgel.2021.106110.

[58] Zygmanski, P., 2016. A self-powered thin-film radiation detector using intrinsic high-energy current. Journal of Medical Physics. 43(1), 4-15.

[59] Paraguay D.F., Estrada L.W., Acosta N.D.R., et al., 1999. Growth, structure and optical characterization of high quality ZnO thin films obtained by spray pyrolysis. Journal of Thin Solid Films. 350(1), 192-202. doi: 10.1016/S0040-6090(99)00050-4.

[60] Salam, S., Islam, M., Akram, A., 2012. Sol-gel synthesis of intrinsic and aluminum-doped zinc oxide thin films as transparent conducting oxides for thin film solar cells. Journal of Thin Solid Films. 529, 242-247. doi: 10.1016/j.tsf.2012.10.079.

[61] Al-maiyaly, B.K.H., 2018. Effect of gamma ray irradiation on structural and optical properties of ZnO thin films. Journal of Pure and Applied Science. 28(3).

BILINGUAL PUBLISHING GROUP

Non-Metallic Material Science

https://journals.bilpubgroup.com/index.php/nmms

REVIEW

Carbon Fiber from Biomass Sources: A Comprehensive Review

Md. Touhidul Islam*, Md. Shahin Howlader, Din Mohamad Shuvo, Md. Kamal Uddin

Department of Textile Engineering, Mawlana Bhashani Science and Technology University, Tangail, Dhaka, 1902, Bangladesh

ABSTRACT

Global energy demand is rising, fossil fuel prices are rising, fossil fuel reserves are running out, and fossil fuel use contributes to the greenhouse effect. As a clean alternative source of energy to fossil fuels, biomass is becoming more and more essential. Carbon fiber (CF), often known as graphite fiber, is a thin, strong, and adaptable material utilized in both structural (capacity) and non-structural applications (e.g., thermal insulation). Precursors are the raw materials used to create carbon fiber, which is mostly derived from fossil fuels. Because of the high cost of precursors and manufacture, carbon fiber has only found employment in a few numbers of high-performance structural materials (e.g., aerospace). To reduce the price of CF and reliance on fossil fuels, numerous alternative precursors have been studied throughout the years, including biomass-derived precursors such as rayon, lignin, glycerol, and lignocellulosic polysaccharides. This study's goal is to present a detailed study of biomass-derived CF precursors and their market potential. The authors look into the viability of producing CF from these precursors, as well as the state of technology, potential applications, and cost of production (when data are available). We go over their benefits and drawbacks. We also talk about the physical characteristics of CF made from biomass and contrast them with CF made from polyacrylonitrile (PAN). Additionally, we go into bio-based CF manufacturing and end-product concerns, logistics for biomass feedstock and plant sites, feedstock competition, and risk-reduction techniques. This paper offers a comprehensive overview of the CF potential from all biomass sources and can be used as a resource by both novice and seasoned professionals who are interested in producing CF from non-traditional sources.

Keywords: Carbon fibre; Polyacrylonitrile; Biomass; Lignocellulosic

*CORRESPONDING AUTHOR:
Md. Touhidul Islam, Department of Textile Engineering, Mawlana Bhashani Science and Technology University, Tangail, Dhaka, 1902, Bangladesh; Email: te17035@mbstu.ac.bd

ARTICLE INFO
Received: 17 March 2023 | Revised: 27 March 2023 | Accepted: 29 March 2023 | Published Online: 7 April 2023
DOI: https://doi.org/10.30564/nmms.v5i1.5572

CITATION
Islam, M.T., Howlader, M.S., Shuvo, D.M., et al., 2023. Carbon Fiber from Biomass Sources: A Comprehensive Review. Non-Metallic Material Science. 5(1): 14-26. DOI: https://doi.org/10.30564/nmms.v5i1.5572

1. Introduction

Carbon fibers are fibrous carbonaceous materials having a diameter of 5-10 μm. Carbon fibers are filaments, lines, or reels that contain more than 92 percent carbon and are normally in a nongraphite condition, according to the International Union of Pure and Applied Chemistry (IUPAC) [1]. This means that carbon is defined as a two-dimensional long-range arrangement of carbon atoms in planar hexagonal networks with no crystalline structure in the third direction except for some parallel stacking [2]. Graphite fiber, often known as carbon fiber (CF), is a strong, lightweight material that can be used for both structural and non-structural applications (e.g., thermal insulation). Most carbon materials demonstrate excellent stability and high power density when used as supercapacitor electrodes; nevertheless, their specific capacitance and energy density are relatively low, which cannot meet the high energy requirements for practical applications [3]. In this case, carbon materials with a high specific surface area, a reasonable pore size distribution, and desired nanostructure are critically demanded [4]. Carbon fiber, a newly developed synthetic material that is commonly utilized in the production of advanced composites has a wide range of applications in the automotive, aerospace, and electronics industries [5]. Carbon materials have long been suitable materials in energy storage due to their superior electrical conductivity, easy fabrication, physical and chemical sustainability, and high surface area among several supercapacitor electrode materials [6]. Carbon fibers have great stiffness, high durability, light weight, strong chemical stability, high-temperature tolerance, and minimal thermal expansion as its key characteristics [7]. To make a composite, carbon fibers are frequently mixed with other materials. It generates carbon-fiber-reinforced polymer (commonly referred to as carbon fiber) when penetrated with a plastic resin and baked. It has a very high-grade ratio and is exceedingly rigid, but slightly brittle. Carbon fibers can also be combined with other materials like graphite to create reinforced carbon-carbon composites with a feverish temperature tolerance. However, when compared to similar fibers such as glass fiber, basalt fibers, or plastic fibers, they are quite pricey [8]. To make a carbon fiber, carbon atoms are bonded together in crystals that are aligned parallel to the fiber's long axis, resulting in a fiber with a high strength-to-volume ratio (in other words, it is strong for its size). Thousands of carbon fibers are bundled together to create a tow that may be used alone or woven into a fabric [9].

2. Synthesis of carbon fiber

Organic polymers, which are long chains of molecules linked together by carbon atoms, are used to make carbon fiber. The polyacrylonitrile (PAN) method produces most of the carbon fibers (about 90%). A minor percentage (about 10%) is made using rayon or the petroleum pitch method [10]. The effects, properties, and grades of carbon fiber are created by the gases, liquids, and other components employed in the manufacturing process. Carbon fiber makers create materials using proprietary formulas and combinations of raw components, and they treat these compositions as trade secrets in general. Pitch, obtained from petroleum or coal, and polyacrylonitrile have been the most popular types of precursor materials used to make carbon fiber commercially since the 1960s. All the non-renewable materials are discussed in the following sub-section.

2.1 PAN

PAN-based carbon fibers with poor mechanical qualities were first manufactured in 1959 in Osaka, Japan, boosting the carbon fiber industry's development. Despite facing numerous challenges in generating high-strength and high-modulus carbon fiber, the Japanese business TORAY has reached world-leading levels of performance in this industry [11]. PAN is petroleum-based linear polymer carbon fibers made from PAN are primarily made in two processes. The first stage is to make polyacrylonitrile precursor, which consists mostly of monomer polymer-

ization and the preparation of spinning liquid, which is then spun further. This is an important first step in the manufacture of carbon fiber since the quality of the precursor dictates the carbon fiber's performance. The precursor is pre-oxidized and carbonized in the second stage [12]. Carbon fiber made from PAN, on the other hand, is expensive, thus its use is confined to high-performance structural components [13]. For example, due to their outstanding mechanical properties and high production, CFs based on PAN precursor are the most important in the market [14]. However, as fossil energy is rapidly exhausted, not only will the cost of CFs based on non-renewable energy rise, but environmental pollution from the production of toxic gases (e.g. hydrogen cyanide) using PAN as a precursor will also rise [15]. Most carbon fibers used are made from polyacrylonitrile (PAN) precursor fibers, which are the best precursors for high-performance carbon fiber production [16]. Thermal stabilization and carbonization are the two processes in the manufacture of carbon fiber from PAN precursor fiber [17]. In an oxygen environment, the stabilization procedure is usually carried out under stress at temperatures ranging from 200 to 300 degrees Celsius [18]. Various exothermic chemical events, such as cyclization, dehydrogenation, oxidation, and cross-linking, cause PAN to undergo chemical modifications that result in an increase in density during this process. The cyclization process converts a linear polymer into an infusible ladder polymer, which gives the polymer thermal stability and prevents melting during the subsequent carbonization process (which takes place at temperatures between 700 and 1500 degrees Celsius in a nitrogen atmosphere) [19]. As a result, the stabilization process is the most important factor in determining carbon fiber's mechanical properties [20]. To date, most studies on the PAN stabilization process have mostly focused on thermal stability, with only a few researchers actively investigating the effect of radiation on the PAN precursor's thermal stabilization. Furthermore, when the PAN precursor fiber is stabilized by electron beam irradiation (EBI) and heat treatments, the stabilization period (2-3 h) can be decreased because of pre-stabilization by EBI and thermal treatments [21].

2.2 Pitch

Pitch is the common name for a tarry substance with a high carbon content that is particularly viscous at ambient temperature. It's a complicated mix of hundreds of aromatic hydrocarbons and heterocyclic molecules with a molecular weight of 300-400. It can be made from natural sources such as petroleum and coal by destructive distillation, or from synthetic sources such as polyaromatic chemicals and polymers by pyrolysis. Pitch composition varies greatly depending on the tar source and processing circumstances. Pitch can contain more than 80% carbon, and the quality of the result CF improves as the aromaticity rises. The bottoms of catalytic crackers, steam cracking of naphtha and gas oils, and wastes from other refinery processes can all be used to make petroleum pitch [22]. Before being used in the CF sector, crude products normally go through several refining processes. Coal tar is produced as a by-product of the coking of bituminous coals to make cokes. Distillation and heat treatment are used to extract coal-tar pitch from coal tar. The pitch is the residue left over after the heavy oil fractions have been removed. Coal-tar pitch has a higher aromatic content than petroleum pitch [23]. It does, however, have a significant solid content, which leads to filament breakage during extrusion and heat treatment. As a result, petroleum pitch is favoured for the manufacturing of CF. Isotropic and mesophase pitch are the two primary forms of pitch used in the pitch-based precursor business. The GP grade of pitch CF is made with isotropic pitches [24]. They are not graphitic, and their characteristics are inferior to those of the HP grade. A unique treatment technique is required to convert the pitch to mesophase grade in order to make HP grade. Mesophase grade is graphitic in nature and optically anisotropic. To make a product appropriate for melt spinning, the isotropic pitch must be processed, filtered to eliminate solid particles, and have low volatility [25]. The low volatility components of the pitch are removed using a wiping film evaporator, and the molten pitch

is filtered to remove solid contaminants. Domains of very parallel, platelike molecules develop and consolidate during the creation of the mesophase until 100 percent anisotropic material is formed. Several strategies for the synthesis of mesophase pitch have been researched over the years: (a) pyrolysis of pitch, (b) solvent extraction, (c) hydrogenation, and (d) catalytic modification. For the best control of the processing parameters and pitch quality, the catalytic technique is preferred in pitch pre-treatment [26]. It is claimed that a spinning pitch should contain 40%-90% mesophase with domain sizes greater than 200 m, resulting in a fiber with a highly orientated structure. Domain sizes of less than 100 m have been found to be unsuitable for spinning. Melt spinning in an extruder produces pitch-based predecessors. Because of the rheological qualities of molten pitch, melt spinning is challenging, and very precise processing conditions are necessary. The viscosity of the mesophase is very temperature-dependent, and the jet temperature should be precisely regulated, as a change of 3.5 °C at the jet face causes a 15% change in diameter [27]. Due to poor viscosity, too high a temperature causes thermal deterioration of the pitch or dripping. Melting the precursor, extrusion via a spinneret capillary, and drawing the fibers as they cool are the three phases in the melt-spinning process. Solid pitch chips have been fed into the hopper of a screw extruder with off-gassing apertures and evenly heated, resulting in a uniform feed of molten pitch to the filter and then spinneret at the extruder's outlet. To avoid interfilamentous fusing, pitch spinnerets have a 130 Fiber Technology for Fiber-Reinforced Composites multiplicity of holes, which must be spaced roughly 1.1 mm apart. As the molten pitch flows through the capillaries, some initial orientation occurs. It is cooled by quenching air after coming from the capillaries [28]. The solid fiber is pulled before windup while it is still hot to produce a highly oriented precursor fiber. Any subsequent carbonizing procedure will not require a further drawing of this precursor fiber. Due to the low strength of the as spun mesophase pitch, fiber handling in the windup is challenging (tensile strength around 0.04 GPa). Mesophase carbon fibers have a diameter of 10-15 m, whereas PAN carbon fibers have a diameter of 5-7 m. This is due to the preference for bigger diameter mesophase precursor fibers for easier handling and higher carbon yield, resulting in a lower size decrease in the carbonization process. It is claimed that a processing speed of up to 1000 m/min can be achieved [29].

The microstructure of spun mesophase pitch precursor fibers is made up of microdomains of well-oriented polyaromatic molecules. Discotic nematic liquid crystal microstructures are the name given to these microstructures.

2.3 Carbon fiber from renewable biomass sources

Carbon fiber made from biomass could be less expensive to produce and have more environmental benefits than carbon fiber made from natural gas or petroleum [30]. Consequently, developing a process for producing low-cost CFs based on renewable, non-toxic, and sustainable resources is both essential and realistic in the context of climate change mitigation and adaptation. Because of the advantages of renewable and low-cost properties, bio-mass resources such as cellulose, lignin, Glycerol, Lignocellulosic Sugars and wood are attractive precursors for the preparation of CFs [31]. Scientists and engineers are motivated to create these novel materials because the use of biomass resources for a variety of electrode materials shows that a sizable portion of the intricate functionality of living systems is founded on an intricate hierarchical organization from the manometer to the macroscopic scale. Because of their abundant availability and added value gained from their renewable and biodegradable nature, biomass sources are becoming increasingly essential. Various bio-renewable resources have been developed as alternative materials for CFs in recent years [32]. All of these are discussed in the following sub-sections.

Cellulose

The manufacture of cellulosic fibers is well known; rayon, the first CF to hit the market in the 1960s, is made from cellulose-based natural materials (such as wood pulp, cotton linters,

leaves, and the inner pith of bamboo plants) that are chemically processed to create semi-synthetic fibers [33]. All three of these rayon types—viscose, modal, and lyocell—are made differently and have different properties. Lyocell is frequently marketed under the brand name TENCEL and is produced by the Lenzing Group in Austria. PAN-based CF has superseded rayon-based CF in most applications due to its superior performance in various areas, particularly tensile strength [34]. Furthermore, although having a cheaper raw material cost, rayon-based CF has a higher total cost due to a low char yield (20%-25%) following carbonization. These qualities can be improved by stress graphitization at elevated temperatures, but this raises the cost of the fiber even more, making it less appealing. Despite not being used for structural purposes, rayon-based CF is still used in the rocket and missile industries for ablative purposes like re-entry vehicle nose tips, heat shields, solid rocket motor (SRM) nozzles, and exit cones [35]. Rayon-based CF can endure the elevated temperatures and corrosive gases of SRM operation, as well as the feverish temperatures created by missile re-entry systems' aerodynamic heating. Due to low demand, commercial manufacturing of rayon-based CF is limited (approximately 1%-2% of overall CF production). RUE-SPA-Khimvolokno in Belarus is the world's largest rayon-based CF producer. Precursor stabilization (low-temperature oxidation), carbonization (longitudinal orientation and crystalline ordering development), and graphitization (optional for high modulus) are the three basic steps in the production of rayon-based CF [36]. Natural fibers like cotton and ramie have not been chosen for the production of CF due to their complicated structure, discontinuous filament structure, low degree of orientation, and related pollutants [37]. Advanced processing technology and a search for renewable sources, on the other hand, may open new possibilities for natural fibers as CF precursors in the future. Because of its tremendous flexibility, cellulose (the most prevalent biological macromolecule in nature) is an appealing alternative material for electrospinning to manufacture submicron-diameter CFs. However, due to the low thermal stability of cellulose, direct carbonization of biomass-based CFs is problematic [38]. The typical viscose process is likewise slow, arduous, and complex in the cellulose-based CFs business. It also produces CS_2, H_2S, and heavy metals, all of which are detrimental to the environment [39]. As a result, finding a cost-effective and ecologically friendly technique to create regenerated cellulose fibers is desirable. CFs manufactured from regenerated cellulose fibers, such as Lyocell fibers, have been attempted using the CarbaCell method. The Lyocell process uses N-methyl-morpholine-N-oxide (NMMO) as a cellulose solvent, resulting in better fiber qualities such as tenacity, crystallinity, and modulus. High-spinning temperature and solvent recovery are two technical issues with this method [40]. The CarbaCell technique is an alternate approach for reducing hazardous compounds. In this procedure, cellulose carbamates (CC) are stable at room temperature and can be stored for more than a year without losing quality [41].

Lignin

Lignin, which has a high carbon content, exceptional thermal stability, and a huge number of benzene ring structures, is another excellent bio-renewable resource [42]. Furthermore, lignin is a cheap and easily available coproduct of the pulp and papermaking process. However, due to lignin's nonlinear chemical structure and limited flexibility, preparing CFs by spinning independently remains a significant difficulty. Physical blending with petroleum-based polymer or bio-macromolecular as spinning auxiliaries has been used to manufacture lignin-based CFs in a variety of ways [43]. However, during the carbonization process (high-temperature heating under a nitrogen atmosphere), cellulose and lignin molecules containing a considerable amount of oxygen have a high oxidation process weightlessness, resulting in the morphological collapse of biomass-based CFs. When these monolignols polymerize in natural biomass, they produce a racemic, cross-linked, and highly heterogeneous aromatic macromolecule. The proportions of syringyl (S), guaiacyl (G), and p-hydroxyphenol (H) monomers, molecular weights,

degree of branching, isolation methods, and purity all influence the physical and chemical properties of lignin separated from biomass [44]. Most of the lignin produced by the Kraft pulping process and the biofuel business are currently used as low-cost fuel. Future development of processes for biomass utilization may involve a "biorefinery" concept in which wood (biomass) is brought to a mill site and further converted to pulp and paper or, alternatively, to energy, biofuels, and chemicals through processes such as prehydrolysis-kraft, organosolv pulping, steam explosion, autohydrolysis or acid hydrolysis. The alternative techniques, unlike the classic kraft pulping process, are not suited for creating pulp and paper, but they can be developed for other purposes such as cellulose, hemicelluloses, and lignin synthesis. Chemical modification of the lignin might be done during the process or afterward. Lignin will most likely be widely available in vast amounts in the future [45]. Although lignin is a great biofuel, new applications in higher-value-added products are appealing because lignin isolation and refining need processing stages that can be combined with structural alterations such as membrane fractionation, derivatization, and others. With more than 50 years of research and significant investments, lignin is the most studied biogenic CF precursor [46]. Lignin-based CF has a potentially significant manufacturing cost advantage over current technologies, with commercial scale prices estimated to be around $4-$6 per pound against $10 per pound for petroleum-based CF (in 2010 dollars) [47]. PAN precursors cost $4-$5 per pound, whereas lignin costs $0.25-$0.70 per pound. Most possible production cost savings can be attributed to this significant reduction in precursor costs. However, possible cost-cutting opportunities in other aspects of the process have been studied as well. Due to performance difficulties and manufacturing limitations, the lignin-to-CF route is not commercially viable [48]. Various entities have been active in lignin-based CF research, but the work undertaken by the Oak Ridge National Laboratory (ORNL) and Innventia, which both manufacture CF for testing reasons, have gotten the most attention in the last ten years [49]. In order to meet goals for finished fiber strength and stiffness, these organizations strive to address commercialization challenges associated with lignin-based CF manufacturing, such as "melt processability (especially for softwood lignins); long heat treatment time (especially for hardwood lignins); variability in the feedstock and unproven scale of operation." These difficulties arise from the heterogeneous molecular weight, functionality, and thermal characteristics of lignin, which vary depending on the source and isolation procedure [50].

Glycerol

With regards to being used in food, cosmetics, and pharmaceuticals, glycerol (also known as glycerine or glycerin) also has the potential to be used as a renewable chemical source. It is doable to be utilized in the production of ACN, which may then be polymerized and spun into PAN, which can then be utilized in a variety of applications CF was converted. The literature describes two glycerol-to-ACN conversion processes: Direct synthesis in the gas or liquid phase employing microwave heating in the latter case and ammoxidation in the former [51]. Indirect synthesis via acrolein—glycerol is dehydrated to generate acrolein, which is then ammoxidized to ACN—or allyl alcohol—glycerol can be converted to allyl alcohol using iron oxide as a catalyst, followed by ammoxidation of allyl alcohol to ACN as intermediates [52]. In the past, synthetic methods were mostly used to produce glycerol from petroleum. Yet, as a byproduct of numerous industrial processes, such as the production of biodiesel, the hydrolysis of fatty acids, and the production of soap, glycerol from plant and animal sources became readily accessible. Biodiesel production now accounts for most of the glycerol production, accounting for around 63 percent of the market in 2013. In 2013, global glycerol consumption was 2.2 million tonnes, with 3.5 million tonnes projected by 2020 [53]. Given the better lifestyle in emerging nations, which leads to higher consumption of processed and packaged goods, this demand is predominantly driven by the food and beverage industry. As a result, rather than producing surplus steam in the mill, removing a portion of the

dissolved wood polymers should be a realistic option that also opens new product areas. Glycerol (also known as glycerine or glycerin) is utilized in cosmetics, pharmaceuticals, and food items, but it also has the potential to be used as a renewable chemical source. It can be used to make ACN, which can be polymerized and spun into PAN, which can then be turned into CF [54].

Lignocellulosic sugars

The use of biomass-derived sugars (e.g., glucose, fructose, and xylose) generated from the cellulose and hemicellulose portions of biomass is another mechanism for producing ACN [55]. Laboratory testing has revealed that this route may be used to directly replace conventional ACN with mechanical qualities that are comparable. Recognizing this prospect, the US Department of Energy approved two projects in 2014 to improve the production of low-cost, high-performance CF using sustainable, non-food-based biomass feedstocks [37]. For the conversion of sugars from non-food biomass to ACN, the Southern Research Institute (SRI) in Birmingham, Alabama, will use a multi-step catalytic process. Multiple metabolic pathways to ACN will be investigated and optimized at the National Renewable Energy Laboratory (NREL) in Golden, Colorado.

Biomass-based goods made from natural resources have recently gotten a lot of interest in academics and industry [56]. Biomass materials, as a vast resource pool, have become a popular area of research, with biomass resources such as agricultural wastes and other renewable resources being used to create biomass-based porous carbon compounds [57]. Porous carbon materials such as rice, fiber, wood, prolifera, cattle bone, coconut shells, silk, egg whites, and cigarettes have all been employed in supercapacitors, lithium batteries, and fuel cells. There are few investigations on activated carbon fibers employing natural plant fibers as raw materials in current research, and industrial production has yet to be established [58]. As a result, using biomass as a raw material to make activated carbon fibers and using them in supercapacitors has more practical value and significance [59]. This is owing to benefits such as sustainability, recyclability, cost, efficacy, environmental friendliness, and so on [60]. Although the fibers are not discontinuous, limited in fiber length, and have relatively low mechanical properties in comparison to conventional rayon-based and PAN-based carbon fibers, it would be desirable and useful if carbon fibers or activated carbon fibers could be made from biomass-based natural fibers, which are abundant in nature and less expansive [61].

3. Carbon fiber from other biogenic sources

Glutamic acid, which may be produced from a variety of waste streams including dry distiller's grains and solubles from the manufacturing of ethanol from corn and wheat, is another biogenic source that has been investigated for the creation of ACN. A palladium catalyst is used in a two-step process that starts with an oxidative decarboxylation of 3-cyanopropanoic acid in water and ends with a decarbonylation-elimination reaction. Another method for producing CF has been suggested: Genetic manipulation of biomass. This route comprises (1) employing CO_2 or carbon nanotubes via yet-to-be-developed technologies and (2) engineering plants to generate lignin or other natural polymers that could be transformed into PAN-like compounds. Additionally, the University of Delaware researchers have looked into the use of chicken feathers as a raw material for the synthesis of CF. They created chicken feather fibers with low modulus and low to medium strength; they want to raise these parameters, but recent years have seen a decline in their research in this area.

4. Advantages of increased sustainability

Utilizing CF made from biomass could give some companies a competitive edge. For instance, many current athletic goods incorporate CF to lighten and strengthen their construction. Many of these producers also emphasize the environmentally friendly qualities of the goods they produce. Some snowboards have certified sustainably obtained wood cores that have a minimal environmental impact.

A common component of snowboards is CF, which enhances performance. For some businesses, being able to sell sustainable CF generated from biomass rather than fossil fuels could have a positive competitive advantage and be a differentiation, potentially making the risk associated with switching materials worth it. Many merchants and producers are making efforts to lessen the environmental impact of the goods they produce or sell. For instance, many merchants put pressure on their suppliers to save costs and environmental impact. Switching materials might be encouraged if CF made from biomass could save costs and have positive environmental effects for a product like a tennis racket. Additionally, many businesses, particularly those in Europe, are facing greater pressure to lessen the environmental impact of the goods they produce. Sustainability professionals, activists, or shareholders may encourage the use of low-impact materials like biomass-based CF.

4.1 Recyclability

The recyclability of CF at the end of its useful life has been identified as a known concern by numerous ongoing research efforts, although few current workable solutions have been offered. Beginning in 2015, each car must include 85% recyclable elements by weight in accordance with the End-of-Life Vehicle (ELV) Directive 5 of the European Union (Gardiner 2014). Metals and other plastics used in automobiles are recyclable, but CF is currently not. CF must be recyclable if it is to become a key automotive component in Europe. Similar problems are faced by the European aircraft sector, and Airbus has set a goal to recycle 95% of its CF-reinforced plastic by the years 2020-2025. Biomass-based CF might become more popular if it offered a better route to recycling. This would provide it with a significant supply chain advantage. However, if CF made from biomass were chemically equivalent to CF made from petroleum, it would have the same problems with recycling and probably not be more advantageous. For a better understanding of the process and possibilities for recycling, more research is needed to examine the recyclability of biomass-based CF.

4.2 Biomass feedstock competition

There are additional existing or potential uses and applications for biomass resources that might be used to make CF. These include the production of heat and electricity, as well as chemicals and other materials from lignocellulosic material. Glycerol is currently primarily used in personal care and pharmaceutical products, as was already mentioned. However, between now and 2020, food and beverage are expected to see the fastest growth in terms of application. This is due to improving lifestyles in emerging economies, which have led to an increase in the consumption of processed and packaged foods. There is ongoing research into the synthesis of liquid fuels, aromatic compounds, and polymers as well as other value-added commodities from lignin. The capacity to secure a supply of raw materials at a reasonable price will be a critical factor for the industry's long-term success. The potential risk to feedstock supply is increased by competition from other sectors for biomass. For instance, CF is just one of 43 possible lignin-derived compounds listed in a paper from the Pacific Northwest National Laboratory. CF is a high-value product and would probably compete advantageously for lignin with many other commodities, but price increases due to the competition may lessen the cost savings from CF made from biomass.

4.3 Plant siting and feedstock logistics

The location of CF manufacturing facilities has been determined by a few variables, such as closeness to customers or affordable energy. Since most of these current facilities are close to biomass sources, there may be a chance to incorporate these alternative sources into the production of CF. With only one or two exceptions, solid biomass resources and pulp and paper mills, which serve as a stand-in for lignin production, are located close to the CF manufacturing factories (e.g., crop residues, forest residues, or both). The economic analysis of biomass-based CF must appropriately account for and take into consideration the logistics of packing and delivering these

raw materials. The bulk of CF manufacturing facilities in the United States already imports raw materials for CF production, such as PAN or ACN, from other nations. These facilities might perhaps switch to importing biomass or precursors generated from biomass, such as ACN or PAN. Some biomass resources can cost up to $100 per dry ton, and in some situations even more, to purchase (for example, lignocellulosic biomass, which includes crop leftovers). In comparison to the current price of ACN, which is about a dollar per pound, even at the high end of expenses, this is only a few cents per pound.

5. Conclusions

As of right now, no biomass-based CF has been created that possesses the structural qualities needed for use in the main CF applications (such as aerospace, wind, and automotive). The appropriate application or exploitation of the many forms of CF that can be produced from biomass sources depends on the physical qualities (mainly tensile strength, as well as other factors). The market share of CF made from rayon is modest. Since the strength of this form of CF is less than that needed for structural purposes, it is generally employed in insulating and ablative applications. CF made from lignin is still in the research and development (R & D) stage. Current research is concentrated on non-structural uses like insulation because based on current experimental efforts, the modulus and strength of lignin-based CF are too low to meet the criteria of structural applications. Although glycerol is cheap and widely available, straight ammoxidation from this resource to produce acrylonitrile (ACN) has been shown to be uneconomical at the current moment; it costs around 67% more than ammoxidation based on propane. Although other conversion routes have been looked into, it is still unclear whether they are cost-effective. In addition to its techno-economic viability, biomass-based CF will have other ramifications and difficulties that must be taken into account for manufacturing, feedstock supply, and end products. They include raw material availability, plant locations, raw material certification, product warranties, product competitiveness, and raw material availability.

Conflict of Interest

There is no conflict of interest.

References

[1] Jiménez, V., Sánchez, P., Romero, A., 2017. Materials for activated carbon fiber synthesis. Activated Carbon Fiber and Textiles. 21-38. DOI: https://doi.org/10.1016/B978-0-08-100660-3.00002-X

[2] Wang, K., Zhang, G., Zhao, P., et al., 2014. Effects of calcination temperature on the structure and CO_2 sorption properties of Li_4SiO_4 sorbents from rice husk ash. 2014 International Conference on Mechatronics, Electronic, Industrial and Control Engineering (MEIC-14). Atlantis Press: The Netherlands. pp. 760-763. DOI: https://doi.org/10.2991/MEIC-14.2014.170

[3] Wang, K., Yan, R., Zhao, N., et al., 2016. Bio-inspired hollow activated carbon microtubes derived from willow catkins for supercapacitors with high volumetric performance. Materials Letters. 174, 249-252. DOI: https://doi.org/10.1016/J.MATLET.2016.03.063

[4] Lei, Z., Zhang, J., Zhang, L.L., et al., 2016. Functionalization of chemically derived graphene for improving its electrocapacitive energy storage properties. Energy & Environmental Science. 9(6), 1891-1930. DOI: https://doi.org/10.1039/C6EE00158K

[5] Huang, X., 2009. Fabrication and properties of carbon fibers. Materials. 2(4), 2369-2403. DOI: https://doi.org/10.3390/MA2042369

[6] Zhang, G., Song, Y., Zhang, H., et al., 2016. Radially aligned porous carbon nanotube arrays on carbon fibers: A hierarchical 3D carbon

nanostructure for high-performance capacitive energy storage. Advanced Functional Materials. 26(18), 3012-3020.
DOI: https://doi.org/10.1002/ADFM.201505226

[7] Liu, F., Wang, H., Xue, L., et al., 2008. Effect of microstructure on the mechanical properties of PAN-based carbon fibers during high-temperature graphitization. Journal of Materials Science. 43, 4316-4322.
DOI: https://doi.org/10.1007/S10853-008-2633-Y

[8] Bhatt, P., Goe, A., 2017. Carbon fibres: Production, properties and potential use. Material Science Research India. 14(1), 52-57.
DOI: https://doi.org/10.13005/MSRI/140109

[9] Deng, Y.L., 2007. Carbon fiber electronic interconnects [PhD thesis]. College Park: University of Maryland, College Park.

[10] All about Carbon Fiber and How It's Made [Internet] [cited 2022 Feb 27]. Available from: https://www.thoughtco.com/how-is-carbon-fiber-made-820391

[11] Lim, T.H., Kim, M.S., Yeo, S.Y., et al., 2019. Preparation and evaluation of isotropic and mesophase pitch-based carbon fibers using the pelletizing and continuous spinning process. Journal of Industrial Textiles. 48(7), 1242-1253.
DOI: https://doi.org/10.1177/1528083718763774

[12] Maciá-Agulló, J.A., Moore, B.C., Cazorla-Amorós, D., et al., 2007. Influence of carbon fibres crystallinities on their chemical activation by KOH and NaOH. Microporous and Mesoporous Materials. 101(3), 397-405.
DOI: https://doi.org/10.1016/J.MICROMESO.2006.12.002

[13] Chatterjee, S., Jones, E.B., Clingenpeel, A.C., et al., 2014. Conversion of lignin precursors to carbon fibers with nanoscale graphitic domains. ACS Sustainable Chemistry & Engineering. 2(8), 2002-2010.
DOI: https://doi.org/10.1021/SC500189P

[14] Frank, E., Steudle, L.M., Ingildeev, D., et al., 2014. Carbon fibers: precursor systems, processing, structure, and properties. Angewandte Chemie International Edition. 53(21), 5262-5298.
DOI: https://doi.org/10.1002/ANIE.201306129

[15] Lewandowska, A.E., Soutis, C., Savage, L., et al., 2015. Carbon fibres with ordered graphitic-like aggregate structures from a regenerated cellulose fibre precursor. Composites Science and Technology. 116, 50-57.
DOI: https://doi.org/10.1016/J.COMPSCITECH.2015.05.009

[16] Ju, A.Q., Guang, S.Y., Xu, H.Y., 2012. A novel poly [acrylonitrile-co-(3-ammoniumcarboxylate-butenoic acid-methylester)] copolymer for carbon fiber precursor. Chinese Chemical Letters. 23(11), 1307-1310.
DOI: https://doi.org/10.1016/J.CCLET.2012.09.021

[17] Bell, J.P., Dumbleton, J.H., 1971. Changes in the structure of wet-spun acrylic fibers during processing. Textile Research Journal. 41(3), 196-203.
DOI: https://doi.org/10.1177/004051757104100302

[18] Fitzer, E.M.D.J., Müller, D.J., 1975. The influence of oxygen on the chemical reactions during stabilization of pan as carbon fiber precursor. Carbon. 13(1), 63-69.
DOI: https://doi.org/10.1016/0008-6223(75)90259-6

[19] Mathur, R.B., Bahl, O.P., Mittal, J., 1992. A new approach to thermal stabilisation of PAN fibres. Carbon. 30(4), 657-663.
DOI: https://doi.org/10.1016/0008-6223(92)90185-Y

[20] Lv, M.Y., Ge, H.Y., Chen, J., 2009. Study on the chemical structure and skin-core structure of polyacrylonitrile-based fibers during stabilization. Journal of Polymer Research. 16, 513-517.
DOI: https://doi.org/10.1007/S10965-008-9254-7

[21] Kim, B.S., Park, J.H., Hong, N., et al., 2013. Ultrathin carbon film from carbonization of spin-cast polyacrylonitrile film. Journal of Industrial and Engineering Chemistry. 19(5), 1631-1637.
DOI: https://doi.org/10.1016/J.JIEC.2013.01.034

[22] Morgan, P., 2005. Carbon fibers and their composites. CRC Press: Boca Raton.
DOI: https://doi.org/10.1201/9781420028744

[23] Park, S.J., Heo, G.Y., 2015. Precursors and manufacturing of carbon fibers. Carbon Fibers. 210, 31-66.
DOI: https://doi.org/10.1007/978-94-017-9478-7_2

[24] Huang, X., 2009. Fabrication and properties of carbon fibers. Materials. 2(4), 2369-2403.
DOI: https://doi.org/10.3390/MA2042369

[25] Park, S.J., Kim, B.J., 2015. Carbon fibers and their composites. Springer: Berlin.

[26] Newcomb, B.A., 2016. Processing, structure, and properties of carbon fibers. Composites Part A: Applied Science and Manufacturing. 91, 262-282.
DOI: https://doi.org/10.1016/J.COMPOSITESA.2016.10.018

[27] Peebles, L.H., 2018. Carbon fibers: Formation, structure, and properties. CRC Press: Boca Raton. pp. 1-203.

[28] Wei, H., Lee, H., Nagatsuka, W., et al., 2015. Systematic comparison between carding and paper-making method for producing discontinuous recycled carbon fiber reinforced thermoplastics. ICCM20; 2005 Jul 21; Copenhagen, Denmark. p. 19-24.

[29] Seydibeyoğlu, M.Ö., 2012. A novel partially biobased PAN-lignin blend as a potential carbon fiber precursor. Journal of Biomedicine and Biotechnology. (Special Issue)
DOI: https://doi.org/10.1155/2012/598324

[30] Carbon Fiber from Biomass [Internet] [cited 2022 Feb 27]. Available from: https://bioplasticsnews.com/2014/02/17/carbon-fiber-from-biomass/

[31] Zhou, X., Wang, P., Zhang, Y., et al., 2016. From waste cotton linter: A renewable environment-friendly biomass based carbon fibers preparation. ACS Sustainable Chemistry & Engineering. 4(10), 5585-5593.
DOI: https://doi.org/10.1021/ACSSUSCHEMENG.6B01408

[32] Wang, J., Nie, P., Ding, B., et al., 2017. Biomass derived carbon for energy storage devices. Journal of Materials Chemistry. 5(6), 2411-2428.
DOI: https://doi.org/10.1039/C6TA08742F

[33] Diefendorf, R.J., Tokarsky, E.J.P.E., 1975. High-performance carbon fibers. Polymer Engineering & Science. 15(3), 150-159.
DOI: https://doi.org/10.1002/PEN.760150306

[34] Milbrandt, A., Booth, S., 2016. Carbon fiber from biomass. United States: N. p.
DOI: https://doi.org/10.2172/1326730

[35] Szabó, L., Imanishi, S., Kawashima, N., et al., 2018. Interphase engineering of a cellulose-based carbon fiber reinforced composite by applying click chemistry. Chemistry Open. 7(9), 720-729.
DOI: https://doi.org/10.1002/OPEN.201800180

[36] Dumanlı, A.G., Windle, A.H., 2012. Carbon fibres from cellulosic precursors: A review. Journal of Materials Science. 47, 4236-4250.
DOI: https://doi.org/10.1007/s10853-011-6081-8

[37] Dahlquist, E. (editor), 2013. Biomass as energy source: Resources, systems and applications. CRC Press: Leiden.

[38] Arantes, A.C.C., Silva, L.E., Wood, D.F., et al., 2019. Bio-based thin films of cellulose nanofibrils and magnetite for potential application in green electronics. Carbohydrate Polymers. 207, 100-107.
DOI: https://doi.org/10.1016/J.CARBPOL.2018.11.081

[39] Klemm, D., Heublein, B., Fink, H.P., et al., 2005. Cellulose: Fascinating biopolymer and sustainable raw material. Angewandte Chemie International Edition. 44(22), 3358-3393.
DOI: https://doi.org/10.1002/ANIE.200460587

[40] Guo, Y., Zhou, J., Song, Y., et al., 2009. An efficient and environmentally friendly method for the synthesis of cellulose carbamate by microwave heating. Macromolecular Rapid Commu-

nications. 30(17), 1504-1508.
DOI: https://doi.org/10.1002/MARC.200900238

[41] Zhou, X., Wang, P., Zhang, Y., et al., 2016. From waste cotton linter: A renewable environment-friendly biomass based carbon fibers preparation. ACS Sustainable Chemistry & Engineering. 4(10), 5585-5593.
DOI: https://doi.org/10.1021/ACSSUSCHEMENG.6B01408

[42] Mainka, H., Täger, O., Körner, E., et al., 2015. Lignin—an alternative precursor for sustainable and cost-effective automotive carbon fiber. Journal of Materials Research and Technology, 4(3), 283-296.
DOI: https://doi.org/10.1016/J.JMRT.2015.03.004

[43] Sun, Q., Khunsupat, R., Akato, K., et al., 2016. A study of poplar organosolv lignin after melt rheology treatment as carbon fiber precursors. Green Chemistry, 18(18), 5015-5024.
DOI: https://doi.org/10.1039/C6GC00977H

[44] Sannigrahi, P., Pu, Y., Ragauskas, A., 2010. Cellulosic biorefineries-unleashing lignin opportunities. Current Opinion in Environmental Sustainability. 2(5-6), 383-393.
DOI: https://doi.org/10.1016/J.COSUST.2010.09.004

[45] Carbon Fiber Made from Lignin (Kayacarbon) [Internet] [cited 2022 Feb 27]. Available from: https://agris.fao.org/agris-search/search.do?recordID=US201301183139

[46] Adam, A.A., Dennis, J.O., Abdulkadir, B.A., et al., 2020. Lignin/Cellulose Nanofibers for Supercapacitor Applications [Internet] [cited 2022 Feb 27]. Available from: https://www.researchgate.net/publication/347913736

[47] Stewart, D., 2008. Lignin as a base material for materials applications: Chemistry, application and economics. Industrial Crops and Products. 27(2), 202-207.
DOI: https://doi.org/10.1016/j.indcrop.2007.07.008

[48] Sabornie, C., Saito, T., 2016. Lignin derived carbon materials. ChemSusChem. 9(24), 3441-3447.

[49] Chatterjee, S., Saito, T., 2015. Lignin-derived advanced carbon materials. ChemSusChem. 8(23), 3941-3958.
DOI: https://doi.org/10.1002/CSSC.201500692

[50] Gabov, K., Fardim, P., da Silva Júnior, F., 2013. Hydrotropic fractionation of birch wood into cellulose and lignin: A new step towards green biorefinery. BioResources. 8(3), 3518-3531.

[51] Calvino-Casilda, V., Olga Guerrero-Pérez, M., Bañares, M.A., 2016. Green chemistry retraction retraction: Efficient microwave-promoted acrylonitrile sustainable synthesis from glycerol. Green Chemistry. 18, 18.
DOI: https://doi.org/10.1039/c6gc90110g

[52] Liu, Y., Tüysüz, H., Jia, C.J., et al., 2010. From glycerol to allyl alcohol: Iron oxide catalyzed dehydration and consecutive hydrogen transfer. Chemical communications. 46(8), 1238-1240.
DOI: https://doi.org/10.1039/b921648k

[53] Anitha, M., Kamarudin, S.K., Kofli, N.T., 2016. The potential of glycerol as a value-added commodity. Chemical Engineering Journal. 295, 119-130.
DOI: https://doi.org/10.1016/J.CEJ.2016.03.012

[54] Mbamalu, V.C., 2013. Glycerin and the market [Master's thesis]. Chattanooga: The University of Tennessee at Chattanooga.

[55] Guerrero-Pérez, M.O., Bañares, M.A., 2015. Metrics of acrylonitrile: From biomass vs. petrochemical route. Catalysis Today. 239, 25-30.
DOI: https://doi.org/10.1016/J.CATTOD.2013.12.046

[56] Inagaki, M., Nishikawa, T., Sakuratani, K., et al., 2004. Carbonization of kenaf to prepare highly-microporous carbons. Carbon. 4(42), 890-893.
DOI: https://doi.org/10.1016/J.CARBON.2004.01.055

[57] Hou, J., Jiang, K., Tahir, M., et al., 2017. Tun-

able porous structure of carbon nanosheets derived from puffed rice for high energy density supercapacitors. Journal of Power Sources. 371, 148-155.
DOI: https://doi.org/10.1016/J.JPOWSOUR.2017.10.045

[58] Gao, X., Xing, W., Zhou, J., et al., 2014. Superior capacitive performance of active carbons derived from Enteromorpha prolifera. Electrochimica Acta. 133, 459-466.
DOI: https://doi.org/10.1016/J.ELECTACTA.2014.04.101

[59] Leitner, K., Lerf, A., Winter, M., et al., 2006. Nomex-derived activated carbon fibers as electrode materials in carbon based supercapacitors. Journal of Power Sources. 153(2), 419-423.
DOI: https://doi.org/10.1016/J.JPOWSOUR.2005.05.078

[60] Ma, X., Yang, H., Yu, L., et al., 2014. Preparation, surface and pore structure of high surface area activated carbon fibers from bamboo by steam activation. Materials. 7(6), 4431-4441.
DOI: https://doi.org/10.3390/MA7064431

[61] Yun, C.H., Park, Y.H., Park, C.R., 2001. Effects of pre-carbonization on porosity development of activated carbons from rice straw. Carbon. 39(4), 559-567.
DOI: https://doi.org/10.1016/S0008-6223(00)00163-9

BILINGUAL PUBLISHING GROUP

Non-Metallic Material Science

https://journals.bilpubgroup.com/index.php/nmms

ARTICLE

Synthesis of Activated Carbon from Polyethylene Terephthalate (PET) Plastic Waste and Its Application for Removal of Organic Dyes from Water

Thu Hanh Thi Pham

Institute of Chemistry and Materials, Nghia Do, Cau Giay, Hanoi, 10000, Vietnam

ABSTRACT

Synthetic plastics are often considered to be materials that cannot be broken down by natural processes. One such plastic, polyethylene terephthalate (PET), is commonly used in everyday items but when these products are discarded, they can cause serious harm to the environment and human health. In this study, PET plastic waste was used to create activated carbon using a physical activation process that involved using CO_2 gas. The researchers investigated the effects of different temperatures, carbonization, and activation times on the resulting activated carbon's surface area. The activated carbon was then analyzed using scanning electron microscopy (SEM), X-ray diffraction (XRD), FTIR, and BET. The activated carbon created from PET plastic waste showed excellent absorption properties for methylene blue in aqueous solutions across a wide range of pH levels. By creating activated carbon from plastic waste, not only are environmental issues addressed, but high-value activated carbon is produced for environmental remediation purposes.

Keywords: Plastic waste; Environmental treatment; Activated carbon; Waste utilization; Polyethylene terephthalate (PET)

1. Introduction

Plastic is widely used in all aspects of daily life and production, such as packaging, household items, construction, transportation, electrical industry, electronics, and other applications. In 2017, over 348 million tons of plastic were produced worldwide, and it is predicted to quadruple by 2050 [1]. Since its introduction into civilian production and application in the 1950s, approximately 6.3 billion tons

*CORRESPONDING AUTHOR:
Thu Hanh Thi Pham, Institute of Chemistry and Materials, Nghia Do, Cau Giay, Hanoi, 10000, Vietnam; Email: masterist83@gmail.com

ARTICLE INFO
Received: 18 April 2023 | Revised: 26 April 2023 | Accepted: 27 April 2023 | Published Online: 12 May 2023
DOI: https://doi.org/10.30564/nmms.v5i1.5663

CITATION
Pham, T.H.T., 2023. Synthesis of Activated Carbon from Polyethylene Terephthalate (PET) Plastic Waste and Its Application for Removal of Organic Dyes from Water. Non-Metallic Material Science. 5(1): 27-37. DOI: https://doi.org/10.30564/nmms.v5i1.5663

of plastic have been discarded, of which about 79% were buried and disposed of in the environment [2]. Plastic waste is very difficult to decompose in the natural environment. Each type of plastic has a different number of years to decompose, with a very long time, hundreds of years, and sometimes even thousands of years. Plastic waste has caused many negative impacts on the ecological environment and human health, therefore finding a solution to plastic waste disposal is one of the most urgent issues.

Currently, most commercial plastic recycling plants mainly use mechanical processing and recycling methods. In Europe, over 5 million tons of plastic waste are recycled by mechanical methods, while only about 50,000 tons are processed and recycled by chemical methods [3]. Mechanical processing methods are often complex and require separate waste collection lines, leading to relatively high costs. In addition, chemical recycling and processing technologies are considered to be economically viable and capable of achieving complete recycling. Many scientists around the world have recently focused on developing technology to recycle plastic waste into carbon-based materials such as graphene, carbon nanotubes, and especially activated carbon [4-9]. Physical activation is a widely used technology for recycling plastic waste into activated carbon [10-13]. Qiao's group used hot steam to activate PVC in the production of activated carbon [4]. PET plastic waste is also commonly used as raw material for the production of activated carbon [7,14-17]. First, PET is carbonized at a temperature of 700 °C in a nitrogen gas environment with a carbon yield of about 20% [5]. The physical activation method also uses CO_2 to activate carbon from PET plastic. Almazán-Almazán and colleagues have successfully changed the structure of activated carbon by controlling some process conditions to obtain activated carbon with high surface area, porous structure, and high adsorption volume [6]. However, it can be seen that when implementing the physical activation method, the production conditions such as long time, high carbonization and activation temperatures are difficult and energy-consuming [16,18].

This article presents a study on the production of activated carbon from PET waste using physical activation method with CO_2 gas to find the optimal time and temperature. At the same time, it presents some results of the application of the obtained activated carbon in the adsorption and treatment of methylene blue dye in water.

2. Experimental section

2.1 Materials

Waste PET plastic is collected in the form of plastic bottles. The plastic bottles are then cut into small pieces of 1-3 mm, washed and dried. Crystalline iodine, $Na_2S_2O_3 \cdot 5H_2O$, starch, CO_2 gas, and methylene blue were purchased from Xilong Company, China.

2.2 Activated carbon fabrication

Carbonization: Weigh the appropriate amount of PET plastic and put it into a ceramic boat, then place the ceramic boat into the tube furnace. Throughout the heating process, the environment inside the tube furnace is a continuously blowing CO_2 gas environment. The carbonization phase is carried out within a certain period of time and at a specific temperature. After the heating process is complete, the resulting carbonized product is cooled down [7,15].

Yield of carbonization process:

$$H = \frac{m_{carbon}}{m_{plastic}} \times 100\%$$

Carbon activating process: The activated carbon product is baked in a tube furnace (with a CO_2 gas environment) for a specified time and temperature [7,15]. After the activation time, the product is cooled. Then, the activated carbon is further crushed into a fine powder. The activated carbon samples in the form of a fine powder are tested for their iodine number, and the optimized sample is selected for structural analysis and surface area measurement.

Yield of activating process:

$$H = \frac{m_{activated\ carbon}}{m_{carbon}} \times 100\%$$

The physical activation process is carried out by using CO_2 gas, which will act as an activating gas. CO_2 will react with the carbon in the material to create pores that increase the specific surface area and also prevent the infiltration of oxygen gas (O_2) [16].

$$C + CO_2 \longrightarrow 2CO \qquad \Delta H = +159 \text{ kJ/mol}$$

2.3 Materials characterizations

The morphological surface structure characteristics of the activated carbon were observed using a scanning electron microscope (SEM) from HITACHI S-4800 (Japan). The functional groups on the surface of the activated carbon were investigated using Fourier-transform infrared spectroscopy (FTIR) from Perkin Elmer, model Spectrum Two (UK). X-ray diffraction (XRD) measurements were carried out using a machine from X'Pert PRO Panalytical PW3040/60 (Netherlands) with Cu-Kα 0.15405 nm radiation source to study the crystallinity of the samples. The physisorption-desorption method of nitrogen was used with a Tristar 3000-Micromeritics machine to determine the BET surface area of the activated carbon samples.

2.4 Methylene blue (MB) adsorption behaviour of prepared activated carbon

Influence of solution pH: 10 mg of activated carbon was added to 10 mL of 10 ppm MB solution with varying pH values, and the adsorption time was 20 minutes.

Influence of activated carbon dosage: 10 mg, 20 mg, 30 mg, 40 mg, and 50 mg of activated carbon were added to 10 mL of 10 ppm MB solution at pH 7, and the adsorption time was 20 minutes.

Influence of adsorption time: 10 mg of activated carbon was added to 10 mL of 10 ppm MB solution at pH 7 for different periods of time: 15 minutes, 20 minutes, 25 minutes, 30 minutes, 35 minutes, and 40 minutes.

Influence of MB solution concentration: 10 mg of activated carbon was added to MB solution with varying concentrations at pH 7 for 35 minutes.

The adsorption samples were stirred on a stirrer. After stirring, the solid was filtered out, and the resulting solution was measured for absorbance using a UV-VIS machine.

From these results, the adsorption efficiency of the activated carbon was calculated using the formula:

$$H = \frac{C_o - C}{C_o} \times 100\%$$

where: Co, C are the initial and after-adsorption concentrations of MB (ppm); H: Yield (%).

3. Results and discussion

The effect of temperature and time on the carbonization stage

Table 1 is the results of the effect of temperature and time on the carbonization stage. The investigation of the heating temperature from 400 °C to 600 °C for a duration of 15 minutes shows a gradual decrease in efficiency, and a sudden drop in efficiency is observed at 600 °C. This can be explained by the fact that before 600 °C, volatile substances and water vapor were easily released from the material, and at 600 °C, the formation of pores began to develop the porous structure of the activated carbon, resulting in a significant change in mass. Therefore, the temperature of 550 °C was chosen as the temperature for the carbonization process.

Table 1. Effect of temperature on the carbonization yield.

Samples	Temperature (^{o}C)	Time (minutes)	yield (%)
4015	400	15	13.98
4515	450	15	13.67
5015	500	15	13.69
5515	550	15	13.45
6015	600	15	12.5

The effect of carbonization time on the conversion yield was also studied and the result is shown in **Table 2**. A study of the carbonization time at 550 °C from 15 to 30 minutes showed that as the time increased, the carbonization efficiency decreased gradually. This can be explained by the fact that as the time increases, the decomposition of the structure and the volatilization of the substances become

greater. However, at 550 °C, the efficiency of the process did not change significantly, so the choice of the carbonization time period is 15 minutes.

Table 2. Effect of carbonization time on the conversion yield.

Samples	Temperature (^{0}C)	Time (minutes)	Yield (%)
5515	550	15	13.45
5520	550	20	13.28
5525	550	25	13.1
5530	550	30	12.97

The effect of temperature and time on the activating stage

From **Table 3** and **Figure 1**, it can be seen that from the temperature range of 600 °C to 800 °C, both the efficiency and iodine number do not change significantly. However, when the temperature reaches 850 °C, the iodine number increases significantly. This can be explained by the fact that at 850 °C, the pore structure is completed and the ability to adsorb iodine reaches the highest efficiency. At 900 °C, the efficiency and iodine number decrease abruptly, indicating that the process has entered the carbonization stage, and the pore structure is destroyed, directly affecting the quality of the resulting activated carbon. Therefore, 850 °C is chosen as the suitable temperature for the activation process.

Based on the results obtained in **Table 4** and **Figure 2**, it can be seen that there is no significant change in performance during the 25-minute activation time compared to the 20-minute time, and the iodine number reaches its highest value. The iodine number and performance decrease at 30 minutes, indicating that the formed pore system has been carbonized, resulting in a decrease in specific surface area. Therefore, 25 minutes is the appropriate activation time.

Table 3. Effect of temperature on the activating stage.

Samples	Carbonization temperature (^{0}C)/ time (minutes)	Activating temperature (^{0}C)	Activating time (minutes)	Yield (%)
AC6020	550/15	600	20	11.31
AC6520	550/15	650	20	11.30
AC7020	550/15	700	20	11.21
AC7520	550/15	750	20	9.79
AC8020	550/15	800	20	9.5
AC8520	550/15	850	20	8.69
AC9020	550/15	900	20	8.09

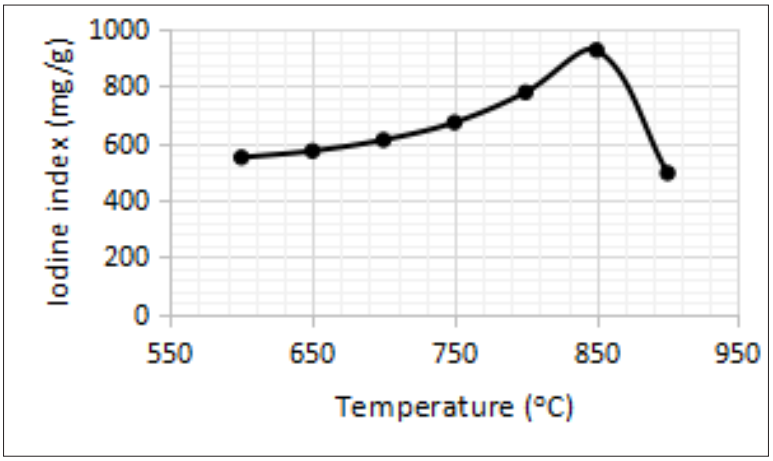

Figure 1. Effect of the activating temperature on the iodine adsorption.

Table 4. Effect of time on the activating stage.

Sample	Temperature (°C)	Time (minutes)	Yield (%)	Iodine index (mg/g)
AC8520	850	20	8.69	927.1
AC8525	850	25	8.57	1003.3
AC8535	850	30	8.02	749.3

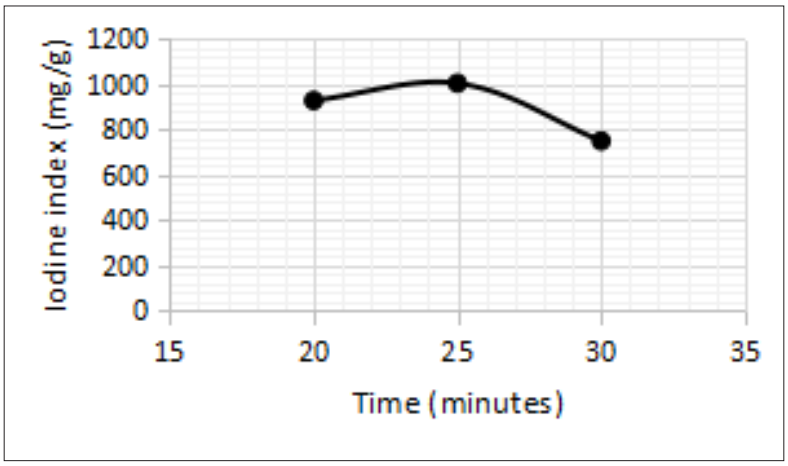

Figure 2. Effect of the activating temperature on the iodine adsorption.

3.1 Characterizations of the activated carbon fabricated using optimized conditions

From **Figure 3**, it can be seen that the X-ray diffraction pattern of the prepared activated carbon sample. The increase in peak intensity in the range of 10-30 degrees is due to the presence of continuous pore voids that scatter X-ray radiation [18]. Subsequently, the XRD peaks weaken, indicating that the activated carbon is in the form of graphite and has many defects on the surface, resulting in a decrease in graphitic crystallization of the activated carbon (JCPSD no. 00-056-0160). Therefore, in the activation process, it is desirable to create more defects on the surface of the carbon to increase the surface area of the activated carbon.

The surface chemical characteristics of the activated carbon are demonstrated through the FTIR spectrum as shown in **Figure 4**. A series of characteristic peaks shown in the graph indicate the presence of various chemical functional groups. The peak at 3447.77 cm^{-1} indicates the -OH group on the surface structure of the activated carbon [14]. The peaks at around 2923.56 and 2871.39 cm^{-1} indicate the appearance of C-H bonds in the benzene and alkane rings. The peak at around 1600 cm^{-1} is characteristic of C-C bonds, while the peak at around 1300 cm^{-1} is characteristic of C-O bonds. The presence of -OH groups may be due to the adsorption of moisture on the activated carbon surface under normal storage conditions, while the presence of C-O groups is likely due to the reaction between C and CO_2, creating a porous structure with the appearance of C-O bonds. The results indicate that the activated carbon obtained is suitable for adsorbing organic compounds, including organic dyes.

The surface morphology of the activated carbon made from PET waste plastic is shown in the SEM image (**Figure 5**). It can be seen that the surface of the activated carbon is relatively smooth, with no clear presence of pores, voids, or channels on the surface.

The surface area is one of the important factors directly affecting the adsorption capacity of activated carbon. The principle is the equal heat of adsorption of nitrogen used to determine the volume of a monolayer. Knowing the covering area of N_2 in the adsorbed state, the specific surface area of the adsorbent can be calculated [19]. **Figure 6** shows the nitro-

gen adsorption isotherm of activated carbon derived from PET waste was measured at 77.3 K. The BET surface area measurement results showed that the activated carbon sample carbonized at 550 °C for 15 minutes and activated at 850 °C for 25 minutes had a specific surface area of 703.4 m^2/g.

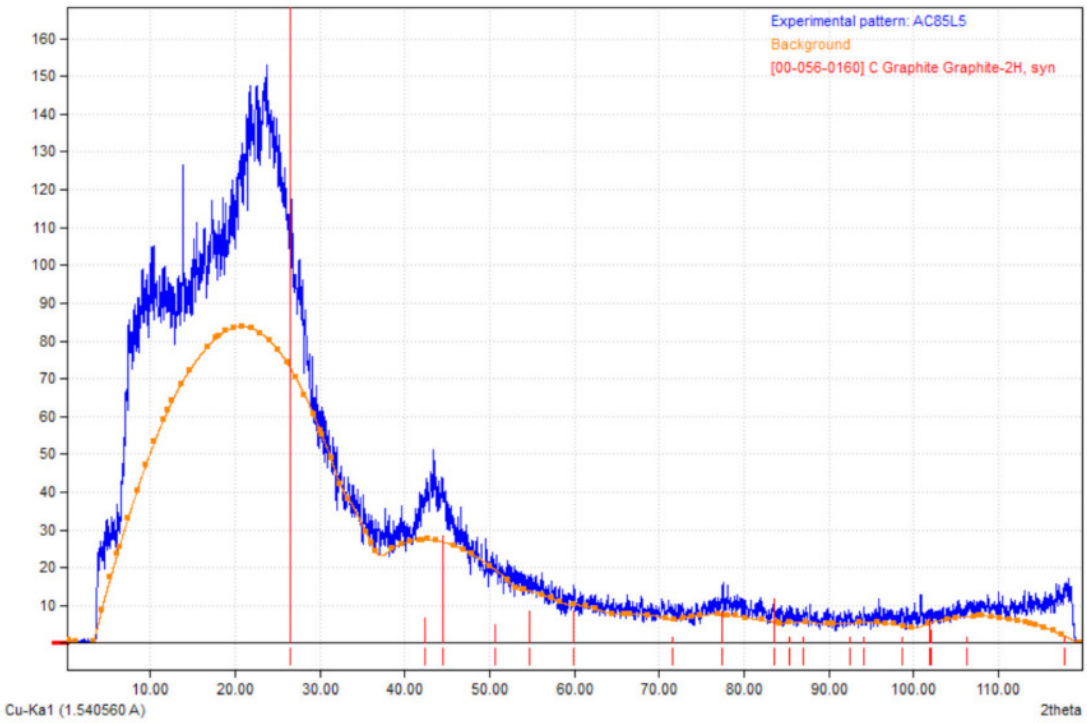

Figure 3. XRD pattern of the activated carbon fabricated from PET plastic using physical activation route at temperature 850 °C for 20 minutes.

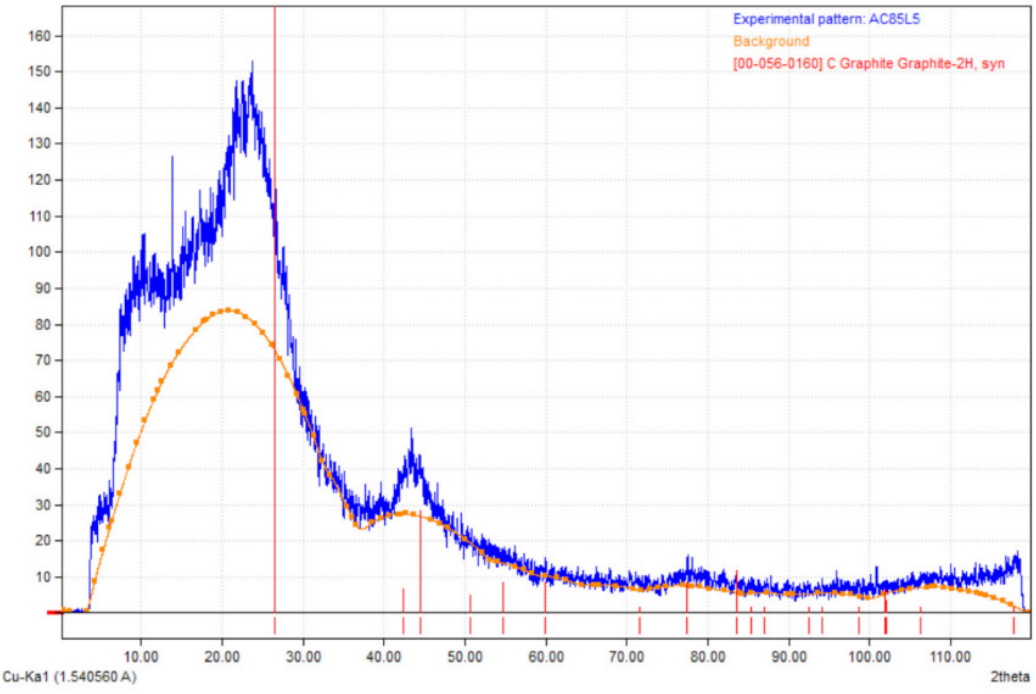

Figure 3. XRD pattern of the activated carbon fabricated from PET plastic using physical activation route at temperature 850 °C for 20 minutes.

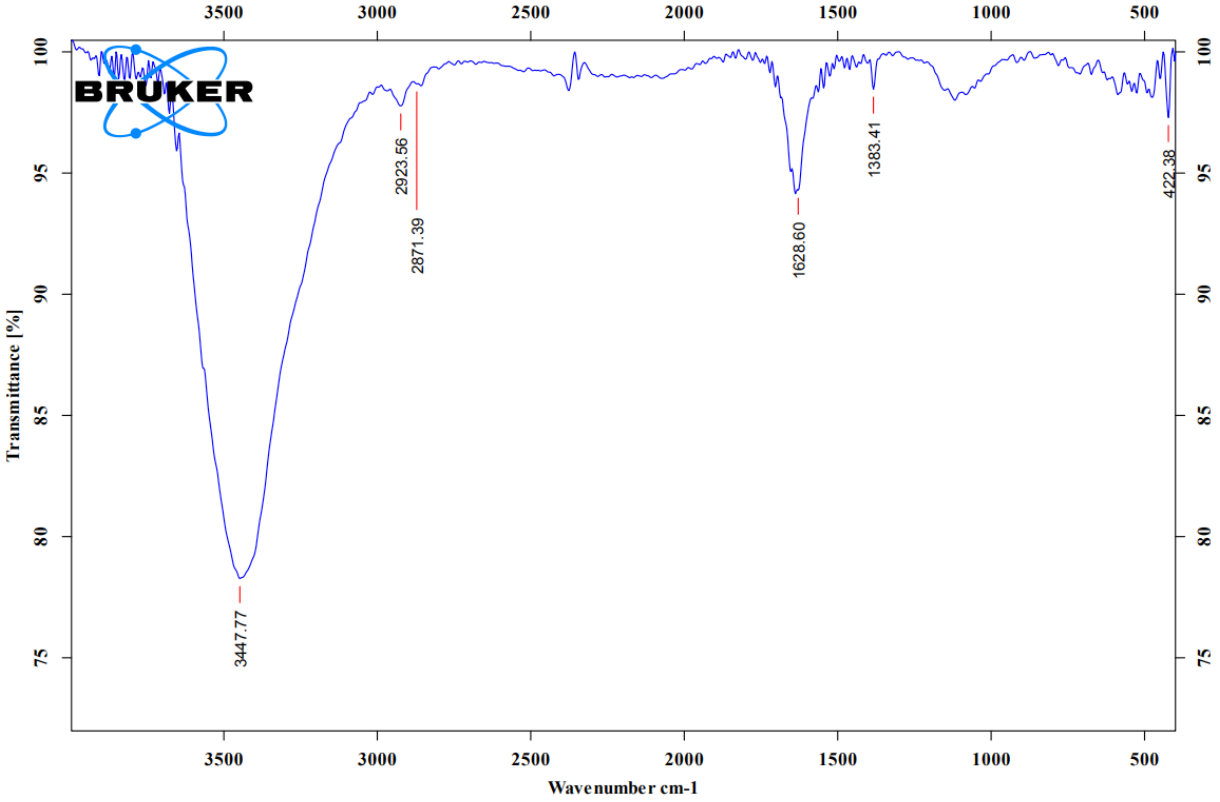

Figure 4. FTIR spectrum of the activated carbon fabricated from PET plastic using physical activation route at temperature 850 °C for 20 minutes.

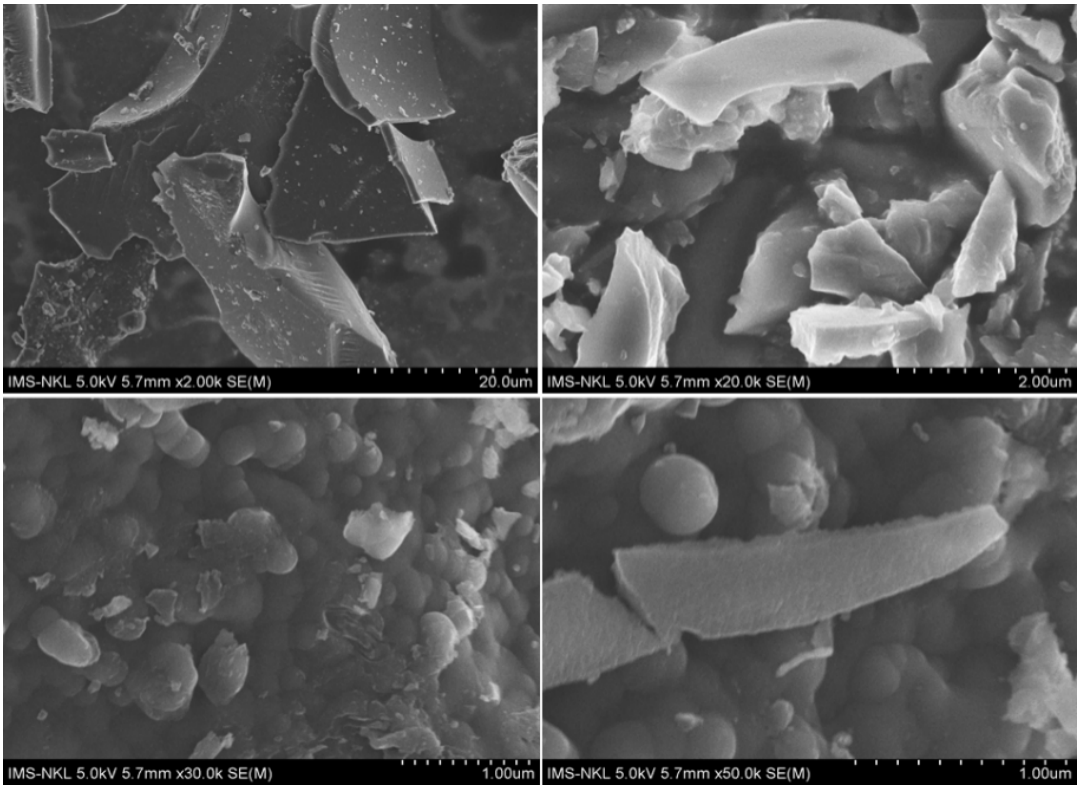

Figure 5. SEM images of the activated carbon fabricated from PET plastic using physical activation route at temperature 850 °C for 20 minutes.

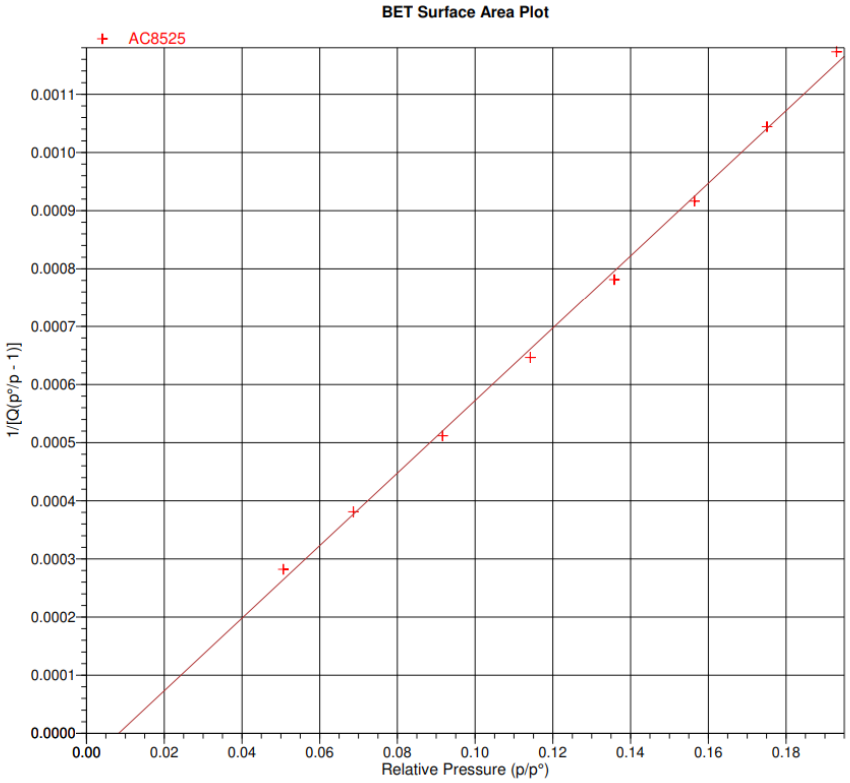

Figure 6. The nitrogen adsorption isotherm of activated carbon derived from PET waste was measured at 77.3 K.

3.2 MB adsorption behaviour of prepared activated carbon

Effect of pH on the MB adsorption efficiency

From **Figure 7**, it can be seen that when pH < 7 (acidic environment), the MB adsorption efficiency of the activated carbon is only below 50%, but when pH ≥ 7, the adsorption efficiency reaches over 80%. The investigation shows that the activated carbon adsorbs well in a pH ≥ 7 environment. Therefore, the next processes will be carried out in a neutral environment, which is suitable for practical conditions in dyeing wastewater treatment.

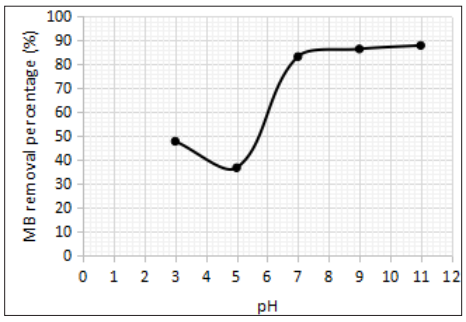

Figure 7. Effect of pH on the MB adsorption efficiency.

Effect of amount of activated carbon on the MB adsorption efficiency

From the survey results, we can see that the higher the mass of activated carbon, the higher the adsorption efficiency. **Figure 8** reveals the effect of the amount of activated carbon on the MB adsorption efficiency. Specifically, with a mass of 0.01 g of carbon, the adsorption efficiency is only 83.212%, while increasing the mass of carbon to 0.02 g results in an efficiency of 94% and there is not much change when increasing the mass of carbon further. Therefore, a mass of 0.02 g of carbon is a suitable condition for weighing and investigating further adsorption processes.

Effect of time on the MB adsorption efficiency

The effect of time on the MB adsorption efficiency was also studied as shown in **Figure 9**. From the obtained results, we can see that the adsorption efficiency is proportional to the adsorption time. The longer the adsorption time, the higher the efficiency and it gradually stabilizes. Specifically, during the adsorption time from 15 to 35 minutes, the efficiency

gradually increases from 87.115% to 95.033%, and at 40 minutes, the adsorption efficiency stabilizes at 95.033%. Therefore, at the time of 35 minutes, the adsorption process reaches equilibrium.

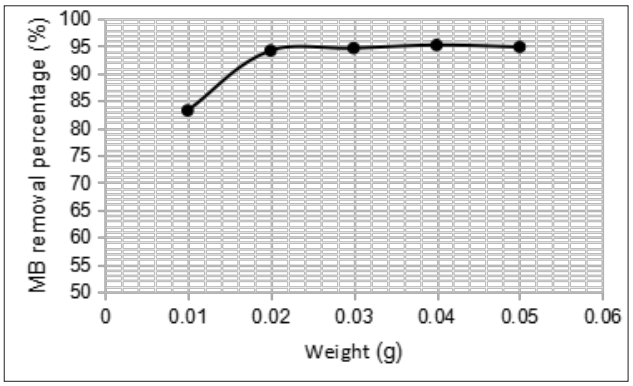

Figure 8. Effect of amount of activated carbon on the MB adsorption efficiency.

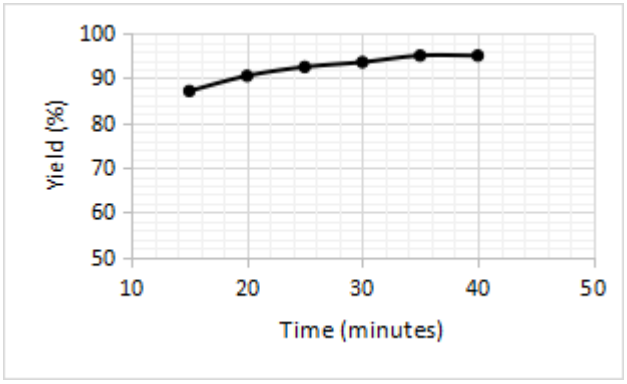

Figure 9. Effect of time on the MB adsorption efficiency.

Effect of MB concentration on the MB adsorption efficiency

Illustrated in **Figure 10** is the effect of MB concentration on the MB adsorption efficiency. The experimental results show that under the same conditions, the adsorption capacity decreases as the MB concentration increases. When increasing the concentration of the solution from 10 ppm to 20 ppm, the efficiency decreases insignificantly (about 4%). However, when the concentration reaches 30%, the color adsorption efficiency drops to 81.34%, and when the concentration reaches 40%, the adsorption efficiency is only 61.18%.

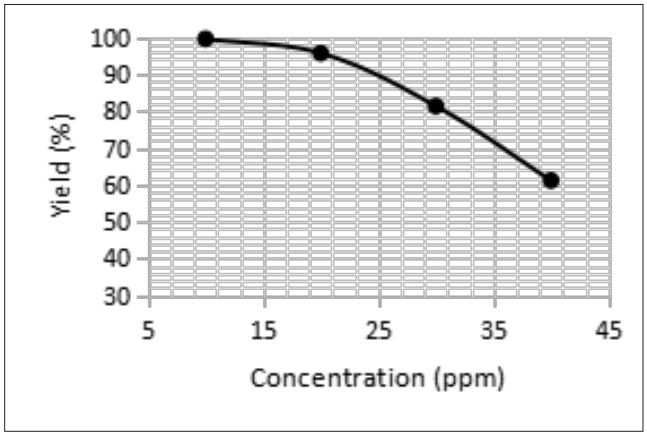

Figure 10. Effect of MB concentration on the MB adsorption efficiency.

4. Conclusions

The successful synthesis of activated carbon materials from PET waste using a physical activation method provides an eco-friendly solution to manage PET waste while producing valuable material for various applications. The specific surface area of 703.4 m^2/g suggests that the activated carbon has a high adsorption capacity for various pollutants. The good adsorption capacity of the PET waste-derived activated carbon for MB in a pH $\geq$ 7 environment indicates its potential as an adsorbent for wastewater treatment. The Langmuir isotherm model provides a good fit for the MB adsorption process, and the maximum adsorption capacity of 18.284 mg/g suggests that the PET waste-derived activated carbon is an efficient adsorbent for MB removal. Overall, this study demonstrates the potential of PET waste-derived activated carbon as a sustainable and effective adsorbent for environmental applications.

Author Contribution

Thu Hanh Pham Thi is responsible for all works that have been done for this work, including conceptualization, experiments, analysis, characterization, manuscript preparation, and submission.

Conflict of Interest

There is no conflict of interest.

Acknowledgement

This work was financially funded by The Ministry of Natural Resources and Environment (No. TNMT.2022.05.04).

References

[1] Qureshi, M.S., Oasmaa, A., Pihkola, H., et al., 2020. Pyrolysis of plastic waste: Opportunities and challenges. Journal of Analytical and Applied Pyrolysis. 152, 104804.
DOI: https://doi.org/10.1016/j.jaap.2020.104804

[2] Geyer, R., Jambeck, J.R., Lavender, K., 2017. Law production, use, and fate of all plastics ever made. Science Advances. 3, e1700782.
DOI: https://doi.org/10.1126/sciadv.1700782

[3] d'Ambrières, W., 2019. Plastics recycling worldwide: Current overview and desirable changes. Field Actions Science Reports. The Journal of Field Actions. Special Issue 19, 12-21.

[4] Qiao, W.M., Yoon, S.H., Korai, Y., et al., 2004. Preparation of activated carbon fibers from polyvinyl chloride. Carbon. 42(7), 1327-1331.
DOI: https://doi.org/10.1016/j.carbon.2004.01.035

[5] Bóta, A., László, K., Nagy, L.G., et al., 1997. Comparative study of active carbons from different precursors. Langmuir. 13(24), 6502-6509.
DOI: https://doi.org/10.1021/la9700883

[6] Almazán-Almazán, M.C., Pérez-Mendoza, M., Domingo-García, M., et al., 2010. The influence of the process conditions on the characteristics of activated carbons obtained from PET de-polymerisation. Fuel Processing Technology. 91(2), 236-242.
DOI: https://doi.org/10.1016/j.fuproc.2009.10.003

[7] Esfandiari, A., Kaghazchi, T., Soleimani, M., 2012. Preparation and evaluation of activated carbons obtained by physical activation of polyethyleneterephthalate (PET) wastes. Journal of the Taiwan Institute of Chemical Engineers. 43(4), 631-637.
DOI: https://doi.org/10.1016/j.jtice.2012.02.002

[8] Parra, J.B., Ania, C.O., Arenillas, A., et al., 2002. Textural characterisation of activated carbons obtained from poly (ethylene terephthalate) by carbon dioxide activation. Studies in Surface Science and Catalysis. 144, 537-543.
DOI: https://doi.org/10.1016/S0167-2991(02)80178-1

[9] Bazargan, A., Hui, C.W., McKay, G., 2015. Porous carbons from plastic waste. Porous carbons—hyperbranched polymers—polymer solvation. Springer: Berlin. pp. 1-25.
DOI: https://doi.org/10.1007/12_2013_253

[10] Almazan-Almazan, M.C., Paredes, J.I., Perez-Mendoza, M., et al., 2006. Surface characteristics of activated carbons obtained by pyrolysis of plasma pretreated PET. The Journal of Physical Chemistry B. 110(23), 11327-11333.
DOI: https://doi.org/10.1021/jp056946i

[11] Cho, M.H., Jung, S.H., Kim, J.S., 2010. Pyrolysis of mixed plastic wastes for the recovery of benzene, toluene, and xylene (BTX) aromatics in a fluidized bed and chlorine removal by applying various additives. Energy Fuels. 24(2), 1389-1395.
DOI: https://doi.org/10.1021/ef901127v

[12] Zhou, J., Luo, A., Zhao, Y., 2018. Preparation and characterisation of activated carbon from waste tea by physical activation using steam. Journal of the Air & Waste Management Association. 68(12), 1269-1277.
DOI: https://doi.org/10.1080/10962247.2018.1460282

[13] Zhang, Z.A., Cui, M., Lai, Y.Q., et al., 2009. Preparation and electrochemical characterization of activated carbons by chemical-physical activation. Journal of Central South University of Technology. 16(1), 91-95.
DOI: https://doi.org/10.1007/s11771-009-0015-5

[14] Cuerda-Correa, E.M., Alexandre-Franco, M.F., Fernßndez-Gonzßlez, C., et al., 2016. Preparation of high-quality activated carbon from polyethyleneterephthalate (PET) bottle waste. Its use in the removal of pollutants in aqueous solution.

Journal of Environmental Management. 181, 522-535.
DOI: https://doi.org/10.1016/j.jenvman.2016.06.070

[15] Ali, E., Tahereh, K., Mansooreh, S., 2011. Preparation of high surface area activated carbon from polyethylene terephthalate (PET) waste by physical activation. Research Journal of Chemistry and Environment. 15, 433-437.

[16] Sanal, A., Bernama, A., Haris, F., et al., 2017. Preparation of activated carbon from waste plastics polyethylene terephthalate as adsorbent in natural gas storage. IOP Conference Series: Materials Science and Engineering. 176(1), 012055.
DOI: http://doi.org/10.1088/1757-899X/176/1/012055

[17] Domingo-García, M., Fernández, J.A., Almazán-Almazán, M.C., et al., 2010. Poly (ethylene terephthalate)-based carbons as electrode material in supercapacitors. Journal of Power Sources. 195(12), 3810-3813.
DOI: https://doi.org/10.1016/j.jpowsour.2009.12.090

[18] Bratek, W., Świątkowski, A., Pakuła, M., et al., 2013. Characteristics of activated carbon prepared from waste PET by carbon dioxide activation. Journal of Analytical and Applied Pyrolysis. 100, 192-198.
DOI: https://doi.org/10.1016/j.jaap.2012.12.021

[19] Mai Thanh Phong, M.X.K., Tuấn, P.A., 2020. Than hoạt tính và ứng dụng (Vietnamese) [Activated carbon and its applications]. NXB Khoa học kĩ thuật: Vietnam. Available from: https://e3audiomiennam.com/than-hoat-tinh-va-ung-dung-111192737.html

BILINGUAL PUBLISHING GROUP

Non-Metallic Material Science

https://journals.bilpubgroup.com/index.php/nmms

ARTICLE

Reflection Loss is a Parameter for Film, not Material

***Ying Liu*[1*], *Xiangbin Yin*[1], *Michael G. B. Drew*[2], *Yue Liu*[1]**

[1] *College of Chemistry and Chemical Engineering, Shenyang Normal University, Shenyang, 110034, China*

[2] *School of Chemistry, The University of Reading, Whiteknights, Reading, RG66AD, UK*

ABSTRACT

In studies of microwave absorption in the current literature, theories such as reflection loss, impedance matching, the delta function, and the quarter-wavelength model have been inappropriately applied. As shown in this case study, these problems need to be corrected as they are representative of similar work in the literature.

Keywords: Microwave absorption; Reflection loss; Impedance matching; Input impedance

1. Introduction

Analyses of experimental data which are based on flawed theories should always be corrected [1-3]. Here we highlight inadequacies in the theory that has been applied to experimental data concerned with microwave absorption in some recent papers [4-9] and provide detailed corrections that can be used to correctly understand such experimental data. While some authors are aware of our comments, they continued to use the current theory [8-14] despite our views being available in publications [15-24]. The problems addressed here are common in publications [25-28] and thus deserve serious attention. A theory can survive for several years after it has been proved wrong [29]. The purpose of this work is to draw attention to the subject and to shorten the period for the practice of the wrong theory. Nevertheless, journals are places where different ideas confront each other to push science forward.

2. Reflection loss should not be used to characterize material

The purpose of the paper by Du et al. [4] was to establish the amount of Mo_2C that would provide the best microwave absorption material based on Mo_2C/Co/C composite. However, this was done by using reflection loss *RL*, a parameter for film rather

*CORRESPONDING AUTHOR:

Ying Liu, College of Chemistry and Chemical Engineering, Shenyang Normal University, Shenyang, 110034, China; Email: yingliusd@163.com

ARTICLE INFO

Received: 27 March 2023 | Revised: 25 April 2023 | Accepted: 27 April 2023 | Published Online: 18 May 2023

DOI: https://doi.org/10.30564/nmms.v5i1.5602

CITATION

Liu, Y., Yin, X.B., Drew, M.G.B., et al., 2023. Reflection Loss is a Parameter for Film, not Material. Non-Metallic Material Science. 5(1): 38-48. DOI: https://doi.org/10.30564/nmms.v5i1.5602

than for material [15,18,20,24,30] thus following the common practice in modern research to characterize material [5,6,8-14,31-41].

The property of material should be characterized quantitatively using parameters such as permittivity or permeability while a portion of material can be characterized by extensive variables such as *RL*/dB. Layered material is an assembly of material and two parallel interfaces thus it behaves more like a film than a material [20,24].

RL is the scattering parameter s_{11} for metal-backed film defined in transmission-line theory and therefore, it is a parameter to characterize devices other than material [15,17-23]. Thus, using *RL* to characterize material is inappropriate and the conclusions obtained are misleading. For example, the MCC-50 sample was judged by *RL*/dB and impedance matching (im) theory to be the best microwave absorption composite [4]. MCC-50 and MCC-75 are materials for which *RL* is not applicable. However, it is clear from the data presented in the paper that when correctly interpreted from the properties of the relevant materials, the best microwave absorption composite is in fact MCC-75, a result that can be readily obtained from the innate properties of the materials [4]. Here parameters such as the imaginary part of the permittivity of the material should be used rather than *RL*/dB to characterize dielectric loss material [30] of the Mo_2C which dominated the functionality of the composites. Clearly, judging from the suitable parameters, MCC-50 can be the most suitable composite for microwave absorption film in order to obtain a result for specific applications at some specific frequency and film thickness *d*, but in general, it cannot be considered to be the best absorbing material.

In this context, the absorption mechanism for the device and material must be differentiated [22]. The film of the ternary Mo_2C/Co/C composite is a simple device. The material should be characterized by its innate properties such as permittivity ε_r and permeability μ_r [30]. But as the value of *RL* varies with film thickness *d* while keeping the material of the film unchanged [15,30], it cannot be used to characterize material. This is true since *RL* of film is correlated to R_M of interface [16,22]. R_M is used in Equation (1) for reflection coefficient of interface. Indeed, the ε_r and μ_r values of a material can be obtained from s_{11} and s_{21} of the film [22]. But using s_{11} and s_{21} to obtain ε_r and μ_r and to characterize material are not the same. For example, the equilibrium constant *K* is the innate property of the chemical equilibrium system. Although the equilibrium concentration C_i for species i in a particular equilibrium system can be calculated by using *K*, it cannot be used to characterize thermodynamic equilibrium since it varies when equilibrium is shifted. Similarly, ε_r and μ_r are constants for material but *RL* is not. When the thickness of the film *d* is changed, the values of *RL* change but those of ε_r and μ_r do not. The absorption mechanism of film is related to angular and amplitude effects unique to film [22]. Interestedly, it was proved theoretically [42] that ε_r is a function of *d* and this result was even established using experimental data [42], a result which seems inconsistent and shows that the theoretical proof presented in that paper was wrong [23,42].

Many experimentalists do not pay sufficient attention to theoretical results, so this work, which resolves problems easily overlooked from experimental data, based on theory from mathematical methods [15,17-24] is particularly pertinent. Using the wave cancellation method for microwave absorption film [20,22], the experimental data from voltage measurements for a whole frequency range can be reproduced from transmission-line theory using only constants appropriate to material [17,18,20,22,30]. This shows that the theoretical method of characterization of microwave absorption of film by *RL*/dB from ε_r and μ_r is feasible, i.e., *RL*/dB is obtained from voltage measurement experimentally with Equation (2) [17,22], but its values can also be obtained from *d*, ε_r and μ_r theoretically as shown by Equation (5) below [19-22]. The experimental results obtained from a linear device using different amount of incident microwaves can be accurately predicted by a theoretical model using a matrix of scattering s parameters arising from the innate properties of the device, and the theoretical results can be verified by experimental measurements [17,18,20]. These facts show that experimental

results of film can be well assimilated by universally valid theory.

The results [4] are unexpected, as normally, the real part of permeability μ_r' should have lower values at low frequency and higher values at high frequency [30] rather than the contrary and in particular the values shown at high frequency range do not conform to the fact that Co is the main magnetic component. It is argued that energy can be generated by making the imaginary part of permeability μ_r'' negative. ("This induced electric field can generate an internal magnetic field and radiate some magnetic energy in turn. The radiation of magnetic energy will result in negative μ_r'' values. … Herein, these ternary composites have larger conductivities and smaller magnetic loss capabilities than binary Co/C composite, so that their inherent magnetic loss cannot offset the radiation of magnetic energy completely in high frequency range. " [4]) This explanation is unlikely to be true since it would be an effect symptomatic of a perpetual machine. In fact, the magnetic loss is determined by the absolute value of μ_r'' [21,43]. Thus, the absolute values should be used in that paper [4] for μ_r'' and the magnetic loss tangent, respectively. Contrary to the authors' conclusions [4], MCC-75 is the most efficient magnetic loss composite at high frequency. The material consumes energy if $\mu_r'' > 0$ while no energy will be consumed if $\mu_r'' = 0$. Thus, the authors assume that the composites generate energy when $\mu_r'' < 0$ and as a consequence it was concluded that MCC-75 is the least microwave consumption composite on the grounds that the most energy generating material is the one with the least energy consumption. Thus, the material can output useful work at high frequency without absorbing energy by making μ_r'' negative. Then switching to low frequency to restore the value of μ_r'' to 0 will not require any energy. In those circumstances, a perpetual machine against the laws of thermodynamics would be possible by a circulation of switching frequencies.

2.1 Input and the characteristic impedances

Z_0 was defined as the impedance of free space [5,44-46]. However, free space acts as part of the transmission line and the definition does not distinguish between input and characteristic impedances. Confusion between these two types has led to the imperfect theory of im for interface and for film [17,19] as with the statements: (a) "Ma et al. ever proposed a delta function to evaluate the matching degree of characteristic impedance between free space and transmission medium… When EM waves in space reach the front surface of the ring, the good impedance matching of MCC-50 will allow the transmission of EM waves in its interior rather than induce strong reflection at the interface" [4,44], (b) "If the characteristic impedance is poorly matched, there will be a strong reflection of incident EM waves at free space/MAMs interface… To achieve the condition of zero reflection, MAMs should have characteristic impedance as close as possible to free space. In recent works, a delta-function method was widely utilized to describe the matching degree of characteristic impedance between MAMs and free space" [5], and (c) "Recently, a Δ function has been proposed to feature the matching degree of impedance of MA materials with that of free space." [6]. Many of the confusing statements cited above are discussed below.

2.2 Impedance matching for interface and for film

Differentiating input from characteristic impedance is of crucial importance for the concept of perfect impedance matching (pim). Ignoring the difference between these two in the derivation of the Δ function [47] led to the development of the inaccurate theory of im for interface and for film. Equations (1) and (2) define reflection coefficient R_M for interface and reflection loss RL for film at position x_1 (**Figure 1**) in units of dB, respectively. All the incident beam i penetrates from free space into film without beam r when $Z_M = Z_0$, as shown by Equation (1), while beams r and t still exist although they cancel each other out when $Z_{in}(x_1^-) = Z_0$, as shown by Equation (2) [17], a fact often overlooked in publications [4-34].

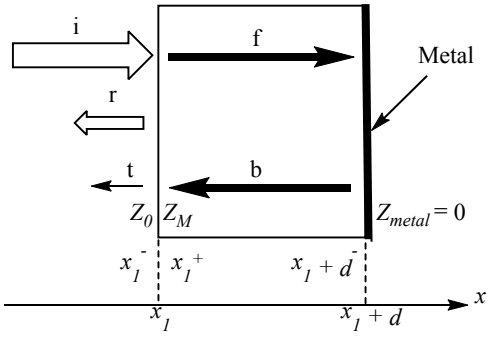

Figure 1. Metal-backed film of thickness *d*. Microwaves are reflected back and forth in the film. f is the total forward beam and b is the total backward beam in the film. i, r, and t represent incident, reflected, and the total transmitted beams, respectively. Z_0, Z_M, and Z_{Metal} are characteristic impedances of free space, material of the film, and metal, respectively. Superscripts – and + indicate immediately before and after a position, respectively.

$$R_M(x_1^-) = 20\log_{10}\left|\left[\frac{V_r(x_1^-)}{V_i(x_1^-)}\right|_{V_b(x_1^+)=0}\right] = 20\log_{10}\left|\frac{Z_M - Z_0}{Z_M + Z_0}\right| \quad (1)$$

$$RL(x_1^-) = 20\log_{10}\left|\left[\frac{V_r(x_1^-) + V_t(x_1^-)}{V_i(x_1^-)}\right|_{V(x_1+d^+)=0}\right] = 20\log_{10}\left|\frac{Z_{in}(x_1^-) - Z_0}{Z_{in}(x_1^-) + Z_0}\right| \quad (2)$$

$V_k(x)$ is the maximum amplitude of voltage at x for beam k in **Figure 1**. k can be i, r, or t.

It should be noted from Equations (1) and (2) that im for the interface cannot be achieved by adjusting Z_{in} or by changing the film thickness *d*. Thus, absorption might be related to $|Z_{in} - Z_0|$ in Equation (2), but penetration cannot be defined by it.

Nevertheless, penetration has been defined by $|Z_M - Z_0|$ from Equation (1) as in the claims: "In theory, the characteristic impedance of MAMs should be equal/close to that of the free space (377 Ω) to achieve zero-reflection at the front surface of the materials." [7], "Generally speaking, the closer the values of η_{in} are close to 377 Ω (wave impedance of free space), the better impedance matching is created." [8], and "In theory, the closer the η_{in} value is to 377 Ω (wave impedance of free space), and the better impedance is created, and the less incident EM wave will be reflected off at the boundary of MAMs, which means that more EM energy is possible to be consumed by the intrinsic attenuation ability of MAMs" [9]. In these quotes, η_{in} is Z_M for characteristic impedance. However, these claims led to the results that film can absorb more microwaves than the amount penetrated and that the energy reflected from the front interface can be drawn into the film by back-and-forth reflections in the film, illogical conclusions which show that im theory is flawed. It should be noted that wave cancellation theory [20,22] does not lead to these conclusions. The problem of im theory is that interface in film and in its isolated state are confused. Although the amplitude of the penetrated beam for film can be defined from Equation (1) [17,21], the penetrated energy for film cannot be defined.

2.3 The delta function

It follows that the widely used delta function [4-6,47-54] cannot be correct since it is based on im theory, even if the function can be fitted into experimental data from statistics, because it is applied improperly at $Z_{in}(x_1^-) \neq Z_0$, while being based on pim where $Z_{in}(x_1^-) = Z_0$ [47].

The peak of *RL* at pim is a strong narrow peak [15] which is rarely observed since the two conditions, $|Z_{in}(x_1^-)| = |Z_0|$ and that the phase of $Z_{in}(x_1^-)$ is equal to the phase of Z_0, must be met simultaneously, which is difficult to achieve. Even if the pim peak exists, it is likely to remain unobserved since the step Δf_m in the measurement is usually much larger than its width. f_m is frequency. All the reported *RL*/dB peaks are wide even for those where $|Z_{in}(x_1^-)|$ nearly equals to $|Z_0|$ [4]. For the majority of *RL*/dB peaks, $|Z_{in}(x_1^-)| \neq |Z_0|$. All the reported peaks occur where $Z_{in}(x_1^-) \neq Z_0$ and therefore the im theory is seriously flawed since the minima of *RL*/dB can occur when $|Z_{in}(x_1^-)|$ deviates far from $|Z_0|$ [20]. Impedance matching theory predicts only one sharp absorption peak at $|Z_{in}(x_1^-) = Z_0|$ which is not consistent with experimental data, while by contrast wave cancellation theory predicts a set of broad peaks whether $Z_{in}(x_1^-)$ and Z_0 are equal or not, a result which conforms to all the published experimental data.

The value of $|RL|$ is not necessarily smaller if $\delta = |Z_{in}(x_1^-)| - |Z_0|$ is smaller. In addition, the smaller of the two $|RL|$ peaks does not necessarily have a

smaller value of δ [24]. An |*RL*| peak can occur at a position with larger δ value, while there may be not a peak at all at a position with smaller value of δ [20]. These facts cannot be explained by using the delta function. In fact, im peaks are wide and they are caused by the fact that beams r and t in **Figure 1** are out of phase by π [20,22].

As in the following quote, it is believed that in order to establish *RL*/dB as the peak position, ε_r'' and μ_r'' must be large and that more incident microwave should have penetrated into the material. ("However, one should also notice that MCC-75 with the largest α values fails to produce the best EM absorption performance. This is because EM absorption efficiency is not only dependent on the overall loss capacity, but also on the impedance matching between free space and transmission medium. An imperfect impedance matching can account for strong reflection of incident EM waves at the front surface, which may invalidate the intrinsic loss capacity of the transmission medium." [4]) But this theoretical basis for *RL*/dB to decrease is only valid when ε_r'', μ_r'', or d is very large. Usually, these three parameters are small and as a result, the microwaves in the film are reflected back and forth many times. The strong peak for the film of MCC-50 is not caused by large values of ε_r'', μ_r'' [4], and the attenuation constants α, nor is it a result of im [20]. Rather, it is determined by how close are the two amplitudes of beam r reflected from the interface at x_1 and of beam t reflected from the interface at $x_1 + d$ in **Figure 1** when the two beams are out of phase by π, which is determined by the property of the film. The amplitude of beam r in **Figure 1** is determined by the reflection coefficient R_M for the interface at x_1. The amplitude of beam t is determined by R_M, d, and ε_r and μ_r, and reaches its maxima when *RL*/dB reaches its minima, a result that can be established from angular effects of film by energy conservation requirement [21,22]. On the other hand, the value of *RL*/dB changes when d increases, however, the microwave penetration characterized by Equation (1) and the attenuation power of the material characterized by ε_r'' and μ_r'' do not change.

It can be revealed from the inconsistencies [4] that im theory is wrong. The im is designed to find the minimum values of *RL*/dB. It is claimed that "the desirable delta value for good matching degree is less than 0.4" [4]. But there was no corresponding value for the first valley of *RL* [4], neither was for the second valley [4]. It is also noteworthy that the highest values of *RL*/dB do not have the highest delta values [4]. In addition, the region with $\Delta < 0.4$ includes values of *RL*/dB near 0 dB [4], which are the maximum instead of the minimum peak values of *RL*/dB. This is an example where evidence can be overlooked if not be equipped with suitable theory.

The formula for *RL* is simple and provides a clear picture from the wave superposition theory of General Physics while the formulae for the delta function are much more complex and as a result, their significance is vague. The delta function originated from statistical fitting and it does not lead to the correct solution of wave cancellation and therefore is not a suitable parameter to characterize *RL*/dB.

3. The quarter-wavelength model cannot be universally applied

The two interfaces introduced into material to form a film is responsible for the differences between film and material. However, the phase effects of the two interfaces have been neglected in the quarter-wavelength model [19,20,23]. What is more, the wavelength λ_m in film was calculated from frequency f_m and the velocity of light c in vacuum by Equation (3) [4].

$$\frac{n}{4}\lambda_m = \frac{nc}{4f_m\sqrt{|\varepsilon_r\mu_r|}} \qquad (n = 1,3,5...) \tag{3}$$

Equation (3) is wrong [19] though often applied in the field of microwave absorption material [4,34, 44,46,54-63]. The correct formula that should be used is shown in Equation (4) [19].

$$\lambda_m = \frac{c}{f_m\left|\mathrm{Re}(\sqrt{\varepsilon_r\mu_r})\right|} \tag{4}$$

The quarter-wavelength ($\lambda/4$) model claimed in the statement [4] "… which suggests that the attenuation of incident EM waves may be based

on a quarter-wavelength (λ/4) matching model. In that case, if the phase difference at the air-medium interface between incident EM waves and reflected waves from a metal-backed layer is 180°, there will be intensive consumption of EM energy due to interference cancellation…" cannot be universally applied [17,19,20,23,64], even though it is widely accepted in publications [34-37,48]. The minima of *RL/dB* occur when the phase difference of beams r and t in **Figure 1** is 180° contrary to the claim [4,34] that the phase difference of beams r and i is 180° as "the phase difference between the incident wave and the reflective wave is 180°" [34]. In fact, as indicated by Equation (2), *RL*/dB is only related to the power ratio of the resultant beam (r + t) to the incident beam i. The power ratio is only related to the maximum amplitude of voltages but has nothing to do with the phase difference between beams (r + t) and i. However, the maximum amplitude of voltage for beam (r + t) is related to the phase difference between beams r and t [19].

It is stated that "It is very interesting that with the increase of coating thickness, the minimum *RL* peaks of all these composites gradually shift towards low-frequency region which suggests that the attenuation of incident EM waves may be based on a quarter-wavelength (λ/4) matching model" [4]. But this is neither interesting nor indeed true.

$$RL(x_1^-) = \frac{R_M(x_1^-)e^{2j\pi f_m\frac{\sqrt{\varepsilon_r\mu_r}}{c}d} - e^{-2j\pi f_m\frac{\sqrt{\varepsilon_r\mu_r}}{c}d}}{e^{2j\pi f_m\frac{\sqrt{\varepsilon_r\mu_r}}{c}d} - R_M(x_1^-)e^{-2j\pi f_m\frac{\sqrt{\varepsilon_r\mu_r}}{c}d}} \quad (5)$$

As can be seen from Equation (5), if $|RL(x_1^-)|$ achieves a minima at f_m and d, it will retain the same peak value when the frequency decreases to $f_m/2$ and the film thickness increases to $2d$ if both ε_r and μ_r are constants. In other words, the peak values will be found on the inverse curve of f_m and d if ε_r and μ_r are insensitive to frequency [23].

4. Conclusions

The criticisms included here are not just concerned with the work of Du et al. [4] as they can be applied to many other published works in this field. It is a general comment on the prevailing theories applied to microwave absorption including the application of *RL* to characterize material, the im theory, the delta function, and the quarter-wavelength model. Judged by the value of *RL*/dB, except in extreme cases, it is found that the material most suitable for microwave absorption film is not usually the one with the highest values of ε_r'', μ_r'', and the attenuation constants α of the material, nor the one which allows most of the incident microwaves to penetrate the film as supposed by the im theory. In fact, the most suitable material has the most balanced amplitudes at x_1^- for the two beams reflected from the two interfaces in the film when the two beams at x_1^- in **Figure 1** are out of phase by π. This work shows that the claim: "the most highly utilized method for determining material response to incident electromagnetic radiation in the microwave region" "appears to have been demonstrated experimentally" [65] is unjustified.

Author Contributions

Ying Liu: Conceptualization, Methodology, Validation, Investigation, Resources, Writing - Review & Editing, Supervision, Project administration, Funding acquisition.

Xiangbin Yin: Validation, Investigation.

Michael G. B. Drew: Conceptualization, Validation, Writing - Review & Editing, Supervision.

Yue Liu: Conceptualization, Methodology, Validation, Formal analysis, Investigation, Writing - Review & Editing, Visualization.

Conflict of Interest

There is no conflict of interest.

Acknowledgements

This work was supported by the Foundation of Liaoning Province Education Administration [grant number LJKMZ20221477].

References

[1] Vazire, S., 2020. A toast to the error detectors.

Nature. 577(7788), 9-10.
DOI: https://doi.org/10.1038/d41586-019-03909-2

[2] Ioannidis, J.P., 2005. Why most published research findings are false. PLoS Medicine. 2(8), e124.
DOI: https://doi.org/10.1371/journal.pmed.0020124

[3] Liu, Y., Liu, Y., Drew, M.G., 2020. Clarifications of concepts concerning interplanar spacing in crystals with reference to recent publications. SN Applied Sciences. 2, 1-29.
DOI: https://doi.org/10.1007/s42452-020-2498-5

[4] Wang, Y., Li, X., Han, X., et al., 2020. Ternary Mo_2C/Co/C composites with enhanced electromagnetic waves absorption. Chemical Engineering Journal. 387, 124159.
DOI: https://doi.org/10.1016/j.cej.2020.124159

[5] Wang, Y., Han, X., Xu, P., et al., 2019. Synthesis of pomegranate-like Mo_2C@ C nanospheres for highly efficient microwave absorption. Chemical Engineering Journal. 372, 312-320.
DOI: https://doi.org/10.1016/j.cej.2019.04.153

[6] Wang, Y., Li, C., Han, X., et al., 2018. Ultrasmall Mo_2C nanoparticle-decorated carbon polyhedrons for enhanced microwave absorption. ACS Applied Nano Materials. 1(9), 5366-5376.
DOI: https://doi.org/10.1021/acsanm.8b01479

[7] Wang, Y., Du, Y., Xu, P., et al., 2017. Recent advances in conjugated polymer-based microwave absorbing materials. Polymers. 9(1), 29.
DOI: https://doi.org/10.3390/polym9010029

[8] Wang, F., Liu, Y., Zhao, H., et al., 2022. Controllable seeding of nitrogen-doped carbon nanotubes on three-dimensional Co/C foam for enhanced dielectric loss and microwave absorption characteristics. Chemical Engineering Journal. 450, 138160.
DOI: https://doi.org/10.1016/j.cej.2022.138160

[9] Liu, Y., Tian, C., Wang, F., et al., 2023. Dual-pathway optimization on microwave absorption characteristics of core-shell Fe_3O_4@ C microcapsules: Composition regulation on magnetic core and MoS_2 nanosheets growth on carbon shell. Chemical Engineering Journal. 461, 141867.
DOI: https://doi.org/10.1016/j.cej.2023.141867

[10] Du, Y., 2022. Advances in carbon-based microwave absorbing materials. Materials. 15(4), 1359.
DOI: https://doi.org/10.3390/ma15041359

[11] Wang, F., Xu, P., Shi, N., et al., 2021. Polymer-bubbling for one-step synthesis of three-dimensional cobalt/carbon foams against electromagnetic pollution. Journal of Materials Science & Technology. 93, 7-16.
DOI: https://doi.org/10.1016/j.jmst.2021.03.048

[12] Zhao, H., Wang, F., Cui, L., et al., 2021. Composition optimization and microstructure design in MOFs-derived magnetic carbon-based microwave absorbers: A review. Nano-Micro Letters. 13, 1-33.
DOI: https://doi.org/10.1007/s40820-021-00734-z

[13] Wang, F., Cui, L., Zhao, H., et al., 2021. High-efficient electromagnetic absorption and composites of carbon microspheres. Journal of Applied Physics. 130(23), 230902.
DOI: https://doi.org/10.1063/5.0068122

[14] Wang, P., Liu, D., Cui, L., et al., 2021. A review of recent advancements in Ni-related materials used for microwave absorption. Journal of Physics D: Applied Physics. 54(47), 473003.
DOI: https://doi.org/10.1088/1361-6463/ac196d

[15] Liu, Y., Zhao, K., Drew, M.G., et al., 2018. A theoretical and practical clarification on the calculation of reflection loss for microwave absorbing materials. AIP Advances. 8(1), 015223.
DOI: https://doi.org/10.1063/1.4991448

[16] Liu, Y., Yu, H., Drew, M.G., et al., 2018. A systemized parameter set applicable to microwave absorption for ferrite based materials. Journal of Materials Science: Materials in Electronics. 29(2), 1562-1575.
DOI: https://doi.org/10.1007/s10854-017-8066-0

[17] Liu, Y., Drew, M.G., Li, H., et al., 2020. An experimental and theoretical investigation into methods concerned with “reflection loss” for microwave absorbing materials. Materials Chemistry and Physics. 243, 122624.

DOI: https://doi.org/10.1016/j.matchemphys.2020.122624

[18] Liu, Y., Drew, M.G., Li, H., et al., 2021. A theoretical analysis of the relationships shown from the general experimental results of scattering parameters s 11 and s 21—exemplified by the film of $BaFe_{12}$-i Ce i O_{19}/polypyrene with i= 0.2, 0.4, 0.6. Journal of Microwave Power and Electromagnetic Energy. 55(3), 197-218.
DOI: https://doi.org/10.1080/08327823.2021.1952835

[19] Liu, Y., Liu, Y., Drew, M.G., 2021. A theoretical investigation on the quarter-wavelength model—part 1: Analysis. Physica Scripta. 96(12), 125003.
DOI: https://doi.org/10.1088/1402-4896/ac1eb0

[20] Liu, Y., Liu, Y., Drew, M.G., 2022. A theoretical investigation of the quarter-wavelength model—part 2: Verification and extension. Physica Scripta. 97(1), 015806.
DOI: https://doi.org/10.1088/1402-4896/ac1eb1

[21] Liu, Y., Liu, Y., Drew, M.G., 2022. A Re-evaluation of the mechanism of microwave absorption in film—Part 1: Energy conservation. Materials Chemistry and Physics. 290, 126576.
DOI: https://doi.org/10.1016/j.matchemphys.2022.126576

[22] Liu, Y., Liu, Y., Drew, M.G., 2022. A Re-evaluation of the mechanism of microwave absorption in film—Part 2: The real mechanism. Materials Chemistry and Physics. 291, 126601.
DOI: https://doi.org/10.1016/j.matchemphys.2022.126601

[23] Liu, Y., Liu, Y., Drew, M.G., 2022. A re-evaluation of the mechanism of microwave absorption in film—Part 3: Inverse relationship. Materials Chemistry and Physics. 290, 126521.
DOI: https://doi.org/10.1016/j.matchemphys.2022.126521

[24] Liu, Y., Yin, X., Drew, M.G.B., et al., 2023. Microwave absorption of film explained accurately by wave cancellation theory. Preprint.
DOI: https://doi.org/10.21203/rs.3.rs-2616469/v2

[25] Wu, Z., Cheng, H.W., Jin, C., et al., 2022. Dimensional design and core-shell engineering of nanomaterials for electromagnetic wave absorption. Advanced Materials. 34(11), 2107538.
DOI: https://doi.org/10.1002/adma.202107538

[26] Cheng, J., Zhang, H., Ning, M., et al., 2022. Emerging materials and designs for low-and multi-band electromagnetic wave absorbers: The search for dielectric and magnetic synergy?. Advanced Functional Materials. 32(23), 2200123.
DOI: https://doi.org/10.1002/adfm.202200123

[27] Xia, Y., Gao, W., Gao, C., 2022. A review on graphene-based electromagnetic functional materials: Electromagnetic wave shielding and absorption. Advanced Functional Materials. 32(42), 2204591.
DOI: https://doi.org/10.1002/adfm.202204591

[28] Xia, L., Feng, Y., Zhao, B., 2022. Intrinsic mechanism and multiphysics analysis of electromagnetic wave absorbing materials: New horizons and breakthrough. Journal of Materials Science & Technology. 130, 136-156.
DOI: https://doi.org/10.1016/j.jmst.2022.05.010

[29] Planck, M., 1950. Scientific autobiography and other paper. William & Norgate: London. pp. 33-34.

[30] Liu, Y., Lin, Y., Zhao, K., et al., 2020. Microwave absorption properties of Ag/$NiFe_2$-x$CexO_4$ characterized by an alternative procedure rather than the main stream method using "reflection loss". Materials Chemistry and Physics. 243, 122615.
DOI: https://doi.org/10.1016/j.matchemphys.2019.122615

[31] Kim, S.S., Han, D.H., Cho, S.B., 1994. Microwave absorbing properties of sintered Ni-Zn ferrite. IEEE Transactions on Magnetics. 30(6), 4554-4556.

[32] Wu, C., Bi, K., Yan, M., 2020. Scalable self-supported $FeNi_3$/Mo_2C flexible paper for enhanced electromagnetic wave absorption evaluated via coaxial, waveguide and arch methods. Journal of Materials Chemistry C. 8(30), 10204-10212.

DOI: https://doi.org/10.1039/d0tc01881c

[33] Li, Q., Zhao, Y., Li, X., et al., 2020. MOF induces 2D GO to assemble into 3D accordion-like composites for tunable and optimized microwave absorption performance. Small. 16(42), 2003905.
DOI: https://doi.org/10.1002/smll.202003905

[34] Zeng, S., Yao, Y., Feng, W., et al., 2020. Constructing a 3D interconnected Fe@ graphitic carbon structure for a highly efficient microwave absorber. Journal of Materials Chemistry C. 8(4), 1326-1334.
DOI: https://doi.org/10.1039/c9tc05615g

[35] Yu, X.F., Zhang, Y., Wang, L., et al., 2020. Boosted microwave absorption performance of multi-dimensional Fe_2O_3/CNTsCM@CN assembly by enhanced dielectric relaxation. Journal of Materials Chemistry C. 8(17), 5715-5726.
DOI: https://doi.org/10.1039/d0tc00941e

[36] Zhou, W., Long, L., Bu, G., et al., 2019. Mechanical and microwave-absorption properties of Si3N4 ceramic with SiCNFs fillers. Advanced Engineering Materials. 21(5), 1800665.
DOI: https://doi.org/10.1002/adem.201800665

[37] Lin, H., Green, M., Xu, L.J., et al., 2020. Microwave absorption of organic metal halide nanotubes. Advanced Materials Interfaces. 7(3), 1901270.
DOI: https://doi.org/10.1002/admi.201901270

[38] Ye, F., Song, Q., Zhang, Z., et al., 2018. Direct growth of edge-rich graphene with tunable dielectric properties in porous Si_3N_4 ceramic for broadband high-performance microwave absorption. Advanced Functional Materials. 28(17), 1707205.
DOI: https://doi.org/10.1002/adfm.201707205

[39] Sun, X., Yang, M., Yang, S., et al., 2019. Ultrabroad band microwave absorption of carbonized waxberry with hierarchical structure. Small. 15(43), 1902974.
DOI: https://doi.org/10.1002/smll.201902974

[40] Ding, J., Wang, L., Zhao, Y., et al., 2019. Boosted interfacial polarization from multishell TiO_2@ Fe_3O_4@ PPy heterojunction for enhanced microwave absorption. Small. 15(36), 1902885.
DOI: https://doi.org/10.1002/smll.201902885

[41] Green, M., Tran, A.T., Chen, X., 2020. Obtaining strong, broadband microwave absorption of polyaniline through data-driven materials discovery. Advanced Materials Interfaces. 7(18), 2000658.
DOI: https://doi.org/10.1002/admi.202000658

[42] Wang, X., Du, Z., Hou, M., et al., 2022. Approximate solution of impedance matching for nonmagnetic homogeneous absorbing materials. The European Physical Journal Special Topics. 231(24), 4213-4220.
DOI: https://doi.org/10.1140/epjs/s11734-022-00570-1

[43] Liu, Y., Li, X., Drew, M.G., et al., 2015. Increasing microwave absorption efficiency in ferrite based materials by doping with lead and forming composites. Materials Chemistry and Physics. 162, 677-685.
DOI: https://doi.org/10.1016/j.matchemphys.2015.06.042

[44] Liu, J., Jia, Z., Zhou, W., et al., 2022. Self-assembled MoS_2/magnetic ferrite $CuFe_2O4$ nanocomposite for high-efficiency microwave absorption. Chemical Engineering Journal. 429, 132253.
DOI: https://doi.org/10.1016/j.cej.2021.132253

[45] Zhu, X., Qiu, H., Chen, P., et al., 2021. Anemone-shaped ZIF-67@ CNTs as effective electromagnetic absorbent covered the whole X-band. Carbon. 173, 1-10.
DOI: https://doi.org/10.1016/j.carbon.2020.10.055

[46] Zhu, X., Qiu, H., Chen, P., et al., 2021. Graphitic carbon nitride (g-C_3N_4) in situ polymerization to synthesize MOF-Co@ CNTs as efficient electromagnetic microwave absorption materials. Carbon. 176, 530-539.
DOI: https://doi.org/10.1016/j.carbon.2021.02.044

[47] Ma, Z., Zhang, Y., Cao, C., et al., 2011. Attractive microwave absorption and the impedance match effect in zinc oxide and carbonyl iron composite. Physica B: Condensed Matter.

406(24), 4620-4624.
DOI: https://doi.org/10.1016/j.physb.2011.09.039

[48] Huang, Y., Ji, J., Chen, Y., et al., 2019. Broadband microwave absorption of $Fe_3O_4BaTiO_3$ composites enhanced by interfacial polarization and impedance matching. Composites Part B: Engineering. 163, 598-605.
DOI: https://doi.org/10.1016/j.compositesb.2019.01.008

[49] Cheng, Y., Hu, P., Zhou, S., et al., 2018. Achieving tunability of effective electromagnetic wave absorption between the whole X-band and Ku-band via adjusting PPy loading in SiC nanowires/graphene hybrid foam. Carbon. 132, 430-443.
DOI: https://doi.org/10.1016/j.carbon.2018.02.084

[50] Liu, D., Qiang, R., Du, Y., et al., 2018. Prussian blue analogues derived magnetic FeCo alloy/carbon composites with tunable chemical composition and enhanced microwave absorption. Journal of Colloid and Interface Science. 514, 10-20.
DOI: https://doi.org/10.1016/j.jcis.2017.12.013

[51] Qiang, R., Du, Y., Chen, D., et al., 2016. Electromagnetic functionalized Co/C composites by in situ pyrolysis of metal-organic frameworks (ZIF-67). Journal of Alloys and Compounds. 681, 384-393.
DOI: https://doi.org/10.1016/j.jallcom.2016.04.225

[52] Cui, L., Tian, C., Tang, L., et al., 2019. Space-confined synthesis of core-shell $BaTiO_3$@ Carbon microspheres as a high-performance binary dielectric system for microwave absorption. ACS Applied Materials & Interfaces. 11(34), 31182-31190.
DOI: https://doi.org/10.1021/acsami.9b09779

[53] Zhang, X., Qiao, J., Jiang, Y., et al., 2021. Carbon-based MOF derivatives: Emerging efficient electromagnetic wave absorption agents. Nano-Micro Letters. 13, 135.
DOI: https://doi.org/10.1007/s40820-021-00658-8

[54] Liu, H., Zhang, M., Hu, K., et al., 2021. High-efficiency microwave absorption performance of cobalt ferrite microspheres/multi-walled carbon nanotube composites. Journal of Materials Science: Materials in Electronics. 32, 26021-26033.
DOI: https://doi.org/10.1007/s10854-021-05877-8

[55] Min, W., Xu, D., Chen, P., et al., 2021. Synthesis of novel hierarchical CoNi@ NC hollow microspheres with enhanced microwave absorption performance. Journal of Materials Science: Materials in Electronics. 32(6), 8000-8016.
DOI: https://doi.org/10.1007/s10854-021-05523-3

[56] Chen, G., Xu, D., Chen, P., et al., 2021. Constructing and optimizing hollow bird-nest-patterned C@ Fe_3O_4 composites as high-performance microwave absorbers. Journal of Magnetism and Magnetic Materials. 532, 167990.
DOI: https://doi.org/10.1016/j.jmmm.2021.167990

[57] Qiu, H., Zhu, X., Chen, P., et al., 2021. Synthesis of ternary core-shell structured ZnOC@ CoC@ PAN for high-performance electromagnetic absorption. Journal of Alloys and Compounds. 868, 159260.
DOI: https://doi.org/10.1016/j.jallcom.2021.159260

[58] Zhang, Z., Cai, Z., Wang, Z., et al., 2021. A review on metal—organic framework-derived porous carbon-based novel microwave absorption materials. Nano-Micro Letters. 13(1), 1-29.
DOI: https://doi.org/10.1007/s40820-020-00582-3

[59] Zhang, X., Ren, X., Wang, C., et al., 2021. Synthesis of layered Fe_3O_4 nanodisk and nanostructure dependent microwave absorption property. Journal of Materials Science: Materials in Electronics. 32(4), 4404-4415.
DOI: https://doi.org/10.1007/s10854-020-05183-9

[60] Zhang, H., Pang, H., Duan, Y., et al., 2021. Facile morphology controllable synthesis of zinc oxide decorated carbon nanotubes with enhanced microwave absorption. Journal of Materials Science: Materials in Electronics. 32(9), 12208-12222.
DOI: https://doi.org/10.1007/s10854-021-05850-5

[61] Yuan, M., Yao, Q., Zhou, H., et al., 2021. Effect of Pr_2Fe_{17} alloy doping Cr on magnetic and microwave absorption properties. Journal of Mate-

rials Science: Materials in Electronics. 32(10), 13108-13116.
DOI: https://doi.org/10.1007/s10854-021-05801-0

[62] Huang, F., Wang, S., Ding, W., et al., 2021. Sulfur-doped biomass-derived hollow carbon microtubes toward excellent microwave absorption performance. Journal of Materials Science: Materials in Electronics. 32(5), 6260-6268.
DOI: https://doi.org/10.1007/s10854-021-05341-7

[63] Bao, X.K., Shi, G.M., Wang, X.L., et al., 2021. Effect of nitrogen-doping content on microwave absorption performances of Ni@ NC nanocapsules. Journal of Materials Science: Materials in Electronics. 32(1), 1007-1021.
DOI: https://doi.org/10.1007/s10854-020-04876-5

[64] Liu, Y., Drew, M.G., Liu, Y., 2019. Characterization microwave absorption from active carbon/$BaSm_xFe_{12-x}O_{19}$/polypyrrole composites analyzed with a more rigorous method. Journal of Materials Science: Materials in Electronics. 30(2), 1936-1956.
DOI: https://doi.org/10.1007/s10854-018-0467-1

[65] Green, M., Chen, X., 2019. Recent progress of nanomaterials for microwave absorption. Journal of Materiomics. 5(4), 503-541.
DOI: https://doi.org/10.1016/j.jmat.2019.07.003

BILINGUAL PUBLISHING GROUP

Non-Metallic Material Science

https://journals.bilpubgroup.com/index.php/nmms

ARTICLE

Synthesis, Characterization and Impedance Analysis of Calcium-Doped Zinc Oxide Nanoparticles

K. N. Ganesha[1,2], H. Chandrappa[2], S. R. Kumarswamy[3], V. Annadurai[4], H. Somashekarappa[1*], R. Somashekar[5]

[1] *Department of Physics, Yuvaraja's College, University of Mysore, Mysuru, Karnataka, 570005, India*

[2] *SRSMN Govt. First Grade College & PG Study Centre, Barkur, Udupi, Karnataka, 576210, India*

[3] *Government First Grade College for Women, Byrapura, T. Narasipura, Mysuru, Karnataka, 571124, India*

[4] *Department of Physics, NIE First Grade College, University of Mysore, Mysuru-570008, India*

[5] *Institution of Excellence, Vijnana Bhavana, Manasagangothri, Mysuru, 570006, India*

ABSTRACT

The calcium-doped ZnO nanoparticles, $Zn_{1-x}Ca_xO$ (x = 0, 0.025, 0.05, 0.075) were prepared by the solution combustion method. The synthesized nanoparticles were characterized by various techniques such as XRD, FTIR, Raman, FESEM-EDX, PL, Impedance, and UV-Vis. The Rietveld refinement of the X-ray diffractogram yields the crystalline structure and lattice parameters. Also, the XRD analysis shows that the substitution of Ca into ZnO does not alter the Wurtzite structure of ZnO. The crystallite size of the samples, calculated using the Scherer equation, was found to be between 46 nm and 92 nm. FTIR spectra detect the ZnO-related vibration modes of the samples. The FESEM morphological images suggest the spherical shape of the synthesized nanoparticles. The EDAX spectra identify the presence of Zn, Ca, and O atoms in the samples. The Raman active modes of the ZnO phase were identified by Raman spectral analysis. The analysis of Photoluminescence (PL) spectra gives information about the UV emission and other visible bands corresponding to violet, blue, and green emission representing different intrinsic defects in synthesized nanoparticles. Using UV-vis spectroscopy, the optical transparency and band gap values were examined. The energy band gap obtained by Tauc's plot was decreased with the increase in Ca doping. Impedance analysis shows that the grain conductivity increased with the increase in dopant concentration. Contrarily, the total conductivity decreased with the increasing doping concentration due to increased grain boundary resistance. The proposed work demonstrates the changes in microstructure, electrical conductivity, and optical bandgap energy with Ca-doping. These synthesized Ca-doped ZnO nanoparticles could be promising materials for photocatalytic applications.

Keywords: Solution combustion synthesis; ZnO; Impedance; Optical properties; Photoluminescence

*CORRESPONDING AUTHOR:

H. Somashekarappa, Department of Physics, Yuvaraja's College, University of Mysore, Mysuru, Karnataka, 570005, India; Email: drhssappa@gmail.com

ARTICLE INFO

Received: 22 April 2023 | Revised: 15 May 2023 | Accepted: 16 May 2023 | Published Online: 25 May 2023

DOI: https://doi.org/10.30564/nmms.v5i1.5677

CITATION

Ganesha, K.N., Chandrappa, H., Kumarswamy, S.R., et al., 2023. Synthesis, Characterization and Impedance Analysis of Calcium Doped Zinc Oxide Nanoparticles. Non-Metallic Material Science. 5(1): 49-63. DOI: https://doi.org/10.30564/nmms.v5i1.5677

1. Introduction

As the most studied zinc oxide (ZnO), it offers some attractive properties due to its size-dependent optoelectronic properties. In recent days, ZnO has revolutionized the optoelectronics industry due to its interesting semiconducting, pyroelectric, and piezoelectric properties. ZnO has diverse applications such as gas/chemical sensors [1-3], optoelectronics [4], laser diodes [5], piezo electronics [6,7], photo-catalysis [8], food packaging [9], biomedical [10], personal care and cosmetics [11] and field emission devices [12]. Basically, ZnO (group II-VI) is a wide-bandgap semiconductor with unique physical properties. It has a direct band gap energy of 3.37 eV with a free exciton binding energy of 60 meV. Therefore, it has a pronounced effect on optical and electrical properties [13,14]. It is well established that particle size and morphology, reaction temperature, solution pH, dopants, and dopant concentrations alter the physical, chemical, electrical, and optical properties of ZnO [15-21]. ZnO nanoparticles can be obtained by various synthesis methods such as co-precipitation [22,23], combustion [24], sol-gel [25,26], hydrothermal [27], etc. Many researchers have synthesized Ca-doped ZnO, and the observed properties have been used in many applications. For example, Davalasab Ilager et al. modified a carbon-based electrochemical sensor with Ca-doped ZnO nanoparticles for an anti-viral drug, and acyclovir [28,29]. S. Jaballah et al. fabricated a Ca-doped zinc oxide gas sensor that exhibits good formaldehyde detection properties [30]. Here, the authors made an attempt to prepare the Ca-doped ZnO by solution combustion synthesis technique. This technique is preferred over other synthesis approaches on account of the major advantage that allows homogeneous phase formation at lower temperatures or at shorter reaction times than conventional methods such as solid-state and mechano-synthesis routes [31]. No extensive literature on the combination of electrical and optical properties and the nanocrystalline phase of this material. An idea about the charge carriers, bandgap energy, and electrical conductivity of this material is essential. The details of structural modifications with Ca doping on ZnO material have been obtained using Rietveld refinement from the XRD data. The principle objective of the current work is to investigate and discuss the influence of Ca doping on the structural, morphological, optical, and electrical properties of synthesized ZnO nanoparticles.

2. Experimental

2.1 Solution combustion synthesis

In a typical solution combustion synthesis, the metal nitrates act as oxidizing agents, and the organic fuels as the reducing agents [24,32]. To prepare $Zn_{1-x}Ca_xO$ (x = 0, 0.025, 0.05, 0.075), Zinc Nitrate Hexahydrate [$Zn(NO_3)_2 \cdot 6H_2O$] (99%), Calcium Nitrate Tetra hydrate [$Ca(NO_3)_2 \cdot 4H_2O$] (99.9%) were used as the precursor (oxidizing agent) and citric acid [$C_6H_8O_7$] (99%) as the fuel. All the chemicals used for the preparation are AR grade. The fuel and oxidant ratio was maintained at one during the preparation. 1 = O/(-n)F, where n is the fuel mole fraction, O is the oxidation valence, and F is the reduction valence [33]. The fuel mole fraction was calculated based on the valences of the oxidizing and reducing elements. Valences of elements like +1 for H, +4 for C, −2 for O, and 0 for N. Valences for metal elements like +2 for Zn and +2 for Ca. The oxidizing valence of $Zn(NO_3)_2 \cdot 6H_2O$ is −10, $Ca(NO_3)_2.4H_2O$ is −10, and the reducing valence of citric acid is +18. The amount of citric acid (fuel) calculated for the reaction is n = 0.56M.

Stoichiometric amounts of $Zn(NO_3)_2 \cdot 6H_2O$ and $Ca(NO_3)_2 \cdot 4H_2O$ and $C_6H_8O_7$ were dissolved in separate beakers with double distilled water. A clear solution of metal nitrates was intimately mixed in a beaker equipped with a magnetic stirrer until a clear solution was formed. Citric acid fuel was also dissolved in distilled water in a separate beaker with a magnetic stirrer until a clear solution was obtained. The above solutions were mixed then the resulting aqueous solution was thoroughly stirred with a magnetic stirrer at room temperature for about 30 minutes until a clear solution was formed. At low pH, nitrates reduce the enthalpy of the exothermic reaction under this condition and the particles agglomerate [34]. The

pH of the solution is maintained at 7 by adding ammonium hydroxide. By heating this mixture at 80 °C under constant stirring for 8 h, the excess water and nitrate gas were removed to form a transparent and viscous gel. Excess water and nitric acid gas were removed to form a clear, viscous gel. Further heating of the gel at 150 °C causes it to ignite and burn completely, forming a carbonaceous powder. The obtained powder material was allowed to cool and ground in an agate mortar to get a fine powder, then annealed at 800 °C for 6 hours to obtain phase pure calcium-doped zinc oxide nanoparticles.

2.2 Characterization

X-ray diffractogram (XRD) patterns were recorded using the X-ray Diffractometer (Bruker AXS D8 Advance) fitted with Cu-Kα radiation (λ = 1.5406 Å) to get structural information of the prepared nanoparticles. The vibrational modes of the samples were characterized using an FTIR spectrometer (Perkin Elmer Spectrum1) and a Raman spectrometer (LabRAM HR 800, HORIBA, excitation laser 532 nm). The surface morphology and elemental analysis of the samples were investigated by FESEM and EDAX (ΣIGMAZEISS FESEM). Optical absorption spectra were recorded over the wavelength range of 350-800 nm using an ultraviolet-visible-near-infrared (UV-VIS-NIR) spectrophotometer (Perkin Elmer UV Lambda 900). Photoluminescence (PL) was measured using HORIBA with a laser light excitation wavelength of 355 nm. Electrical impedance measurements were made at room temperature from 100 Hz to 1 MHz using a Wayne Kerr 6500B Precision Impedance Analyzer. The silver paste was applied evenly on both sides of the pellet to ensure good electrical contact.

3. Results and discussion

3.1 Structural analysis

Figure 1 shows the powder XRD patterns of samples prepared with $Zn_{1-x}Ca_xO$ (x = 0, 0.025, 0.05, 0.075) calcined at 800 °C. A hexagonal wurtzite structure with space group $P6_3mc$ (JCPDS01-075-0576) is evident from the XRD pattern. Ca^{2+} doping does not show any additional peaks in the diffractograms, confirming that Ca is perfectly incorporated into the ZnO matrix without altering the wurtzite structure. A negligible shift in peak positions towards lower 2θ values was observed with Ca doping. The shift to smaller angles was caused by the larger radius of the Ca^{2+} ion (0.99 Å) [23]. XRD diffractograms were examined with the Rietveld fitting using FullProf software. **Figure 2** shows the Rietveld refinement (Fullprof) of XRD pattern for ZnO (CA00), $Zn_{0.975}Ca_{0.025}O$ (CA25), $Zn_{0.95}Ca_{0.05}O$ (CA50) and $Zn_{0.925}Ca_{0.075}O$ (CA75) nanoparticles. **Table 1** illustrates the lattice and the Rietveld parameters χ^2 (reduced chi-square) obtained by the Rietveld fit. The χ^2 values of the samples vary between 1.42 and 3.42, which justifies the goodness of refinement. All samples converge to a hexagonal wurtzite structure of space group $P6_3mc$. In the Wurtzite structure, Zn^{2+} is bonded to four equivalent O^{2-} atoms to form a corner-sharing ZnO_4 tetrahedra. Although Ca ions occupy regular lattice sites in ZnO, variations in lattice parameter values produce crystal defects around the dopants, and it has been suggested that these defects change the stoichiometry of the material.

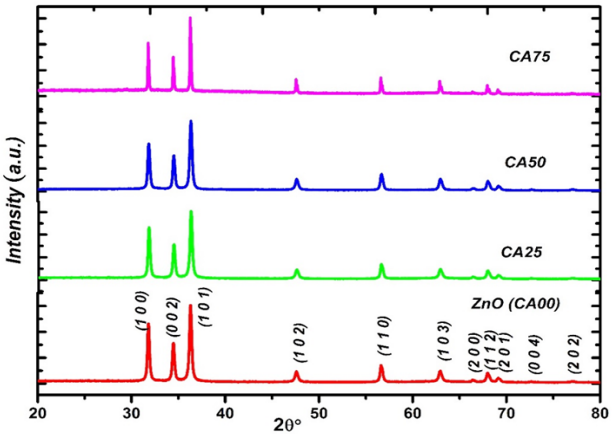

Figure 1. XRD pattern of ZnO (CA00), $Zn_{0.975}Ca_{0.025}O$ (CA25), $Zn_{0.95}Ca_{0.05}O$ (CA50), and $Zn_{0.925}Ca_{0.075}O$ (CA75) nanoparticles calcined at 800 °C.

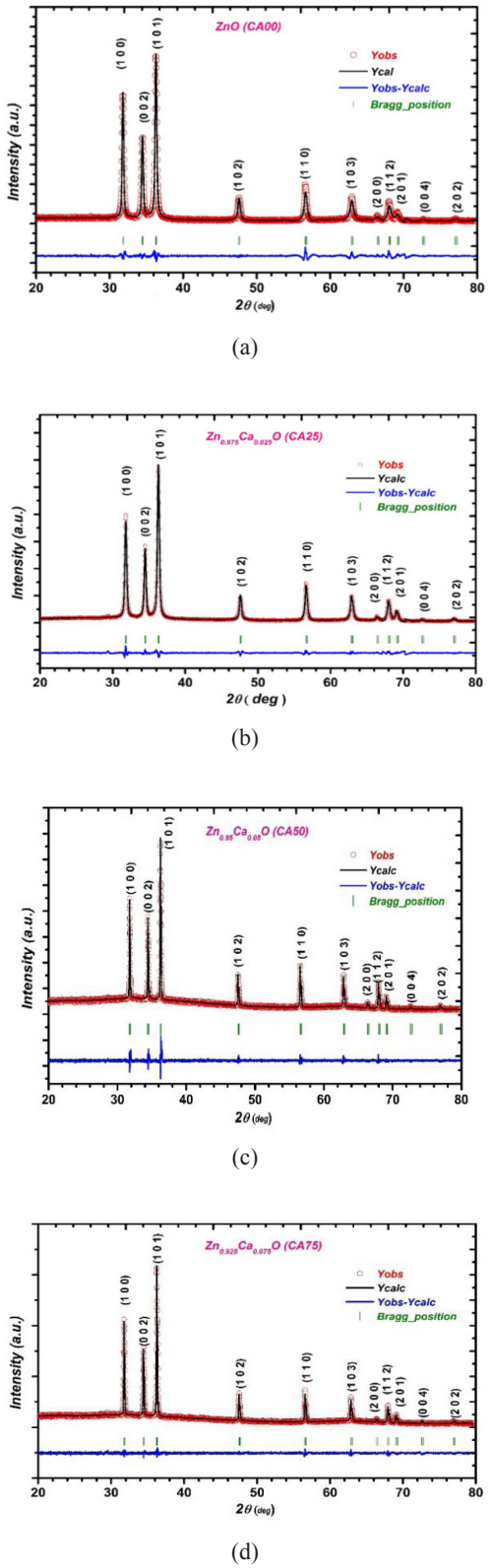

Figure 2. Rietveld fit of pure and Ca-doped ZnO nanoparticles (a) ZnO (CA00), (b) $Zn_{0.975}Ca_{0.025}O$ (CA25), (c) $Zn_{0.95}Ca_{0.05}O$ (CA50) and (d) $Zn_{0.925}Ca_{0.075}O$ (CA75).

The average crystallite size (D) is estimated using Debye-Scherrer's equation [35] as follows:

$$D = \frac{K\lambda}{\beta \cos\theta} \quad (1)$$

where D is the average crystallite size, K is a constant (0.9), λ is the wavelength of X-rays, β is the full width at half maxima (FWHM) of a (101) reflection peak, and θ is the Bragg's diffraction angle.

The calculated crystallite size values are shown in **Table 1**. The average crystallite size was found to be the smallest (42 nm) for CA25 and the largest (92 nm) for CA75. This indicates that the average crystallite size increases with increasing dopant concentration. The bond length (L) of Zn-O was calculated from the relation [26]:

$$L = \sqrt{\frac{a^2}{3} + \left(\frac{1}{2} - u\right)^2 c^2} \quad (2)$$

where *a* and *c* are lattice constants and *u* is a positional parameter. The parameter *u* can be calculated by using the formula: $u=(a^2/3c^2)+0.25$. The calculated positional parameters and bond lengths are also shown in **Table 1**. It was observed that the bond length increased slightly with increasing Ca concentration.

3.2 Fourier Transform Infra-Red (FTIR) spectra analysis

The characteristics vibrational frequencies of $Zn_{1-x}Ca_xO$ nanoparticles with wurtzite structure were identified using FTIR spectra. **Figure 3** shows the FTIR spectra of the prepared samples. Infrared active optical phonon modes in ZnO were observed in the spectral range from 300 to 600 cm^{-1} [26,36]. The absorption peaks observed between 401-412 cm^{-1} can be assigned to the E_1 (TO) mode of pure and Ca-doped ZnO. The band 484 cm^{-1} can be assigned to the surface phonon mode A_1(TO). Two additional bands, 912 cm^{-1} and 1010 cm^{-1} were assigned to the vibrational frequencies due to the changes in the microstructural features by adding Ca into the ZnO lattice [37,38].

Table 1. XRD analysis results of ZnO and Ca-doped ZnO nanoparticles.

Sample	a=b (Å)	C (Å)	Atomic packing factor (c/a)	Volume $(Å)^3$	Average crystallite size D (nm)	χ^2	Bond length Zn-O L (Å)	Position parameters u
CA00	3.2482	5.2036	1.602	47.54	52	3.32	1.976	0.379
CA25	3.2479	5.2032	1.602	47.54	46	3.42	1.976	0.379
CA50	3.2505	5.2051	1.601	47.63	50	1.95	1.977	0.379
CA75	3.2504	5.2049	1.601	47.62	92	1.42	1.977	0.380

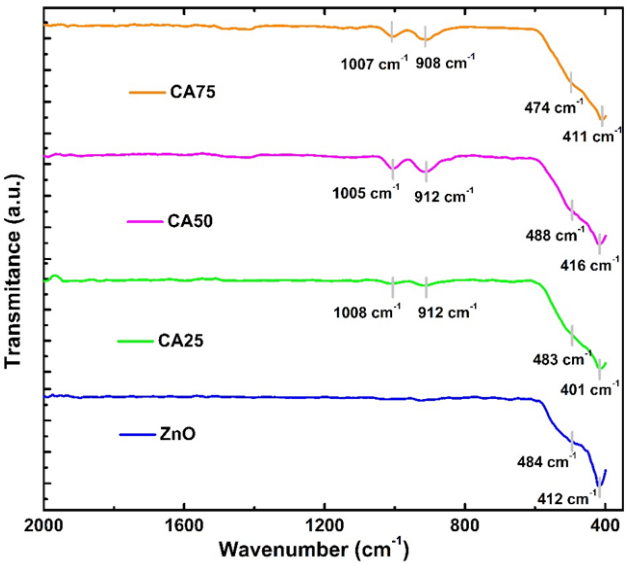

Figure 3. FTIR absorption spectra of pure ZnO and Ca-doped ZnO nanoparticles.

3.3 Raman analysis

The lattice vibrational properties of the prepared samples were studied by Raman spectroscopy. The prepared sample $Zn_{1-x}Ca_xO$ (x = 0. 0.025, 0.05, 0.075) crystallizes into a wurtzite structure with symmetry $P6_3mc$. Since there are four atoms per unit cell in the wurtzite structure, there are 12 phonon modes. Among 12 modes, three longitudinal-optical (LO), six transverse optical (TO) branches, one longitudinal-acoustic (LA), and two transverse-acoustic (TA). The irreducible representation for the zone-centre optical phonons is $G_{opt} = A_1 + E_1 + 2E_2 + 2B_1$ [39]. The B_1 mode is silent, the A_1 and E_1 modes are both Raman and infrared active, while the E_2 mode is non-polar and Raman-only active. Raman spectra were obtained at an excitation wavelength of 512 nm, as shown in **Figure 4**. The absorption peaks in **Table 2** are attributed to the 1st and 2nd-order Raman active modes of ZnO and Ca-doped ZnO. The two most intense peaks were associated with the nonpolar mode E_2. The E_2^{low} vibrational mode around 100 cm^{-1} corresponds to the vibrations of the zinc sublattice. Another intense vibrational mode E_2^{high} near 438 cm^{-1} corresponds to oxygen migration and is characteristic of the hexagonal wurtzite phase of ZnO [39-42]. The peaks at 334 cm^{-1} and 391 cm^{-1} correspond to the second-order Raman modes (multiple phonon processes) E_2^{high}-E_2^{low} and A_1 (TO) [42], respectively. The peak at 582 cm^{-1} is attributed to the E_1 (LO) vibrational mode. This mode implies the presence of structural defects due to oxygen vacancies, Zn interstitial atoms, and impurities [43]. The combined acoustic and optical vibrational modes A_1 (TA) and A_1 (LO) also occur between 651 cm^{-1} and 665 cm^{-1}.

The E_1 (TO) mode of Zn-O at 410 cm^{-1} [39] is not seen in the current Raman spectrum, but this mode can be seen in the FTIR spectrum. The A_1(LO) mode at 574 cm^{-1} was also missing, as reported by Calleja and Cardona, and this mode could not be detected at excitation wavelengths longer than 406.7 nm [44]. Additional features emerge in the Ca-doped ZnO Raman spectra. The peak at 279 cm^{-1} has been assigned to B_1^{high}-B_1^{low} mode, and the peak at 1090 cm^{-1} can be assigned to the combination of the A_1(LO) and A_1(TO) modes. A broad asymmetric mode at 1157 cm^{-1} depicts the contributions of $2A_1$(LO) and $2E_1$(LO) modes. Additional modes at 279 cm^{-1} were also ascribed to the host lattice defects. Dopant-relat-

ed defects can disrupt the selection rule and activate the silent mode [45].

3.4 Morphological and elemental analysis

Figure 5 shows the FESEM images of the Ca-doped ZnO nanoparticles annealed at 800 °C for 6 hours. Micrographs of all samples show dispersed crystallites and also reveal polycrystalline nature. FESEM shows that all grains are more or less spherical, and the grain boundaries are well separated. The EDAX pattern in **Figure 6** illustrates the presence of prime elements zinc, calcium, and oxygen along with carbon trace as contamination. This carbon trace element was detected through the use of carbon tape as the base on the sample holder. The elemental proportion corresponding to Zn, Ca, and O is in good agreement with permissible error.

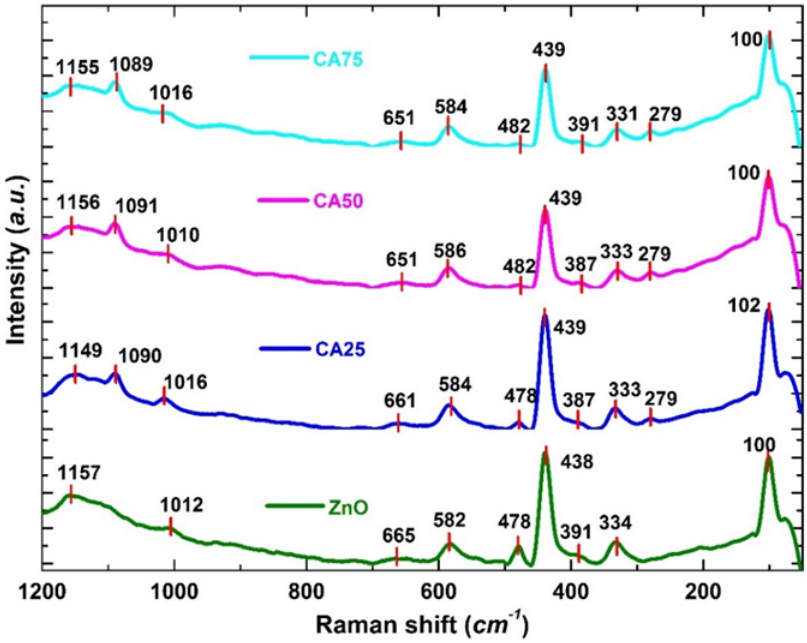

Figure 4. Raman spectra of pure ZnO and Ca-doped ZnO nanoparticles.

Table 2. Raman vibrational modes of ZnO and Ca-doped ZnO.

Sample	Wavenumber (cm^{-1})				PROCESS
ZnO	CA25	CA50	CA75	REFERENCE	
100	102	100	100	99 [39]	E_2^{low}
-	279	279	279	284 [39]	B_1^{high}-B_1^{low}
334	333	333	331	333 [39]	E_2^{high}-E_2^{low}
391	387	387	391	384 [41]	A_1(TO)
438	439	439	439	438 [39]	E_2^{high}
478	478	482	482	483 [39]	2LA
582	584	586	584	586 [41]	E_1(LO)
665	661	651	651	660 [41]	TA + LO
1012	1016	1010	1016	980 [41]	2TO
-	1090	1091	1089	1080 [44]	TO + LO
1157	1149	1156	1155	1158 [39]	$2A_1$(LO), $2E_1$(LO)

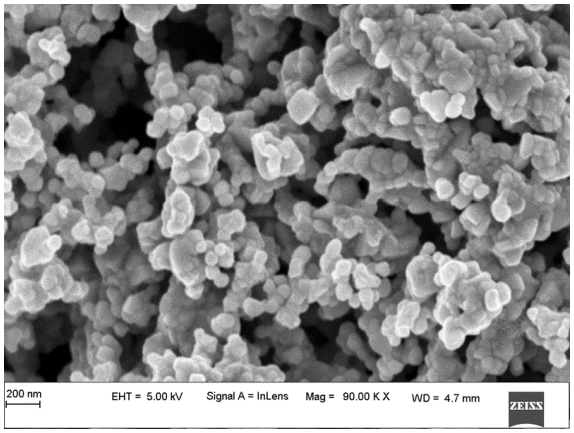

(a)

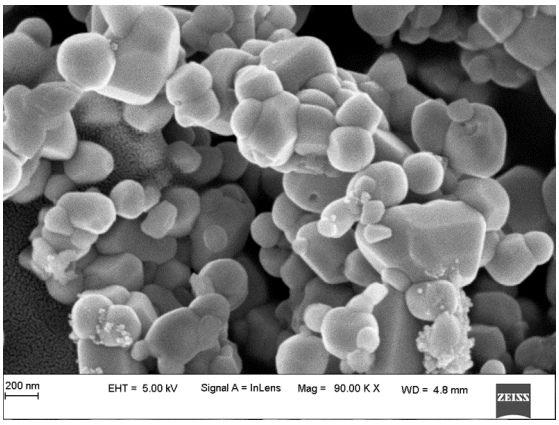

(b)

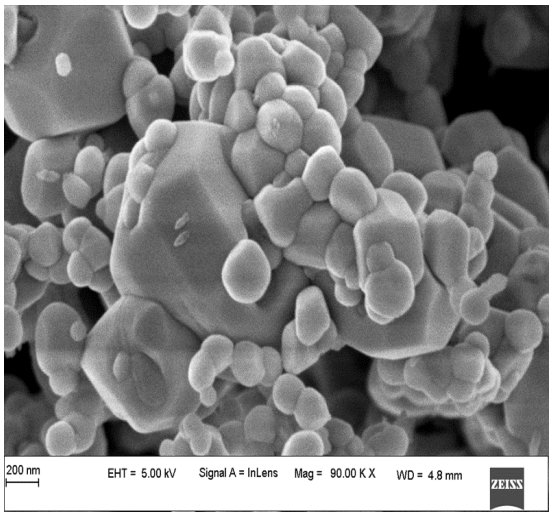

(c)

Figure 5. FESEM images of Ca-doped ZnO nanoparticles (a) $Zn_{0.975}Ca_{0.025}O$ (CA25), (b) $Zn_{0.95}Ca_{0.05}O$ (CA50) and (c) $Zn_{0.925}Ca_{0.075}O$ (CA75).

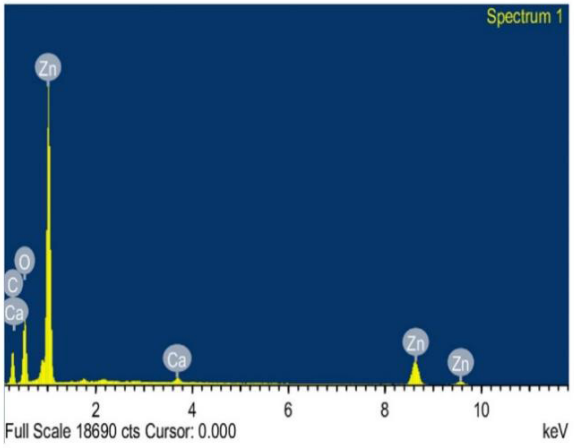

(a)

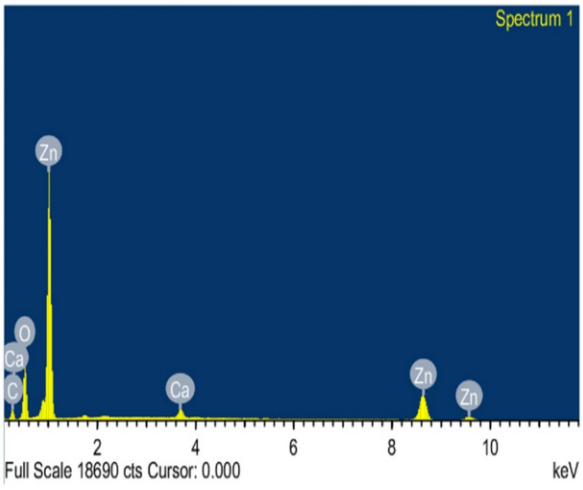

(b)

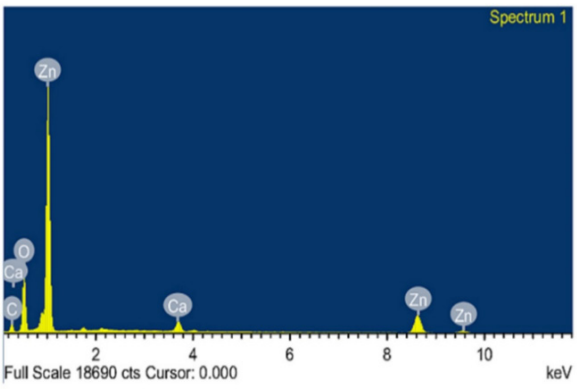

(c)

Figure 6. EDAX spectra of Ca-doped ZnO nanoparticles (a) $Zn_{0.975}Ca_{0.025}O$ (CA25), (b) $Zn_{0.95}Ca_{0.05}O$ (CA50) and (c) $Zn_{0.925}Ca_{0.075}O$ (CA75).

3.5 UV-Vis spectroscopy

Figure 7 shows the UV-Vis spectra of the ZnO and the calcium-doped ZnO samples. The absorption spectrum of pure and Ca-doped ZnO exhibits a strong absorption band at 369 nm due to its wide-bandgap energy. This indicates that the prepared samples were activated only under UV light irradiation. A characteristic absorption peak at about 369 nm can be assigned to the intrinsic bandgap absorption of ZnO due to the electronic transition from the valence band to the conduction band ($O_{2p} \rightarrow Zn_{3d}$) [15]. With increasing Ca concentration at the Zn sites, the samples exhibited a red shift of the absorption band and increased photoactivity. The Bandgap energy of the synthesized samples was determined using Tauc's relation:

$$ahv = A(hv - Eg)^{1/n} \quad (3)$$

where A is the constant of proportionality, h is Planck's constant, α is the absorption coefficient, υ is the optical frequency, and Eg is the energy bandgap. For direct bandgap semiconductors, n = 2. The bandgap energy was determined by plotting $(\alpha h\upsilon)^2$ versus photon energy $h\upsilon$. The undoped ZnO band gap energy is wider than the band gap energy (3.11 eV, FER = 1) in the work written by H. V. Vasei, et al. [46], which may be due to the use of different fuels during preparation. **Table 3** shows the band gap energy of the prepared samples. The band gap energy value from the Tauc plot (**Figure 8**) decreases from 3.24 eV to 3.22 eV with increasing Ca doping concentration. Morphology, size, and synthesis methods of ZnO nanoparticles are believed to influence the bandgap energy [47].

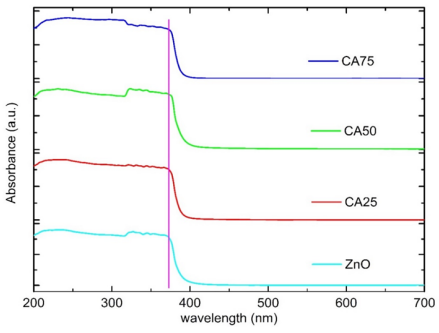

Figure 7. UV-vis absorption spectra of Pure and Ca-doped ZnO nanoparticles.

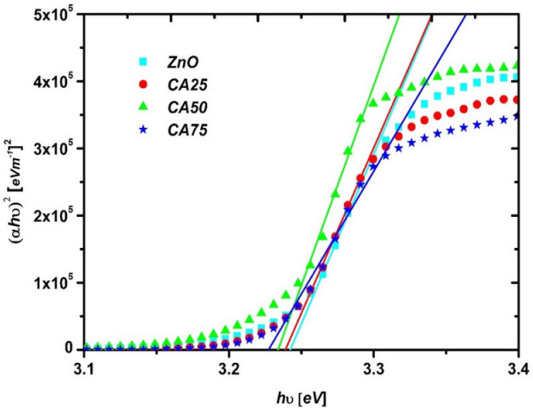

Figure 8. Tauc's plot of pure and Ca-doped ZnO nanoparticles.

Table 3. Bandgap energy of ZnO and Ca-doped ZnO.

Sample	**ZnO**	**CA25**	**CA55**	**CA75**
Band gap energy (*eV*)	3.242	3.238	3.231	3.227

3.6 Photoluminescence (PL) analysis

Figure 9 shows the photoluminescence spectra of pure ZnO and Ca-doped ZnO recorded at an excitation wavelength of 355 nm to determine excited states and defects. **Table 4** shows the emission bands of the prepared samples. The prepared nanoparticles exhibit four emission bands at 395 nm (band edge emission), 430 nm (violet emission), 490 nm (blue emission), and 515 nm, 580 nm (green emission). The UV emission near 395 nm, is attributed to direct exciton recombination resulting from near-band edge transitions in ZnO via an exciton-exciton process [48]. The emission of different visible colours represents the several intrinsic defects Vis Zn vacancies (V_{Zn}), O vacancies (V_0), Zn interstitials (Zn_i), O interstitials (O_i), and O anti-sites (O_{Zn}). The violet emission corresponds to the electron transitions from the shallow donor level of neutral Zni to the top of the valence band [49-51]. The blue emission is due to electron transfer from shallow donor levels of Zn interstitial atoms (Zn_i) to an acceptor level of neutral Zn vacancies (V_{Zn}) [52,53]. Green emission represents the radial recombination of photogenerated holes with electrons from the single-ionized oxygen (O) vacancies in the ZnO lattice surface. Furthermore, this is also due to radiative transitions between shallow donors (associated with O vacancies) and deep acceptors (Zn

vacancies) [54,55].

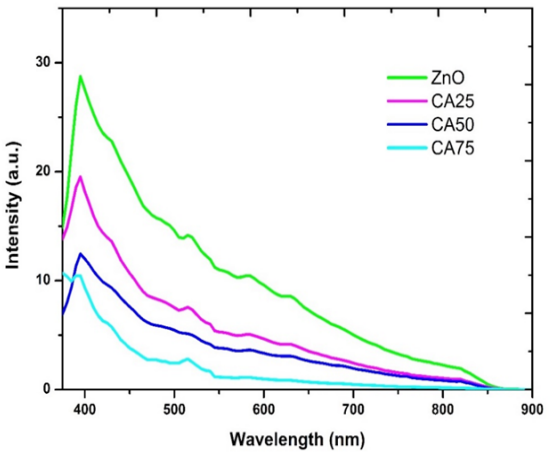

Figure 9. Photoluminescence emission spectra of pure and Ca-doped nanoparticles.

Table 4. Photoluminescence emission bands of ZnO and Ca-doped ZnO.

Sample Name	**Emission (nm)**				
ZnO	395	430	490	515	580
$Zn_{0.975}Ca_{0.025}O$	395	430	490	515	580
$Zn_{0.95}Ca_{0.05}O$	395	430	495	515	585
$Zn_{0.925}Ca_{0.075}O$	390	430	485	515	580
	UV	Violet	Blue	Green	Green

3.7 Impedance analysis

Impedance spectroscopy consists measurement of impedance Z as a function of frequency (υ). Sintered pellets coated with silver paint on both sides were used for impedance measurements. The impedance analyzer record the magnitude of the impedance |Z| and phase angle θ at various frequencies. Real (Z′) and imaginary (Z″) parts of the complex impedance ($Z^* = Z' + j\,Z''$) were calculated using $Z' = |Z| \cos\theta$ and $Z'' = |Z| \sin\theta$.

Figure 10 shows impedance spectra or Cole-Cole plots consisting of the real parts (Z′) and imaginary (Z″) parts of the complex impedance of the prepared samples. The Cole-Cole plots provide information on the resistance offered by the grain interior (G), grain boundary (GB), and electrode-material interfaces to the conduction of the charge carriers. The impedance spectrum consists of two semicircles, one at a high-frequency region and another at mid or low frequencies. The high-frequency semicircle ascribed to grain (G), and the semicircle at low frequency represents the grain boundary (GB) contribution. Grain resistance (R_g) and resistance due to grain boundary (R_{gb}) were obtained by fitting *R-CPE* equivalent circuits using Zview2. The general expression for the impedance of a constant phase element (*CPE)* is $Z_{CPE} = 1/Q(j\omega)^n$, where Q is the constant phase element (CPE), $j = \sqrt{-1}$ and ω is the angular frequency(ω = 2πυ, υ-frequency). When n = 1, Q acts as ideal capacitance C. The solid line represents the fit to the experimental data based on the equivalent circuit ($R_g||Q_g$) ($R_{gb}||Q_{gb}$) by Zview2. The total resistance (R_t) to the ion conduction is $R_t = R_g + R_{gb}$. The total conductivity of the samples was calculated using $\sigma_t = t/R_tA$. Where t is the pellet thickness, A is the pellet area, and R_t is the total resistance. **Table 5** consists of the fitted resistance values, the calculated grain conductivity ($\sigma_g = t/R_gA$), grain boundary conductivity ($\sigma_{gb} = t/R_{gb}A$), and total conductivity. Capacitors or CPEs in the *pF* range reflect grain interiors, and the *nF* range reflects grain boundaries. The grain resistance decreases with increasing the Ca doping concentration, similar to the results obtained by Irshad Ahmad et al. [48], whereas the grain boundary resistance increases with increasing Ca doping. **Figure 11** shows the variation of conductivity with dopant (Ca) concentration. It observed that there is an increase in grain conductivity with increasing doping because there is an increase of the charge carriers with increasing calcium doping [56]. On the other hand, the grain boundary conductivity decrease with increasing Ca doping. This is due to the precipitation of calcium at the ZnO grain boundaries, which calcifies the grain boundaries [57] and reduces the overall conductivity.

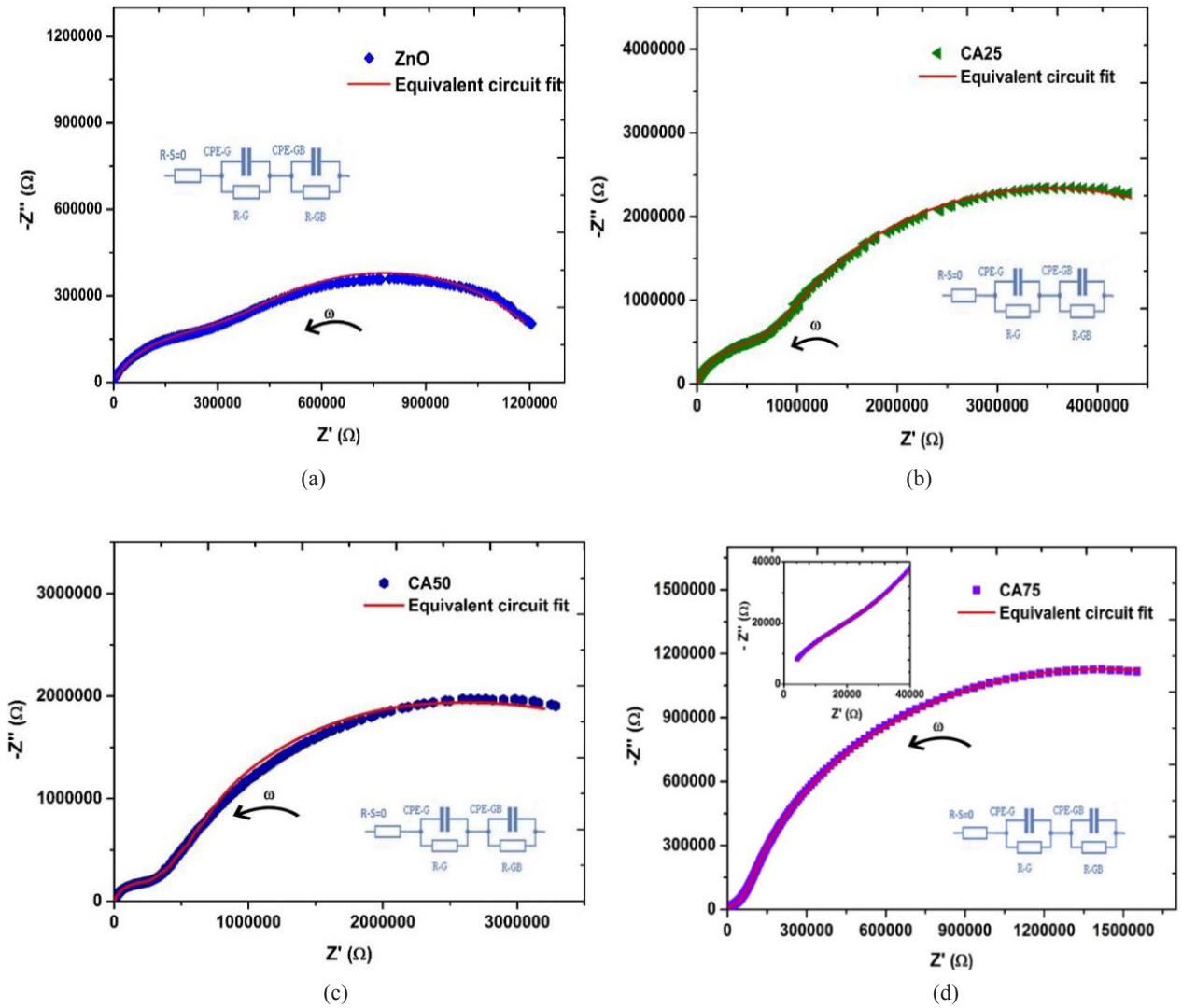

Figure 10. Impedance spectra or Cole-Cole plot of pure and Ca doped ZnO pellets sintered at 700 °C (a) ZnO (CA00), (b) $Zn_{0.975}Ca_{0.025}O$ (CA25), (c) $Zn_{0.95}Ca_{0.05}O$ (CA50) and (d) $Zn_{0.925}Ca_{0.075}O$ (CA75).

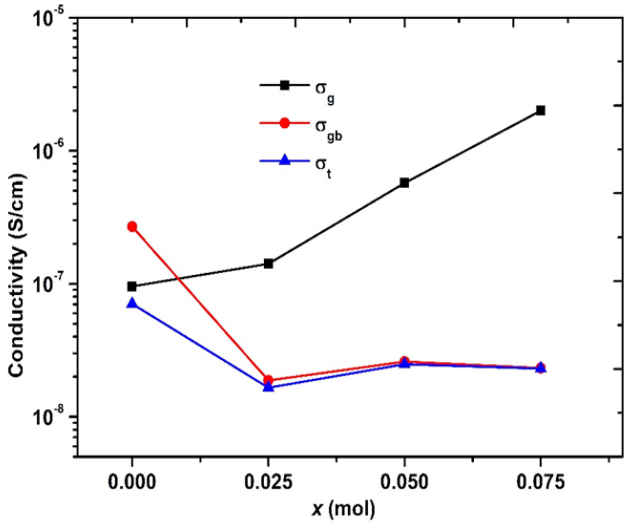

Figure 11. Variation of conductivity with dopant concentration.

Table 5. Impedance analysis results: Grain resistance (R_g), grain boundary resistance (R_{gb}), total resistance (R_t) and the calculated grain conductivity (σ_g), grain boundary conductivity (σ_{gb}) and total conductivity (σ_t).

Sample	R_g (ohm)	R_{gb} (ohm)	R_t (ohm)	σ_g (S/cm)	σ_{gb} (S/cm)	σ_t (S/cm)
ZnO	961430	341830	1303260	9.56×10^{-8}	2.69×10^{-7}	7.05×10^{-8}
CA25	746390	5629800	6376190	1.41×10^{-7}	1.87×10^{-8}	1.65×10^{-8}
CA50	194240	4278300	4472540	5.71×10^{-7}	2.59×10^{-8}	2.48×10^{-8}
CA75	31659	2722400	2754060	2.00×10^{-6}	2.33×10^{-8}	2.30×10^{-8}

4. Conclusions

The pure and Ca-doped ZnO nanoparticles were successfully prepared by the solution combustion technique. XRD investigations confirmed that the prepared samples had a hexagonal wurtzite structure without heterogeneous phases. XRD analysis also shows structural changes with Ca concentration, both in terms of lattice parameter and crystallite size. FESEM images show that the particles are nearly spherical and have few aggregates. EDX analysis identified the chemical composition of the prepared samples. The Raman spectrum depicts the hexagonal wurtzite structure of the ZnO, indicating the first and second-order active modes of the ZnO. The presence of wurtzite structural defects in the prepared samples was identified using PL spectroscopy. The decrease in optical bandgap is due to the increase in carrier concentration in Ca-doped ZnO nanoparticles, which increases the grain conductivity of the Ca-doped samples. The red shift of the energy bandgap and increase in grain conductivity suggests that Ca-doped ZnO is a potential candidate for photocatalytic applications.

Author Contributions

K. N. Ganesha: Conceptualization, data collection, analysis, investigation, methodology, writing—original draft; H. Chandrappa: Resources and feedback; S. R. Kumarswamy: Resources and critical feedback; V. Annadurai: Resources and critical feedback; H. Somashekarappa: Conceptualization, Supervision, validation, visualization, writing—review and editing; R. Somashekar: Conceptualization, validation, visualization, writing—review and editing.

Conflict of Interest

There is no conflict of interest.

Acknowledgement

The authors thank the Department of Collegiate Education, Government of Karnataka providing a grant to purchase equipment for sample preparation. The authors acknowledge the DST-PURSE laboratory at Mangalagangotri, Mangalore University, facilitating the XRD, FESEM, and EDX characterization facility. The authors thank SAIF, IITM, Chennai, for FTIR and UV-VIS characterization facilities. Authors acknowledge IOE, University of Mysore, Manasagangotri, Mysore 570 006, India facilitating Raman and Impedance analyzer.

References

[1] Chao, J., Chen, Y., Xing, S., et al., 2019. Facile fabrication of ZnO/C nanoporous fibers and ZnO hollow spheres for high performance gas sensor. Sensors and Actuators B: Chemical. 298, 126927.
DOI: https://doi.org/10.1016/j.snb.2019.126927

[2] Franco, M.A., Conti, P.P., Andre, R.S., et al., 2022. A review on chemiresistive ZnO gas sensors. Sensors and Actuators Reports. 4, 100100.
DOI: https://doi.org/10.1016/j.snr.2022.100100

[3] Kulkarni, D.R., Malode, S.J., Prabhu, K.K., et al.,

2020. Development of a novel nanosensor using Ca-doped ZnO for antihistamine drug. Materials Chemistry and Physics. 246, 122791.
DOI: https://doi.org/10.1016/j.matchemphys.2020.122791

[4] Alshammari, A.S., Khan, Z.R., Gandouzi, M., et al., 2022. Tailoring the optical properties and the UV detection performance of sol-gel deposited ZnO nanostructured thin films via Cd and Na co-doping. Optical Materials. 126, 112146.
DOI: https://doi.org/10.1016/j.optmat.2022.112146

[5] Li, L.E., Demianets, L.N.. 2008. Room-temperature excitonic lasing in ZnO tetrapod-like crystallites. Optical Materials. 30(7), 1074-1078.
DOI: https://doi.org/10.1016/j.optmat.2007.05.013

[6] Pandey, R.K., Dutta, J., Brahma, S., et al., 2021. Review on ZnO-based piezotronics and piezoelectric nanogenerators: Aspects of piezopotential and screening effect. Journal of Physics: Materials. 4(4), 044011.
DOI: https://dx.doi.org/10.1088/2515-7639/ac130a

[7] Sahoo, R., Mishra, S., Ramadoss, A., et al., 2020. An approach towards the fabrication of energy harvesting device using Ca-doped ZnO/PVDF-TrFE composite film. Polymer. 205, 122869.
DOI: https://doi.org/10.1016/j.polymer.2020.122869

[8] Liu, J., Wang, Y., Ma, J., et al., 2019. A review on bidirectional analogies between the photocatalysis and antibacterial properties of ZnO. Journal of Alloys and Compounds. 783, 898-918.
DOI: https://doi.org/10.1016/j.jallcom.2018.12.330

[9] Kim, I., Viswanathan, K., Kasi, G., et al., 2022. ZnO nanostructures in active antibacterial food packaging: Preparation methods, antimicrobial mechanisms, safety issues, future prospects, and challenges. Food Reviews International. 38(4), 537-565.
DOI: https://doi.org/10.1080/87559129.2020.1737709

[10] Kumar, R., Umar, A., Kumar, G., et al., 2017. Antimicrobial properties of ZnO nanomaterials: A review. Ceramics International. 43(5), 3940-3961.
DOI: https://doi.org/10.1016/j.ceramint.2016.12.062

[11] Hameed, A., Fatima, G.R., Malik, K., et al., 2019. Scope of nanotechnology in cosmetics: Dermatology and skin care products. Journal of Medicinal Chemical Science. 2(1), 9-16.
DOI: https://doi.org/10.26655/jmchemsci.2019.6.2

[12] Safdar, M., Waqas, M., Jabeen, N., et al., 2022. Fabrication of In_2Te_3 nanowalls garnished with ZnO nanoparticles and their field emission behavior. Materials Chemistry and Physics. 290, 126510.
DOI: https://doi.org/10.1016/j.matchemphys.2022.126510

[13] Özgür, Ü., Alivov, Y.I., Liu, C., et al., 2005. A comprehensive review of ZnO materials and devices. Journal of Applied Physics. 98(4), 11.
DOI: https://doi.org/10.1063/1.1992666

[14] Selvi, K.T., Mangai, K.A., Priya, M., et al., 2020. Investigation of the dielectric and impedance properties of ZnO/MgO nanocomposite. Physica B: Condensed Matter. 594, 412355.
DOI: https://doi.org/10.1016/j.physb.2020.412355

[15] Sulciute, A., Nishimura, K., Gilshtein, E., et al., 2021. ZnO nanostructures application in electrochemistry: Influence of morphology. The Journal of Physical Chemistry C. 125(2), 1472-1482.
DOI: https://doi.org/10.1021/acs.jpcc.0c08459

[16] Umavathi, S., AlSalhi, M.S., Devanesan, S., et al., 2020. Synthesis and characterization of ZnO and Ca-ZnO nanoparticles for potential antibacterial activity and plant micronutrients. Surfaces and Interfaces. 21, 100796.
DOI: https://doi.org/10.1016/j.surfin.2020.100796

[17] Mahajan, P., Singh, A., Arya, S., 2020. Improved performance of solution processed organic solar cells with an additive layer of sol-gel synthesized ZnO/CuO core/shell nanoparticles. Journal of Alloys and Compounds. 814, 152292.
DOI: https://doi.org/10.1016/j.jallcom.2019.152292

[18] Abed, C., Bouzidi, C., Elhouichet, H., et al., 2015. Mg doping induced high structural quality of sol-gel ZnO nanocrystals: Application in photocatalysis. Applied Surface Science. 349, 855-

863.
DOI: https://doi.org/10.1016/j.apsusc.2015.05.078

[19] Liu, S., Zhu, L., Cao, W., et al., 2021. Defect-related optical properties of Mg-doped ZnO nanoparticles synthesized via low temperature hydrothermal method. Journal of Alloys and Compounds. 858, 157654.
DOI: https://doi.org/10.1016/j.jallcom.2020.157654

[20] Suwanboon, S., Amornpitoksuk, P., Sukolrat, A., 2011. Dependence of optical properties on doping metal, crystallite size and defect concentration of M-doped ZnO nanopowders (M = Al, Mg, Ti). Ceramics International. 37(4), 1359-1365.
DOI: https://doi.org/10.1016/j.ceramint.2010.12.010

[21] Ahmad, F., Maqsood, A., 2021. Structural, electric modulus and complex impedance analysis of ZnO at low temperatures. Materials Science and Engineering: B. 273, 115431.
DOI: https://doi.org/10.1016/j.mseb.2021.115431

[22] Kuo, C.L., Wang, C.L., Ko, H.H., et al., 2010. Synthesis of zinc oxide nanocrystalline powders for cosmetic applications. Ceramics International. 36(2), 693-698.
DOI: https://doi.org/10.1016/j.ceramint.2009.10.011

[23] Hameed, A.S.H., Karthikeyan, C., Sasikumar, S., et al., 2013. Impact of alkaline metal ions Mg^{2+}, Ca^{2+}, $Sr2^{+}$ and Ba^{2+} on the structural, optical, thermal and antibacterial properties of ZnO nanoparticles prepared by the co-precipitation method. Journal of Materials Chemistry B. 1(43), 5950-5962.
DOI: http://dx.doi.org/10.1039/c3tb21068e

[24] Pathak, T.K., Kumar, A., Swart, C.W., et al., 2016. Effect of fuel content on luminescence and antibacterial properties of zinc oxide nanocrystalline powders synthesized by the combustion method. RSC Advances. 6(100), 97770-97782.
DOI: http://dx.doi.org/10.1039/C6RA22341A

[25] El Mir, L., 2017. Luminescence properties of calcium doped zinc oxide nanoparticles. Journal of Luminescence. 186, 98-102.
DOI: https://doi.org/10.1016/j.jlumin.2017.02.029

[26] Karthikeyan, B., Pandiyarajan, T., Mangaiyarkarasi, K., 2011. Optical properties of sol-gel synthesized calcium doped ZnO nanostructures. Spectrochimica Acta Part A: Molecular and Biomolecular Spectroscopy. 82(1), 97-101.
DOI: https://doi.org/10.1016/j.saa.2011.07.005

[27] Morales, A.E., Zaldivar, M.H., Pal, U., 2006. Indium doping in nanostructured ZnO through low-temperature hydrothermal process. Optical Materials. 29(1), 100-104.
DOI: https://doi.org/10.1016/j.optmat.2006.03.010

[28] Ilager, D., Malode, S.J., Kulkarni, R.M., et al., 2022. Electrochemical sensor based on Ca-doped ZnO nanostructured carbon matrix for algicide dichlone. Journal of Hazardous Materials Advances. 7, 100132.
DOI: https://doi.org/10.1016/j.hazadv.2022.100132

[29] Ilager, D., Shetti, N.P., Malladi, R.S., et al., 2021. Synthesis of Ca-doped ZnO nanoparticles and its application as highly efficient electrochemical sensor for the determination of anti-viral drug, acyclovir. Journal of Molecular Liquids. 322, 114552.
DOI: https://doi.org/10.1016/j.molliq.2020.114552

[30] Jaballah, S., Benamara, M., Dahman, H., et al., 2020. Formaldehyde sensing characteristics of calcium-doped zinc oxide nanoparticles-based gas sensor. Journal of Materials Science: Materials in Electronics. 31, 8230-8239.
DOI: https://doi.org/10.1007/s10854-020-03358-y

[31] Varma, A., Mukasyan, A.S., Rogachev, A.S., et al., 2016. Solution combustion synthesis of nanoscale materials. Chemical Reviews. 116(23), 14493-14586.
DOI: https://doi.org/10.1021/acs.chemrev.6b00279

[32] Cheruku, R., Vijayan, L., Govindaraj, G., 2012. Electrical relaxation studies of solution combustion synthesized nanocrystalline Li_2NiZrO_4 material. Materials Science and Engineering: B. 177(11), 771-779.
DOI: https://doi.org/10.1016/j.mseb.2012.04.005

[33] Jain, S.R., Adiga, K.C., Verneker, V.P., 1981. A new approach to thermochemical calculations of condensed fuel-oxidizer mixtures. Combustion

and Flame. 40, 71-79.
DOI: https://doi.org/10.1016/0010-2180(81)90111-5

[34] Pathak, L.C., Singh, T.B., Das, S., et al., 2002. Effect of pH on the combustion synthesis of nano-crystalline alumina powder. Materials Letters. 57(2), 380-385.
DOI: https://doi.org/10.1016/S0167-577X(02)00796-6

[35] Scherrer, P., 1918. Bestimmung der Grösse und der inneren Struktur von Kolloidteilchen mittels Röntgenstrahlen (German) [Determination of the size and internal structure of colloidal particles using X-rays]. Nachr. Ges. Wiss. Göttingen. 26, 98-100.

[36] Cheng, B., Xiao, Y., Wu, G., et al., 2004. The vibrational properties of one-dimensional ZnO: Ce nanostructures. Applied Physics Letters. 84(3), 416-418.
DOI: https://doi.org/10.1063/1.1639131

[37] Vergés, M.A., Mifsud, A., Serna, C.J., 1990. Formation of rod-like zinc oxide microcrystals in homogeneous solutions. Journal of the Chemical Society, Faraday Transactions. 86(6), 959-963.
DOI: http://dx.doi.org/10.1039/FT9908600959

[38] Sigoli, F.A., Davolos, M.R., Jafelicci Jr, M., 1997. Morphological evolution of zinc oxide originating from zinc hydroxide carbonate. Journal of Alloys and Compounds. 262, 292-295.
DOI: https://doi.org/10.1016/S0925-8388(97)00404-0

[39] Cuscó, R., Alarcón-Lladó, E., Ibanez, J., et al., 2007. Temperature dependence of Raman scattering in ZnO. Physical Review B. 75(16), 165202.
DOI: https://doi.org/10.1103/PhysRevB.75.165202

[40] Damen, T.C., Porto, S.P.S., Tell, B., 1966. Raman effect in zinc oxide. Physical Review. 142(2), 570.
DOI: https://doi.org/10.1103/PhysRev.142.570

[41] Šćepanović, M.G.B.M., Grujić-Brojčin, M., Vojisavljević, K., et al., 2010. Raman study of structural disorder in ZnO nanopowders. Journal of Raman Spectroscopy. 41(9), 914-921.
DOI: https://doi.org/10.1002/jrs.2546

[42] Rosset, A., Djessas, K., Goetz, V., et al., 2020. Sol-gel synthesis and solar photocatalytic activity of Ca-alloyed ZnO nanoparticles elaborated using different precursors. RSC Advances. 10(43), 25456-25466.
DOI: http://dx.doi.org/10.1039/C9RA10131D

[43] Xing, Y.J., Xi, Z.H., Xue, Z.Q., et al., 2003. Optical properties of the ZnO nanotubes synthesized via vapor phase growth. Applied Physics Letters. 83(9), 1689-1691.
DOI: https://doi.org/10.1063/1.1605808

[44] Calleja, J.M., Cardona, M., 1977. Resonant raman scattering in ZnO. Physical Review B. 16(8), 3753.
DOI: https://link.aps.org/doi/10.1103/PhysRevB.16.3753

[45] Bundesmann, C., Ashkenov, N., Schubert, M., et al., 2003. Raman scattering in ZnO thin films doped with Fe, Sb, Al, Ga, and Li. Applied Physics Letters. 83(10), 1974-1976.
DOI: https://doi.org/10.1063/1.1609251

[46] Vasei, H.V., Masoudpanah, S.M., Habibollahzadeh, M., 2020. Different morphologies of ZnO via solution combustion synthesis: The role of fuel. Materials Research Bulletin. 125, 110784.
DOI: https://doi.org/10.1016/j.materresbull.2020.110784

[47] Agarwal, S., Jangir, L.K., Rathore, K.S., et al., 2019. Morphology-dependent structural and optical properties of ZnO nanostructures. Applied Physics A. 125, 1-7.
DOI: https://doi.org/10.1007/s00339-019-2852-x

[48] Ahmad, I., Ahmed, E., Ahmad, M., et al., 2020. The investigation of hydrogen evolution using Ca doped ZnO catalysts under visible light illumination. Materials Science in Semiconductor Processing. 105, 104748.
DOI: https://doi.org/10.1016/j.mssp.2019.104748

[49] Pascariu, P., Tudose, I.V., Suchea, M., et al., 2018. Preparation and characterization of Ni, Co doped ZnO nanoparticles for photocatalytic applications. Applied Surface Science. 448, 481-488.
DOI: https://doi.org/10.1016/j.apsusc.2018.04.124

[50] Kumar, A.S., Huang, N.M., Nagaraja, H.S.,

2014. Influence of Sn doping on photoluminescence and photoelectrochemical properties of ZnO nanorod arrays. Electronic Materials Letters. 10, 753-758.
DOI: https://doi.org/10.1007/s13391-014-3348-7

[51] Mishra, S.K., Srivastava, R.K., Prakash, S.G., et al., 2010. Photoluminescence and photoconductive characteristics of hydrothermally synthesized ZnO nanoparticles. Opto-Electronics Review. 18(4), 467-473.
DOI: https://doi.org/10.2478/s11772-010-0037-4

[52] Wu, C., Shen, L., Zhang, Y.C., et al., 2011. Solvothermal synthesis of Cr-doped ZnO nanowires with visible light-driven photocatalytic activity. Materials Letters. 65(12), 1794-1796.
DOI: https://doi.org/10.1016/j.matlet.2011.03.070

[53] Umar, A., Ribeiro, C., Al-Hajry, A., et al., 2009. Growth of highly c-axis-oriented ZnO nanorods on ZnO/glass substrate: Growth mechanism, structural, and optical properties. The Journal of Physical Chemistry C. 113(33), 14715-14720.
DOI: https://doi.org/10.1021/jp9045098

[54] Umar, A., Hahn, Y.B., 2006. ZnO nanosheet networks and hexagonal nanodiscs grown on silicon substrate: Growth mechanism and structural and optical properties. Nanotechnology. 17(9), 2174.
DOI: https://dx.doi.org/10.1088/0957-4484/17/9/016

[55] Dai, Y., Zhang, Y., Bai, Y.Q., et al., 2003. Bicrystalline zinc oxide nanowires. Chemical Physics Letters. 375(1-2), 96-101.
DOI: https://doi.org/10.1016/S0009-2614(03)00823-6

[56] Saadi, H., Rhouma, F.I.H., Benzarti, Z., et al., 2020. Electrical conductivity improvement of Fe doped ZnO nanopowders. Materials Research Bulletin. 129, 110884.
DOI: https://doi.org/10.1016/j.materresbull.2020.110884

[57] Zhao, H., Wang, H., Meng, X., et al., 2021. A method to reduce ZnO grain resistance and improve the intergranular layer resistance by Ca^{2+} and Al^{3+} co-doping. Materials Science in Semiconductor Processing. 128, 105768.
DOI: https://doi.org/10.1016/j.mssp.2021.105768

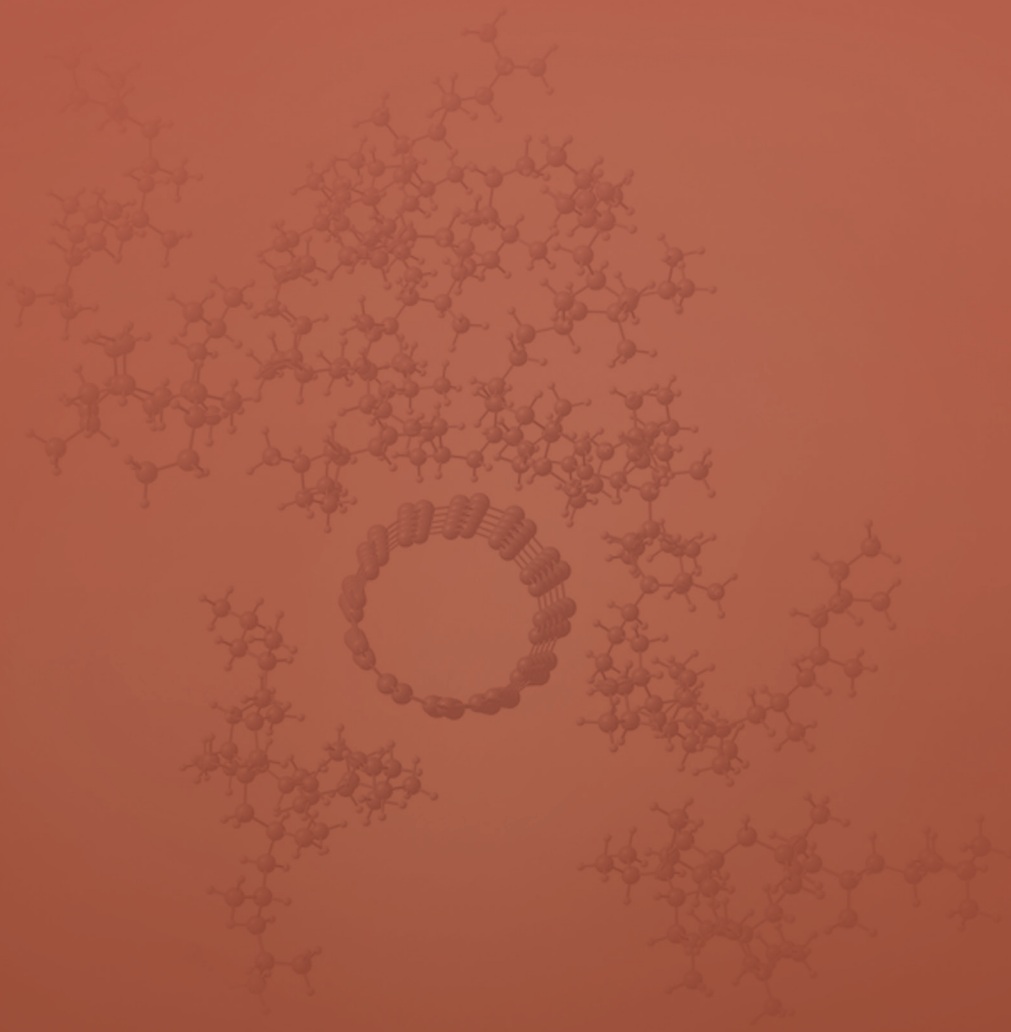

BILINGUAL PUBLISHING GROUP

Tel:+65 65881289
E-mail: contact@bilpublishing.com
Website:https://journals.bilpubgroup.com

2661-3301
01
9 772661 330239